

UNIVERSIDAD AUTÓNOMA DE BAJA CALIFORNIA
FACULTAD DE CIENCIAS MARINAS
INSTITUTO DE INVESTIGACIONES OCEANOLÓGICAS



**ANÁLISIS DE LA EVOLUCIÓN DEL ESPECTRO DIRECCIONAL DEL OLEAJE
LIBRE EN EL GOLFO DE TEHUANTEPEC BAJO CONDICIONES DE VIENTO
INTENSO UTILIZANDO IMÁGENES DE RADAR DE APERTURA SINTÉTICA.**

T E S I S

**QUE PARA CUBRIR PARCIALMENTE LOS REQUISITOS NECESARIOS PARA
OBTENER EL GRADO DE**

DOCTOR EN CIENCIAS EN OCEANOGRAFIA COSTERA

PRESENTA

GUILLERMO MAURICIO DÍAZ MÉNDEZ

ENSENADA, BAJA CALIFORNIA, MEXICO. AGOSTO DE 2011.

RESUMEN

El presente trabajo de tesis doctoral ha tenido por objeto contribuir al estado del conocimiento sobre la evolución del oleaje en el Golfo de Tehuantepec y océano Pacífico adyacente, bajo las condiciones de viento intenso características de este área de estudio. Para ello se han utilizado, como fuente principal de información, imágenes de la superficie del océano adquiridas desde satélites mediante radar de apertura sintética (SAR, del inglés *synthetic aperture radar*). Las características de los campos de oleaje y viento estimados mediante SAR han sido comparadas con parámetros correspondientes, calculados a partir de mediciones de campo y resultados de simulación numérica.

Con base en los análisis realizados se puede concluir que, de manera general, el campo de oleaje en el Golfo de Tehuantepec se caracteriza por presentar estados de mar dominados por múltiples sistemas de oleaje libre coexistiendo simultáneamente, con valores típicos (asociados a los picos del espectro) de longitud de onda $L_p = 200\text{--}400$ m, altura significante $H_s = 0.5\text{--}4$ m y dirección de propagación en el sector azimutal $\alpha_p = 335^\circ\text{--}135^\circ$. Estos sistemas se propagan a lo largo de hasta 14,000 km, principalmente desde el Pacífico sudoccidental frente a la costa Antártica, así como también desde el Pacífico norte; aunque estos últimos, raramente se detectan en el interior del

Golfo al norte de los 15.25° de latitud. Además del oleaje generado por tormentas lejanas, en la zona de estudio se observa la presencia de oleaje local, generado por los *Tehuanos*. Dado que la frecuencia e intensidad de los vientos de chorro son mayores durante los meses de invierno y primavera, en estas épocas el oleaje forzado puede alcanzar valores de $Hs_{sea} \sim 3$ m y $L_{p_sea} \sim 120$ m en las inmediaciones del Golfo.

A partir de los análisis realizados en este trabajo se puede concluir que el SAR es una herramienta adecuada para estimar la variabilidad espacial de los campos de viento y oleaje, además de otros procesos que imprimen su huella sobre la superficie del mar, aunque con ciertas limitaciones. Tiene la ventaja de que proporciona información detallada sobre las características espaciales del oleaje en áreas del océano de decenas a centenas de kilómetros en forma casi instantánea. Sin embargo, su capacidad de detección está circunscrita al rango de longitudes de onda correspondientes al oleaje libre y limitada por factores como el viento y el estado de mar. Además, dado que el ciclo orbital de los satélites (intervalo de tiempo en el que se repite la misma órbita exactamente) es de varios días, la resolución temporal adecuada para estudiar la naturaleza del oleaje en el área de estudio es también limitada. Así, aunque algunos trabajos han demostrado que el viento es capaz de provocar la atenuación del oleaje propagándose en sentido contrario o que las corrientes pueden provocar una fuerte refracción de las olas, los resultados de mis análisis con SAR no son concluyentes en este sentido. Considero que sería muy interesante realizar

experimentos adicionales, en el que pudiera disponerse de un acervo más completo de imágenes SAR, quizás adquiridas durante distintas fases de evolución de un *Tehuano* y quizás en combinación con otros sensores.

Palabras clave: *Radar de Apertura Sintética, Oleaje libre, Golfo de Tehuantepec*

FACULTAD DE CIENCIAS MARINAS
INSTITUTO DE INVESTIGACIONES OCEANOLÓGICAS
POSGRADO EN OCEANGRAFÍA COSTERA

ANÁLISIS DE LA EVOLUCIÓN DEL ESPECTRO DIRECCIONAL
DEL OLEAJE LIBRE EN EL GOLFO DE TEHUANTEPEC BAJO
CONDICIONES DE VIENTO INTENSO UTILIZANDO IMÁGENES
DE RADAR DE APERTURA SINTÉTICA.

T E S I S

QUE PARA CUBRIR PARCIALMENTE LOS REQUISITOS NECESARIOS PARA
OBTENER EL GRADO DE

DOCTOR EN CIENCIAS

PRESENTA

GUILLERMO MAURICIO DÍAZ MÉNDEZ

Aprobada por:

Dr. Francisco Javier Ocampo Torres
Director

Dr. Reginaldo Durazo Arvizu
Sinodal

Dr. José Pedro Osuna Cañedo
Sinodal

Dr. Rafael Hernández Walls
Sinodal

Dr. Oscar Efraín González Yajimovich
Sinodal

DEDICATORIA

A mi padre... ejemplo, guía e inspiración: siempre fue y siempre será.

A María... mi mejor amiga, mi compañera: sin ella, este trabajo no existiría.

A Lucía... lindo angelito: nuestra hermosa proyección al futuro.

"Muertos los piojos por hacer columpio..." ¿cierto, Ma'?

AGRADECIMIENTOS

Quiero agradecer a cada uno de los integrantes de mi Comité de Tesis por su apoyo, sus comentarios y sus sugerencias para la realización de este trabajo, así como por su amistad a lo largo de estos cinco años de estudio. Agradezco a la Dra. Susanne Lehner de IMF-DLR y al Dr. Bertrand Chapron de LOS-IFREMER por su apoyo y su hospitalidad durante las estancias de investigación realizadas en sus respectivos centros de trabajo. Agradezco de forma especial a Mónica Sánchez del departamento de Oceanografía Física del CICESE y a Angélica Arce de la Facultad de Ciencias Marinas, UABC, sin cuya asistencia no hubiese podido sortear los "vericuetos" administrativos varios, inherentes a la realización de un posgrado; agradezco también a Marie Laure Quentel y a Theresia Hantel, por su amable asistencia administrativa en IFREMER y DLR, respectivamente.

Este trabajo de tesis ha sido posible gracias al apoyo del Consejo Nacional de Ciencia y Tecnología (CONACyT), a través de sus programas de Doctorado de Excelencia y de Becas Mixtas para estancias en el extranjero, así como de los proyectos COGOTE (U40822-F), INGOTEPA (85108), DIROC-IOA (CB-2006/62520) y PE-oleajePBC (S0019-2009-01/119798). Agradezco también el apoyo de la UABC a través de su programa de Intercambio Estudiantil, así como de los proyectos internos 323 y 341 (Programa para el estudio del Golfo de Tehuantepec y Dinámica costera en el Golfo de Tehuantepec - los *Nortes*

revisitados, respectivamente) de la Facultad de Ciencias Marinas. Debo agradecer asimismo el apoyo de los varios organismos y centros de investigación cuyas bases datos han proporcionado información invaluable para la realización de este trabajo: el Centro de Investigación Científica y Educación Superior de Ensenada (CICESE), la Agencia Espacial Europea (ESA), el Centro Europeo para la Predicción del Clima a Medio Plazo (ECMWF), el Centro Aeroespacial Alemán (DLR), el Servicio Meteorológico Alemán (DWD), el Laboratorio de Oceanografía Espacial de IFREMER (CERSAT), el Centro Nacional de Datos de Boyas (NDBC) de la NOAA en EE. UU., etc.

Agradezco a mis compañeros del laboratorio, a mis compañeros de la Facultad y del CICESE, así como a mis queridos amigos, quienes hacen de Ensenada uno de los lugares más agradables del mundo para vivir: Lorena y Reginaldo, Gaby y Toño, Pedro, Paco, Leticia y Ernesto, Martha y Gustavo, Malena, Montse, Cynthia y Efraín, Claudia, Ana y Beto, Cecilia, Claudia, Gaby Marcia, Noel, Lupillo, Ricardo, Willy, Álvaro y todos aquellos a quienes mi mala memoria traiciona en este momento.

Finalmente, gracias Ju, gracias Eu y gracias Car: sin nuestras cyberchorchas dominicales, Lomas Verdes, Ensenada, Brest, Munich, Santander, Chilliwack y Palm Springs estarían más lejos entre sí de lo que han estado.

i. ÍNDICE

	Página
i. Índice	I
ii. Lista de tablas	III
iii. Lista de figuras	V
I. Introducción	1
I.1. Antecedentes	5
I.2. Motivación	9
I.3. Objetivos	10
II. Análisis de viento y oleaje en la costa del Pacífico sur de México utilizando imágenes del satélite TerraSAR-X - <i>artículo publicado.</i>	12
III. Análisis de la variabilidad del oleaje libre bajo condiciones de viento moderado en el Golfo de Tehuantepec utilizando radar de apertura	37

sintética - *artículo en revisión.*

IV. Estimación del espectro de oleaje a partir de imágenes de la superficie del mar adquiridas con TerraSAR-X - *artículo en preparación.* 82

V. Conclusiones generales 108

VI. Literatura citada 113

ii. LISTA DE TABLAS

II - Tabla 1. Parámetros característicos de los tipos de imágenes básicos del TerraSAR-X.

II - Tabla 2. Características de las dos imágenes TerraSAR-X analizadas en el estudio.

II - Tabla 3. Comparación entre parámetros de oleaje derivados de los análisis SAR, calculados a través de las relaciones paramétricas de *Kahma y Calkoen* [1992] y datos colocalizados del Servicio Meteorológico Alemán (DWD).

III - Tabla 1. Sistemas de oleaje libre detectados a través de la inversión de las imágenes SAR.

III - Tabla 2. Resumen de mediciones in situ (promediadas sobre cuatro medidas consecutivas) aproximadamente coincidentes con los instantes de adquisición de las imágenes SAR $t_{\text{SAR_1}}$ (26 de febrero de 2005 a las 04:20h UTC), $t_{\text{SAR_2}}$ (2 de marzo de 2005 a las 16:20h UTC) y $t_{\text{SAR_3}}$ (18 de marzo de 2005 a las 16:17h UTC).

III - Tabla 3. Parámetros de oleaje estimados a partir de SAR, colocalizados con las mediciones in situ.

III - Tabla 4. Puntos de origen (instante de generación t_0 y distancia al instrumento de registro Δ ; de acuerdo con Snodgrass *et al.* [1966]) de los eventos de oleaje libre registrados por la boyas ASIS durante la campaña de primavera-verano 2005 en el Golfo de Tehuantepec.

III - Tabla 5. Instante de generación t_0 y distancia al origen Δ de los sistemas de oleaje libre estimados a partir de los análisis de variabilidad de longitud de onda $L_{p,n}$ a lo largo de la trayectoria de propagación a_{p_mean} obtenidos a partir de SAR.

IV. Tabla 1. Características de las imágenes SAR analizadas en este estudio.

iii. LISTA DE FIGURAS

II - figura 1. a) Localización de los gulfos de Tehuantepec, Fonseca, Papagayo y Panamá en la costa del Pacífico centroamericano. b) Ejemplo de un triple evento de vientos de chorro ocurrido el 12 de marzo de 2008 a las 6h UTC.

II - figura 2. Resultados de WAM de condiciones de oleaje local en el Golfo de Tehuantepec y Pacífico adyacente generado por vientos de chorro correspondientes al 21 de marzo de 2008 a las 0h UTC.

II - figura 3. Localización y cobertura de las dos imágenes TerraSAR-X utilizadas en el estudio.

II - figura 4. Diagrama de flujo del algoritmo empleado por el programa SeaSAR para calcular el espectro de intensidad de la imagen SAR en dos dimensiones así como el vector número de onda asociado al pico k_p correspondiente.

II - figura 5. Serie temporal de la velocidad de viento U_{10} correspondiente al evento *Tehuano* del 19–22 de marzo de 2008.

II - figura 6. Campo de viento en el Golfo de Tehuantepec durante un fuerte

evento Tehuano calculado a partir de la imagen TerraSAR-X tipo StripMap del 20 de marzo de 2008 a las 12:19h UTC.

II - figura 7. Similar a la figura 6: vectores de viento calculados de la imagen tipo ScanSAR del 21 de marzo de 2008 a las 00:19h UTC.

II - figura 8. Condiciones de oleaje durante un fuerte evento *Tehuano* calculadas a partir de la imagen tipo StripMap del 20 de marzo de 2008 a las 12:19h UTC.

II - figura 9. Similar a la figura 8: condiciones de oleaje calculadas de la imagen tipo ScanSAR del 21 de marzo de 2008 a las 00:19h UTC.

II - figura 10. Crecimiento del oleaje en condiciones de fetch limitado calculado a partir de las relaciones paramétricas de *Kahma y Calkoen* [1992] para el caso de estratificación estable: periodo asociado al pico del espectro T_p como función del fetch.

II - figura 11. Regiones donde la función de transferencia de la modulación debida al agrupamiento por velocidad R^{bunch} , cambia de lineal a no lineal (arriba y abajo de las curvas, respectivamente; de acuerdo con *Alpers et al.* [1981]).

III - figura 1. Serie temporal de la velocidad del viento U_{10} (ms^{-1}) medida por la boyas ASIS durante el proyecto INTOA.

III - figura 2. Campo de viento sinóptico U_{10} en el área de estudio obtenida a partir de la base de datos *blended QuikSCAT wind product* [CERSAT, 2002] para a) 26 de febrero de 2005 a las 6:00h UTC; b) 2 de marzo de 2005 a las 18h UTC; y c) 18 de marzo de 2005 a las 18h UTC.

III - figura 3. Localización y cobertura de los tres juegos de cuatro imágenes consecutivas ENVISAT-ASAR SLC analizadas en este estudio, correspondientes a los días a) 26 de febrero de 2005 a las 04:19–20h UTC; b) 2 de marzo de 2005 a las 16:20–21h UTC; y c) 18 de marzo de 2005 a las 16:17–18h UTC.

III - figura 4. Ejemplos de espectros de oleaje con múltiples sistemas de swell estimados a partir de dos subimágenes SAR de 256 por 256 pixeles por lado, correspondientes al 2 de marzo de 2005 y ubicadas en: a) las coordenadas 12.62° N y 95.07° W , aproximadamente a 400 km de la costa; y b) las coordenadas 16.02° N y 95.01° W sobre el anclaje de la boyas ASIS, aproximadamente a 22 km al sureste del puerto de Salina Cruz.

III - figura 5. Distribución espacial de los sistemas de oleaje lejano identificados a partir de SAR, correspondientes a los instantes de adquisición de las imágenes $t_{\text{SAR_1-3}}$: a) 26 de febrero de 2005 a las 04:19–20h UTC; b) 2 de marzo de 2005 a las 16:20–21h UTC; y c) 18 de marzo de 2005 a las 16:17–18h UTC.

III - figura 6. Mapas de longitud de onda L_p y dirección de propagación α_p obtenidos a partir de SAR, correspondientes a las diferentes particiones de oleaje identificadas en las imágenes del 26 de febrero.

III - figura 7. Mapas de longitud de onda L_p y dirección de propagación α_p obtenidos a partir de SAR, correspondientes a las diferentes particiones de oleaje identificadas en las imágenes del 2 de marzo.

III - figura 8. Mapas de longitud de onda L_p y dirección de propagación α_p obtenidos a partir de SAR, correspondientes a las diferentes particiones de oleaje identificadas en las imágenes del 18 de marzo.

III - figura 9. Gráficas de distribución conjunta de L_p y α_p de los sistemas de oleaje libre estimados a partir de SAR para las imágenes de a) 26 de febrero; b) 2 de marzo; y c) 18 de marzo de 2005.

III - figura 10. Espectros direccionales de oleaje correspondientes al 26 de febrero de 2005: a) calculado a partir de los registros de la boyas ASIS a las 04:41h UTC; b) calculado a partir de la subimágen SAR de 256 por 256 pixeles por lado, colocalizada con a); c) calculado a partir de los registros del ADCP estación *Castillo* a las 04:01h UTC; y d) calculado a partir de la subimágen SAR de 256 por 256 pixeles por lado, colocalizada con c).

III - figura 11. Espectros direccionales de oleaje correspondientes al 2 de marzo de 2005: a) calculado a partir de los registros de la boyas ASIS a las 16:45h UTC; b) calculado a partir de la subimágen SAR de 512 por 512 pixeles por lado, colocalizada con a); c) calculado a partir de los registros del ADCP estación *Espigón* a las 16:01h UTC; y d) calculado a partir de la subimágen SAR de 512 por 512 pixeles por lado, colocalizada con c).

III - figura 12. Series temporales de espectros de frecuencia $S(f)$ calculados a partir de los registros de la boyas ASIS durante el proyecto INTOA.

III - figura 13. Longitud de onda estimada a partir de SAR $L_{p,SAR}$ como función de la distancia a lo largo de su trayectoria de propagación promedio α_{p_mean} , correspondiente al sistema de oleaje $n = 2$ identificado en la imágenes del 18 de marzo.

IV - figura 1. Diagrama de flujo del algoritmo de inversión para imágenes del TerraSAR-X propuesto en este estudio.

IV - figura 2. Comparación de series temporales de la velocidad del viento U_{10} estimada por algunos modelos de simulación numérica y registrada *in situ* durante la campaña de mediciones del 2005 en el Golfo de Tehuantepec.

IV - figura 3. Comparación entre espectros 2D del oleaje calculados a partir de registros de campo y espectros aproximadamente colocalizados estimados a partir de una imagen adquirida con el SAR de banda C del satélite ENVISAT, el 2 de marzo de 2005 a las 16:20h UTC: a) $S(f,\alpha)$ calculado de mediciones de la boyas ASIS anclada aproximadamente sobre la isóbata de los 60 m; b) $S(f,\alpha)$ calculado de mediciones del ADCP estación *Espigón*, localizada a 5 km de la costa, y instalado en una profundidad de 20 m; c) y d) $S(k_x,k_y)$ calculados mediante nuestro algoritmo de inversión, aproximadamente colocalizados con a) y b), respectivamente.

IV - figura 4. Comparación entre espectros de frecuencia $S(f)$ calculados a partir de las mediciones *in situ* durante la campaña de 2005 y $S(f)_{\text{SAR}}$ calculados mediante nuestro algoritmo de inversión.

IV - figura 5. Comparación de parámetros integrales del oleaje libre calculados de acuerdo con *Collard et al.* [2005] y mediante nuestro algoritmo de inversión, correspondientes a una imagen ENVISAT-ASAR SLC del 2 de marzo de 2005:
a) Hs_{SAR} ; b) L_{p_SAR} .

IV - figura 6. Mapa de localización de las cinco imágenes TerraSAR-X utilizadas en este estudio.

IV - figura 7. Comparación entre espectros de frecuencia $S(f)$ calculados a partir de las mediciones in situ durante la campaña de 2008 y $S(f)_{SAR}$ calculados mediante nuestro algoritmo de inversión.

I. INTRODUCCIÓN

El oleaje juega un papel fundamental en los procesos asociados con la interacción entre el océano y la atmósfera, particularmente en relación a la transferencia de gases (O_2 , CO_2 , etc.) y momento a través de la superficie del mar. La evaluación adecuada de estos procesos es muy importante, por ejemplo, para contribuir al avance del conocimiento sobre la variabilidad del clima a nivel global. Sin embargo, existen limitaciones en cuanto al entendimiento de algunos fenómenos asociados con el oleaje: su generación por parte del viento, su disipación por rotura en aguas profundas¹, su propagación en medios no homogéneos (corrientes, campos de algas, estructuras, etc.), su contribución en la circulación superficial, la variabilidad que induce el oleaje sobre el esfuerzo del viento, etc. Todos estos fenómenos tienen una influencia directa en la evolución del espectro direccional del oleaje.

Enclavado en el Pacífico sur de México, el Golfo de Tehuantepec es considerado como un laboratorio natural para el estudio estos fenómenos, debido tanto a su configuración geomorfológica, como a los procesos atmosféricos, ecológicos y oceanográficos que en él se presentan. Una de sus características más relevantes es la ocurrencia de vientos de chorro (o *gap-winds*) generados por gradientes de presión atmosférica entre el Golfo de México y el océano Pacífico, que fuerzan pulsos viento a través de una

¹ conocido como *white-capping* en inglés.

discontinuidad orográfica en el Istmo de Tehuantepec, conocida como el Paso de Chivelas. Este fenómeno ha sido estudiado desde mediados del siglo XX, iniciando con los trabajos clásicos de *Brandhorst* [1958], *Roden* [1961] y *Blackburn* [1962], en los que se describe el efecto del viento sobre distintos aspectos de la dinámica del Golfo. Trabajos más recientes y, en particular, sobre la interacción entre el campo oleaje y los vientos de chorro, incluyen los de *García Nava et al.* [2009], *Romero y Melville* [2010a; 2010b] y *Ocampo-Torres et al.* [2011]. Sus resultados han sido muy relevantes para el desarrollo de este trabajo y se discutirán más adelante.

Por su parte, el radar de apertura sintética (SAR del inglés *synthetic aperture radar*) es un instrumento diseñado para adquirir imágenes multidimensionales de la superficie de la Tierra. Consiste en un sensor activo, comúnmente instalado en un avión o en un satélite, que emite un haz de microondas perpendicular a su vector de desplazamiento y con un cierto ángulo de incidencia θ respecto de la vertical; instantes después, registra el eco de la señal reflejada. Se denomina "de apertura sintética" debido a que el instrumento registra la "historia" de la señal reflejada durante un cierto tiempo de integración T_i a lo largo de su trayectoria de desplazamiento y de esta forma "sintetiza" una antena significativamente más larga que su antena real. La resolución en el sentido del desplazamiento (o *azimut*) ρ_a que es capaz de lograr el SAR es aproximadamente igual a la mitad de la longitud de su antena real y no depende de la altitud de su plataforma. Debido a la gran capacidad para adquirir

imágenes de la superficie terrestre con una alta resolución espacial, independientemente de la iluminación solar y de las condiciones climáticas, ya que su desempeño no es afectado por la cobertura nubosa, desde la década de los setenta, el SAR se ha incluido en los programas aeroespaciales de observación terrestre. En la actualidad se encuentran en operación aproximadamente una docena de SAR, formando parte de misiones patrocinadas por fondos públicos, como la del ENVISAT de la Agencia Espacial Europea (*European Space Agency*, ESA), o bien por fondos mixtos. Tal es el caso de los satélites alemanes TerraSAR-X y TanDEM-X, cofinanciados por el Centro Aeroespacial Alemán (*Deutsches Zentrum für Luft- und Raumfahrt*, DLR) y la empresa privada EADS-Astrium.

El presente documento de tesis está conformado por cinco capítulos. El primero, Introducción, incluye una sección de antecedentes sobre la estimación del oleaje mediante SAR, otra en la que se mencionan algunas de las preguntas de interés científico que han motivado esta investigación doctoral, y una más en la que se establecen los objetivos general y específicos. Los siguientes tres capítulos están conformados por tres manuscritos científicos. El primero de ellos ha sido publicado en septiembre de 2010, en el volumen 31 de la revista *International Journal of Remote Sensing*, e incluye resultados del trabajo realizado el segundo semestre de 2008 durante una estancia de investigación en el Instituto de Tecnologías en Percepción Remota (IMF) del DLR. El

manuscrito se centra en el análisis de imágenes SAR adquiridas con el satélite alemán TerraSAR-X respecto de los campos de viento y oleaje observados en el Golfo de Tehuantepec durante uno de los típicos eventos de viento intenso, conocidos localmente como *Nortes* o *Tehuanos*, en marzo de 2008. El segundo manuscrito se encuentra en revisión, e incluye resultados del trabajo realizado el primer semestre de 2008 durante una estancia de investigación en el Laboratorio de Oceanografía Espacial del Instituto Francés de Investigación para el Aprovechamiento del Mar (LOS-IFREMER). En este caso, el trabajo se centra en el análisis de la evolución espacial del espectro direccional del oleaje libre en el Golfo de Tehuantepec y océano Pacífico adyacente, estimado a partir de imágenes adquiridas por el ENVISAT-ASAR. El tercer manuscrito se encuentra en preparación, e incluye mis esfuerzos más recientes para adaptar el algoritmo de inversión desarrollado por *Lai y Delisi* [2010] con el fin de poder estimar parámetros de oleaje a partir del espectro de intensidad de la señal del SAR en banda X del satélite TerraSAR-X. El quinto capítulo integra las conclusiones generales del trabajo. La lista de referencias citadas a lo largo del texto se incluye al final del documento.

I.1. Antecedentes

Los primeros trabajos sobre la utilización de SAR para estudiar la evolución del espectro direccional del oleaje fueron publicados a principios de la década de los 1980's. *Beal* [1980; 1981] utilizó imágenes obtenidas del SAR instalado en el satélite SeaSAT² para estudiar la propagación del oleaje libre (comúnmente denominado *swell*) frente a la costa Este de los EE.UU., y demostró la factibilidad de utilizarle para medir su longitud de onda y su dirección de propagación de forma precisa. Por su parte, *González et al.* [1982] trabajaron también con imágenes del SeaSAT-SAR para estudiar el comportamiento del oleaje bajo la influencia del huracán Iva. En trabajos posteriores, *Beal et al.* [1983; 1986] analizaron la evolución del espectro en diferentes escalas y concluyeron que, pese a serias limitaciones en su capacidad de detección, el SAR tenía un enorme potencial para monitorear el oleaje de forma global. Observaron que, a lo largo de un transecto de 600 km de longitud, la dirección de propagación del oleaje mostraba una variabilidad significativa, aunque no su longitud de onda correspondiente. Así, sugirieron que tal comportamiento era debido probablemente a la interacción del oleaje con el campo local de corrientes, específicamente como respuesta a un

² El SeaSAT fue el primer satélite de observación terrestre diseñado con el fin de estudiar el océano. Fue puesto en órbita por la NASA el 28 de junio de 1978 y se mantuvo en operación durante 105 días. Debido a un fallo masivo en su sistema eléctrico, el SEASAT dejó de funcionar el 10 de octubre del mismo año. Entre los sensores que llevaba abordo se incluía el primer Radar de Apertura Sintética (de banda-L y polarización HH), además de un altímetro de radar, un escaterómetro (también llamado *dispersómetro*) de microondas y dos radiómetros: uno de luz visible e infrarrojo y otro de microondas.

remolino de mesoescala localizado a la derecha del paso del satélite. Más tarde, *Ocampo-Torres* [2001] analizó imágenes SAR adquiridas por los satélites RADARSAT y ERS-2 frente a las costas de Baja California y, utilizando técnicas de demodulación compleja, observó que la energía del oleaje variaba significativamente como función de la distancia a la costa. Concluyó que esta variabilidad era una evidencia importante del fenómeno de agrupamiento de las olas. Por otro lado, *Ocampo-Torres y Vachon* [2000] realizaron análisis del campo de oleaje asociado al huracán *Mitch* (27 de octubre de 1998), y encontraron que las variaciones espaciales del espectro direccional eran considerables, concluyendo que bajo estas condiciones de viento intenso el oleaje tenía un espectro muy ancho.

En cuanto a los efectos del viento intenso sobre el oleaje libre, a través de experimentos de laboratorio algunos trabajos [*Young y Sobey* 1985; *Peirson et al.* 2003] han demostrado que cuando se aplica un chorro de viento con dirección contraria a la de propagación de un tren de olas, éste último sufre una atenuación que suele ser proporcional a la pendiente ak y a la edad de la ola Cu^{-1} . Aquí, a se refiere a la amplitud del oleaje y es igual a la mitad de su altura H ; k es el número de onda correspondiente y es igual a $2\pi L^{-1}$; C es la celeridad de fase, definida como la razón entre la longitud L y el periodo de una onda T , y u^* es la velocidad de fricción del viento, definida como la raíz cuadrada de la razón entre el esfuerzo del viento total y la densidad del aire, $u^* = (\tau_{\text{tot}} \rho_{\text{aire}})^{0.5}$. *Peirson et al.* [2003] señalaron que los valores de atenuación observados en

laboratorio son mayores que los reportados previamente en la literatura. Concluyeron que la magnitud de la tasa de atenuación calculada en sus experimentos fue 2.5 veces mayor que la magnitud de la tasa de crecimiento asociado con el mismo forzamiento.

Por otra parte, diversos autores han demostrado la factibilidad de utilizar SAR para estimar los campos de oleaje y viento asociados con huracanes [González *et al.* 1982; Ocampo-Torres & Vachon 2000; Katsaros *et al.* 1994 y 2002; Reppucci *et al.* 2007; Lehner *et al.* 2007]. Se acepta que en estos casos el SAR presenta serias limitaciones en cuanto a su capacidad de detección: la intensidad del viento [Janssen y Alpers 2006], así como el estado del mar (asociado con la altura significante del oleaje, H_s) [Beal *et al.* 1983], limitan severamente la longitud de onda mínima detectable por SAR, particularmente para aquellas olas que se propagan en la dirección del azimut.

La interacción entre oleaje y corrientes ha sido estudiada mediante experimentos de laboratorio desde la década de los cincuenta [Sarpkaya 1955 en Kemp y Simons 1983]. En cuanto a SAR, varios investigadores han analizado el efecto de la circulación superficial sobre la evolución del espectro direccional. Beal *et al.* [1983] observaron que, a pequeña escala, la evolución del espectro seguía adecuadamente las variaciones locales de batimetría y corrientes, y demostraron que la considerable variabilidad en la dirección de propagación del espectro era probablemente debida al campo local de corrientes y, en particular, a un remolino de mesoescala detectado a la derecha

del paso del satélite. *Irvine y Tilley* [1988] analizaron la interacción entre oleaje y la corriente de Agulhas y observaron una amplificación significativa de olas sobre al norte de la corriente. Concluyeron que el oleaje incidente sobre una corriente de chorro estaría sujeto a una fuerte refracción, efecto que podría provocar un incremento en su altura. Estas conclusiones se contraponen a los resultados de *Kemp y Simons* [1983], quienes mediante experimentos de laboratorio observaron que un tren de ondas propagándose en dirección contraria a una corriente, se atenuaba significativamente. Ellos sugirieron que la dirección relativa de la corriente no influía la interacción cerca del fondo, mientras que en la superficie, las velocidades medias dependían de la dirección de propagación de las olas.

Finalmente, la interacción entre el oleaje libre y el oleaje forzado propagándose con direcciones diferentes ha sido considerada por *Snodgrass et al.* [1966] y, más recientemente, por *Violante-Carvalho et al.* [2004] y *Ardhuin y Jenkins* [2005; 2006]. Estos últimos han sugerido que la deriva de Stokes inducida por el oleaje local, o por su rompimiento en aguas profundas, pudiera ser responsable de la atenuación que sufre el oleaje libre en el océano abierto. Mencionan también que la atenuación es proporcional a la energía de la ola E , e inversamente a T y L . En cuanto a observaciones con SAR, los únicos trabajos son aquellos relacionados con huracanes: *Beal et al.* [1983] muestran que para estados de mar altos ($H_s > 2$ m), la longitud de onda mínima detectable es ≤ 200 metros; por su parte, *Ocampo-Torres y Vachon* [2000]

mencionan que la estimación de espectros con direcciones de propagación contrarias (unas con respecto de otras) en una imagen SAR del huracán Mitch, sugiere la presencia de oleaje local.

I.2. Motivación

Aunque estas investigaciones han brindado avances significativos al estado del conocimiento, sus conclusiones no pueden considerarse definitivas; por tanto, persisten el interés y la necesidad de profundizar sobre estos temas. La pregunta central que motiva este trabajo es ¿puede un chorro de viento intenso, como el que caracteriza al Golfo de Tehuantepec, afectar la propagación del oleaje libre?. En particular, ¿atenúa su energía?, ¿qué efecto tiene sobre la evolución de su espectro direccional?

Durante el desarrollo de este trabajo de tesis doctoral se han abordado algunas de estas preguntas con el fin de contribuir al estado del conocimiento sobre la influencia que tienen los vientos intensos, así como la circulación superficial que inducen, sobre la evolución del oleaje libre. Las condiciones oceanográficas particulares que caracterizan a las costas del Pacífico sur de México, destacadas por la ocurrencia de *Nortes* o *Tehuanos*, hacen que el Golfo de Tehuantepec constituya un laboratorio natural para las investigaciones que se proponen y cuyos objetivos se presentan a continuación.

I.3. Objetivos

El objetivo general de este trabajo es estudiar la evolución del espectro direccional del oleaje libre bajo condiciones de viento intenso en el Golfo de Tehuantepec y océano Pacífico adyacente a través del análisis de imágenes SAR. La evolución del espectro se determinará a partir de la variabilidad espacio-temporal de parámetros integrales como la altura significante H_s , la longitud de onda asociada al pico (o a los picos) del espectro L_p , su dirección de propagación correspondiente α_p , etc. Se propone utilizar SAR para analizar la variabilidad de los parámetros mencionados debido a su capacidad de estimar las características del oleaje libre sobre grandes superficies del océano con alta resolución espacial. Dadas las condiciones oceanográficas particulares del Golfo de Tehuantepec, y con base en las preguntas formuladas en la sección anterior, se plantean los siguientes objetivos específicos:

OE1. Estimar la variabilidad del espectro direccional del oleaje libre como resultado de la acción del viento intenso asociado con eventos *Tehuanos*.

OE2. Estimar la variabilidad del espectro direccional del oleaje libre como resultado de la acción del campo de corrientes superficiales asociado con los eventos de viento intenso en el Golfo de Tehuantepec.

Adicionalmente, con este trabajo se desea contribuir al avance del conocimiento sobre las técnicas de estimación del espectro direccional del oleaje mediante la utilización de SAR.

II. ANÁLISIS DE VIENTO Y OLEAJE EN LA COSTA DEL PACÍFICO SUR DE MEXICO UTILIZANDO IMÁGENES DEL SATÉLITE TerraSAR-X.

Artículo publicado

Díaz Méndez, G. M., S. Lehner, F. J. Ocampo-Torres, X. Li y S. Brusch [2010], Wind and wave observations off the south Pacific Coast of Mexico using TerraSAR-X imagery, *International Journal of Remote Sensing*, 31(17), 4933–4955. DOI: 10.1080/01431161.2010.485217

Resumen

Se analizan imágenes SAR de alta resolución del satélite TerraSAR-X, por primera vez, con el fin de analizar el efecto de los vientos de chorro sobre la superficie del mar en el Pacífico sur de México. Se adquirieron imágenes tipo StripMap y ScanSAR sobre el Golfo de Tehuantepec en marzo de 2008, coincidiendo con un fuerte evento de *Tehuano*, en el que se alcanzaron valores de velocidad del viento de aproximadamente 24 ms^{-1} . Aunque la variabilidad espacial de los parámetros de viento y oleaje derivados del análisis SAR fue bastante congruente con resultados de simulación numérica, los valores de la velocidad del viento derivados de este análisis fueron generalmente subestimados hasta en un 33%. Por el contrario, el algoritmo de obtención de

oleaje funcionó tan bien como para evidenciar procesos de asombramiento y refracción del oleaje libre cerca de la costa. Más aún, la evolución espacial de los picos de espectros de intensidad de la imagen sugieren la presencia de oleaje propagándose hacia el suroeste, casi alineado con los vientos de chorro. Aunque se requieren análisis adicionales, podría ser la primera vez que se detecta el crecimiento del oleaje en condiciones de *fetch*³ limitado mediante percepción remota con SAR.

³ *fetch* es un término inglés con el que comúnmente se refiere a la longitud del área de generación del oleaje.

Wind and wave observations off the south Pacific Coast of Mexico using TerraSAR-X imagery

GUILLERMO M. DÍAZ MÉNDEZ*,†, SUSANNE LEHNER‡,
FRANCISCO J. OCAMPO-TORRES§, XIAO MING LI‡
and STEPHAN BRUSCH‡

†Faculty of Marine Sciences, Universidad Autónoma de Baja California (UABC),
Ensenada, Mexico

‡Remote Sensing Technology Institute, Deutsches Zentrum für Luft-und Raumfahrt
(DLR), Oberpfaffenhofen, Germany

§Physical Oceanography Department, Centro de Investigación Científica y Educación
Superior de Ensenada (CICESE), Ensenada, Mexico

High-resolution TerraSAR-X images are analysed for the first time to investigate the effects of gap winds on the sea surface off the south Pacific Coast of Mexico. StripMap and ScanSAR scenes were acquired over the Gulf of Tehuantepec on March 2008, coinciding with a strong *Tehuano* event with a wind speed of about 24 ms^{-1} . Although spatial variability of wind and wave parameters derived from the image analysis was fairly consistent with model data, Synthetic Aperture Radar (SAR)-derived wind speed was generally underestimated by 33%. The wave-retrieval algorithm, contrastingly, performed well enough to show evidence of shoaling and refracting ocean swell close to the shore. Furthermore, spatial evolution of image intensity spectral peaks suggests the presence of wave energy propagating to the SW, closely aligned with the offshore winds. Although further analyses are required, it could be the first time that growing waves in fetch-limited conditions have been detected through SAR remote sensing.

1. Introduction

On 15 June 2007, TerraSAR-X was successfully launched from Baikonur Cosmodrome, Kazakhstan, and acquired its first Synthetic Aperture Radar (SAR) image just four days later. Designed to orbit the Earth sun-synchronously at a nominal height of 514.8 km, it is the first of two Earth Observation (EO) satellites developed through a public-private partnership: the German Aerospace Centre and the European Aeronautical Defence and Space (EADS)-Astrium, respectively. The satellite is 4.9 m long, which is also the length of the SAR antenna, and has a diameter of 2.5 m. Its inclination is 97.44° with respect to the Earth's equator, and thus its revisit cycle is 11 days. The onboard SAR sensor emits radar pulses at a frequency of 9.65 GHz. TerraSAR-X's SAR has been designed to acquire images within four basic imaging modes: ScanSAR (SC), StripMap (SM), Spotlight (SL) and High Resolution Spotlight (HS). Table 1 summarizes their main characteristic parameters: while SM mode is the standard imaging mode of all, SC provides the largest coverage. SL and HS modes use phased array beam steering in the azimuth direction to increase the size of the synthetic aperture, which in turn, results in a higher azimuth resolution ρ_a at the

*Corresponding author. Email: gdiaz@uabc.mx

Table 1. Characteristic parameters of TerraSAR-X basic imaging modes.

	Imaging modes		
	ScanSAR	StripMap	Spotlight
Swath width (km) (ground range)	100	30 sp; 15 dp	10
Product length (km) (ground range)	150	50	10
Incidence angle θ range ($^{\circ}$)	20–45	20–45	5
Azimuth resolution ρ_a (m)	18.5	3.3 sp; 6.6 dp	20–55
Ground range resolution ρ_r (m)	1.70–3.49 ($\theta = 45$ –20°)	1.70–3.49 ($\theta = 45$ –20°)	1.7 sp; 3.4 dp 1.48–3.49 ($\theta = 55$ –20°)
Polarizations	single: HH or VV dual: HH/VV, HH/HV, VV/VH	single: HH or VV dual: HH/VV, HH/HV, VV/VH	single: HH or VV dual: HH/VV

sp = single polarization; dp = dual polarization.

cost of azimuth scene size. Additional information on TerraSAR-X's instrument, basic products and data structure can be found in Fritz and Eineder (2008).

Evaluation of atmospheric and oceanic processes through the analysis of SAR imagery is based on the principle that these phenomena modulate the distribution and behaviour of the capillary-gravity waves. Such waves are generated by the shear stress of the wind τ_w acting upon the sea surface; since very light winds suffice to generate these ripples, the latter are assumed to be omnipresent on the ocean surface. Capillary-gravity waves interact with the microwave pulses emitted by the SAR through Bragg resonance, the result of which is measured by the SAR antenna as the radar backscattered signal or image brightness. The wavelengths of the backscattering elements span 1–40 cm, and depend on the microwave frequency and its angle with respect to the vertical (i.e. incidence angle θ). Assembling or spreading of these ripples by increasing wind stress, tilting of the sea surface due to ocean swell, or converging/diverging of water masses for example, creates distinct patterns on the sea-surface roughness that can be imaged by SAR systems as spatial variations of the radar brightness. Given the fact that surface tension is the restoring force of capillary waves, natural or anthropogenic surfactants are also capable of modulating the radar backscatter from the ocean.

Assessments of the wind field and the sea state over large areas of the open ocean have been performed through the analysis of space-borne SAR under calm-weather conditions (Vesecky and Stewart 1982, Beal *et al.* 1983, 1986, Vachon and Dobson 1996) and extreme-weather conditions (Katsaros *et al.* 2002, Horstmann *et al.* 2006, Li *et al.* 2008, Reppucci *et al.* 2008), with promising results. SAR image analyses have delivered detailed information on the spatial variability of winds and waves in coastal areas (Johannessen *et al.* 1996, Ocampo-Torres 2001, Ocampo-Torres *et al.* 2007, Díaz Méndez *et al.* 2008). High-resolution wind maps derived from larger coverage SAR imagery are highly regarded by the wind farming industry because improved wind maps are desirable for resource assessment, offshore-site selection, etc. (Hasager *et al.* 2007, Brusch *et al.* 2008). SAR has become very important for the study of processes that are difficult to evaluate such as the interaction between ocean waves and sea-surface currents (Irvine and Tilley 1988, Ouchi 1994), formation and evolution of internal waves (Hwang *et al.* 2008) and the synoptic estimation of sea-surface circulation (Collard *et al.* 2008).

Hasselmann and Hasselmann (1991) derived a nonlinear integral transformation relation to describe the mapping of a two-dimensional ocean wave spectrum into a SAR image spectrum; an inversion of the proposed relation yielded the possibility of estimating the two-dimensional (2D) wave spectrum from any given SAR image spectrum. A few years later, additional inversion schemes were proposed to derive wave parameters from the few EO space-borne SAR sensors launched from 1978 onwards (Krogstad *et al.* 1994, Engen and Johnsen 1995, Hasselmann *et al.* 1996, Hasselmann *et al.* 1998, Mastenbroek and de Valk 2000). Improved algorithms (Schulz-Stellenfleth and Lehner 2004, Schulz-Stellenfleth *et al.* 2005, Collard *et al.* 2005) have been used by research institutions to derive sea-surface elevation, compute global statistics with either the full (or just the lower wavenumber part of the) wave spectrum, associated with the ocean swell, derived from the C-band SARs onboard the European satellites ERS-1, -2 and ENVISAT.

In this context, the X-band SAR mounted onboard TerraSAR-X has the potential to give new information on the sea surface because the nonlinearity and azimuthal cutoff described by Hasselmann and Hasselmann (1991) depend on the sensor's altitude. Given its relatively low flying orbit, TerraSAR-X is capable of observing features on

the sea surface not imaged by the L- nor C-band SAR sensors flying at approximately 800 km above sea level, like the above-mentioned European satellites, the Canadian Radarsat-1 and -2 and the Japanese Earth Resources satellite JERS-1 and the Advanced Land Observation Satellite ALOS. TerraSAR-X's imagery has thus been applied to ocean research right after the first scenes were available. Li *et al.* (2009) used Spotlight and StripMap scenes to analyse wave refraction and diffraction around Terceira Island at the Azores. Lehner (2008, personal communication) used SC, SM and SL mode scenes to derive high-resolution wind fields over the open ocean. Contrastingly, Brusch *et al.* (2010) took advantage of TerraSAR-X SAR's high spatial resolution to include them in ship surveillance and security applications.

The main objective of this study has been to investigate, through the analysis of high-resolution TerraSAR-X imagery, the detailed spatial evolution of the wind and wave fields during *Tehuano*-event conditions at the Gulf of Tehuantepec and adjacent Pacific Ocean. Evolution of the swell wave spectrum has been estimated by various authors through changes of spectral density (Ocampo-Torres 2001, Ardhuin *et al.* 2003), propagation direction and directional spreading (Beal *et al.* 1986, Ocampo-Torres and Vachon 2000, Ardhuin *et al.* 2003). Hence, our specific objectives included the assessment of the SAR image spectrum variability presumably induced by the strong gap winds, as well as an assessment of the spectral evolution and spatial variability of the fetch-limited wind-sea generated locally by the gap winds. It has also been of interest to investigate the spatial structure and variability of the wind field and general sea state during these strong-wind conditions.

The following sections include, first, a brief description of the *Tehuano* gap winds and their effect on the ocean surface off the south Pacific Coast of Mexico. This is followed by some theoretical background and by a short introduction on how the wind field and ocean waves were derived from the SAR images. Analysis results are presented and discussed in §4, while §5 includes a summary of findings.

2. Gap winds and their effect on the ocean surface

The Gulf of Tehuantepec located at the south Pacific Coast of Mexico, as well as the gulfs of Fonseca, Papagayo and Panama located in Central America (see figure 1(a)) are characterized by the occurrence of strong gap winds blowing off-shore into the Pacific Ocean during late autumn, winter and early spring months. According to Chelton *et al.* (2000), gap winds are the result of an atmospheric pressure gradient of up to 5 hPa between the Pacific and the Gulf of Mexico and western Caribbean, which forces up to three jets of wind through distinct low-elevation topographic discontinuities on the otherwise high mountain ranges. The resulting jets are usually colder and drier than the surrounding Eastern Tropical Pacific air. Figure 1(b) shows an example of a triple gap wind event that occurred on 12 March 2008 at 06h Coordinated Universal Time (UTC) (source: European Centre for Medium-Range Weather Forecasts (ECMWF) blended QuikSCAT wind product; CERSAT 2002). The two southern jets have also been associated with funnelling of the trade winds through the mountain gaps in Nicaragua and Panama.

South-blown gap winds occurring at the Gulf of Tehuantepec are locally known as *Tehuanos*. *Tehuano* events usually last from a few hours up to a few days, often reaching sustained velocities above 20 ms^{-1} and blowing as far south as 10° N latitude. Depending on duration and intensity, these events may induce a series of oceanographic phenomena, including strong offshore surface currents whose intensities have been

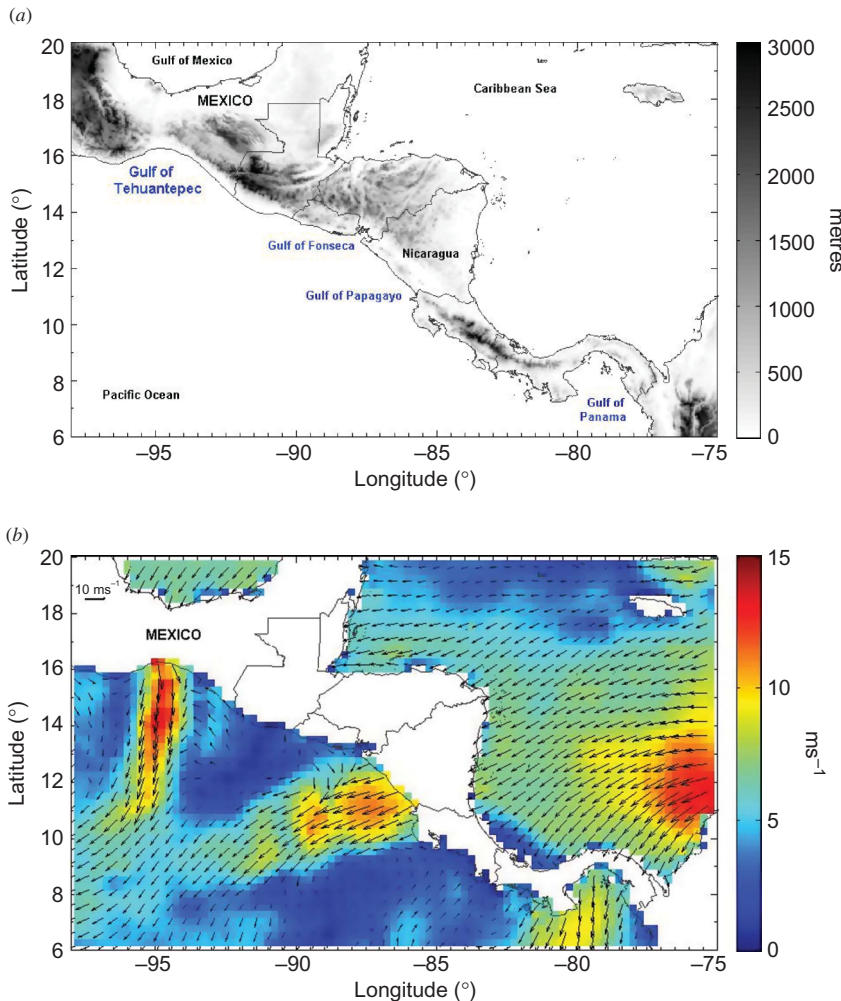


Figure 1. (a) Location of the gulfs of Tehuantepec, Fonseca, Papagayo and Panama in the Pacific Coast of Central America. Shades of grey represent topographic elevations in metres above sea level. (b) Example of a triple gap-wind event that occurred on 12 March 2008 at 06h UTC. Colour code is ms^{-1} . Source of wind data: ECMWF blended QuikSCAT wind product. Source of topographic data: NOAA- GGDC ETOPO-2 Global Gridded 2-minute Database.

measured as high as 1.5 ms^{-1} (Durazo 2009, personal communication), cooling of the sea-surface temperature, depression of the sea level of a few centimetres (Álvarez *et al.* 1989), as well as the generation of fetch-limited wind-sea propagating offshore (Ocampo-Torres *et al.* 2007, Díaz Méndez *et al.* 2008, García-Nava *et al.* 2009).

Figure 2 shows WAM (WAve Model; WAMDI 1988) results of wind-sea waves generated by persistent *Tehuanos* on 21 March 2008 at 00h UTC (model results provided by the German Weather Service, DWD). While shades of blue represent significant wave height H_s in metres, red arrows correspond to vectors of spectral peak wavelength L_p and its associated propagation direction α_p . Maximum computed values were $H_s = 5.1 \text{ m}$ and $L_p = 126.3 \text{ m}$. According to the same source of data, wind speed at these location reached $U_{10} = 20.3 \text{ ms}^{-1}$.

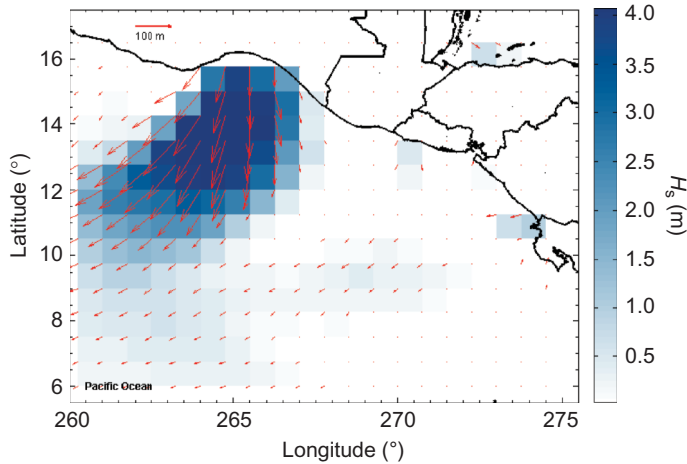


Figure 2. WAM results of wind-sea wave conditions at the Gulf of Tehuantepec and adjacent Pacific Ocean generated by the off-shore blowing gap winds on 21 March 2008 00h UTC: significant wave height H_s values in shades of blue; peak wavelength L_p and associated propagation direction α_p as red arrows. Source: DWD wind and wave data.

Strong *Tehuano* events are believed to induce variability on the evolution of the incoming waves generated by distant storms. Detailed analysis of the 2D wave spectra should provide evidence of ocean-swell variability due to refraction induced by surface currents, broadening or narrowing of the directional spreading and transfer of energy induced by the wind, particularly for larger swell wavenumbers. A number of authors (Snodgrass *et al.* 1966, Violante-Carvalho *et al.* 2004, Arduin and Jenkins 2005, 2006, Arduin *et al.* 2007) have considered the interaction between ocean swell and wind-sea propagating in opposite directions, and believe it may induce attenuation of the swell energy in deep waters.

3. Detection of wind and wave fields from TerraSAR-X imagery

3.1 Theoretical background

Estimation of the wind field within Deutsches Zentrum für Luft- und Raumfahrt (DLR)'s SeaSAR © Toolbox (DLR, Oberpfaffenhofen, Germany) is based on an empirical relation proposed by Masuko *et al.* (1986), who associated the normalized radar cross section (NRCS) σ_0 of a radiometrically calibrated SAR image to the wind speed 10 m above the sea surface U_{10} , the incidence angle of the radar beam θ and the azimuth angle φ between the wind direction and the SAR look direction. Depending also on polarization p and on the SAR wavelength λ , it is logarithmically expressed by:

$$\sigma_0(\lambda, p, U, \theta, \varphi) = 10[G(\lambda, p, \theta, \varphi) + H(\lambda, p, \theta, \varphi) \log_{10} U], \quad (1)$$

where σ_0 is given in dB. The values of G and H were found empirically and varied from -2.82 to -5.63 and from 1.62 to 2.82, respectively for a 10 GHz radar system with $\theta = 30^\circ$ - 60° and HH polarization, and from -2.76 to -4.59 and 1.54 to 2.48, respectively for VV polarization. The azimuth angle φ may be determined directly from the SAR imagery through Fast Fourier Transform (FFT) analysis or observation of wind streaks and other wind-induced processes on the sea surface, as well as input from external sources such as ship anemometers, spaceborne scatterometers or numerical models.

Similar to other geophysical model functions (GMFs), the X-MOD needs be inverted to derive U_{10} for given values of λ , p and θ . Following the CMOD4 (Stoffelen and Anderson 1997) and CMOD5 (Hersbach *et al.* 2004) algorithms derived for the C-band scatterometer onboard ERS-1, the X-band inversion is given by:

$$\sigma_0(U, \theta, \varphi) = x_0 + x_1 U + x_2 \sin(\theta) + x_3 \cos(2\varphi) + x_4 U \cos(2\varphi), \quad (2)$$

where x_n are coefficients tuned empirically from a set of 166 Spaceborne Imaging Radar- C/X-Band Synthetic Aperture Radar (SIR-C/X-SAR) and 52 TerraSAR-X images (Ren and Lehner 2008, personal communication).

Regarding the sea state, Schulz-Stellenfleth and Lehner (2004) described the SAR imaging of ocean waves as dominated by two mechanisms: the modulation of the NRCS by long waves (i.e. waves longer than the SAR resolution cell) through tilt and hydrodynamic processes in the ocean surface, and by Doppler shifts of the backscattered signal associated with the orbital motion of ocean waves. This latter mechanism is commonly referred to as velocity bunching. Tilt and hydrodynamic modulation of the NRCS, also called real aperture radar (RAR) modulation I^{RAR} , is a function of space $\mathbf{x}(x, y)$ and time t , and is usually described by a simple linear model such as

$$I^{\text{RAR}}(\mathbf{x}, t) = \frac{\sigma_0(\mathbf{x}, t) - \langle \sigma_0 \rangle}{\langle \sigma_0 \rangle}, \quad (3)$$

where $\langle \sigma_0 \rangle$ represents the ensemble-averaged value of the NRCS. Based on a Fourier representation of the ocean-surface elevation η at time t :

$$\eta(\mathbf{x}, t) = 2\text{Re} \left(\sum_k \eta_k e^{i(kx - \omega_k t)} \right), \quad (4)$$

where Re denotes the real part of the Fourier transform, \mathbf{k} is the wavenumber vector, η_k are the complex Fourier coefficients of the sea surface and ω_k is the angular wave frequency that is associated with \mathbf{k} through the so-called dispersion relation. By combining equations (4) and (3), I^{RAR} can be rewritten as:

$$I^{\text{RAR}}(\mathbf{x}, t) = 2\text{Re} \left(\sum_k T_k^{\text{RAR}} \eta_k e^{i(kx - \omega_k t)} \right), \quad (5)$$

where T_k^{RAR} is the RAR modulation transfer function (MTF). As noted by these authors, there is still some uncertainty on the exact phase and magnitude of the RAR MTF.

SAR imaging processes uses the phase history of the radar backscattered signal, distorted by the Doppler shifts induced by the wave motions, to synthesize the resolution in the azimuth direction. Since the ocean surface is not stationary, a slant range component of the average orbital velocity u_r during the SAR integration time (usually 1 s), causes shifting ξ of the respective image point in the azimuth direction. This shifting equals the distance from the SAR antenna to the ocean target or slant range R times u_r divided by the satellite velocity V . In a linear approximation, u_r can be expressed in terms of the wave spectrum as:

$$u_r(\mathbf{x}, t) = 2\text{Re} \left(\sum_k T_k^u \eta_k e^{i(kx - \omega_k t)} \right), \quad (6)$$

where T_k^u is the orbital velocity transfer function given by:

$$T_k^u = -\omega_k \left(\frac{k_y}{|k|} \sin \theta + i \cos \theta \right), \quad (7)$$

and k_y is the wavenumber in the azimuth direction. Based on equations (5) and (7), the following integral expression can be derived for a SAR image MTF I^{SAR} of a moving sea surface:

$$I^{\text{SAR}}(\mathbf{x}) = \frac{\sqrt{\pi}}{2\rho_a} \int (1 + I^{\text{RAR}}(\mathbf{x}')) e^{-\frac{\pi^2}{4\rho_a^2}(x-x'-\xi(x'))^2} \delta(y' - y) dx' dy' - 1. \quad (8)$$

Here, $\mathbf{x}(x, y)$ and $\mathbf{x}'(x', y')$ denote the coordinates of the image in the Cartesian and the ocean planes, respectively.

3.2 Data

More than a dozen scenes have been acquired so far by the TerraSAR-X over the Gulf of Tehuantepec. In this paper, however, we present results from the two that coincide with the occurrence of a strong *Tehuano* event. This small dataset included a higher resolution SM scene from 20 March 2008 at 12:19h UTC and a larger coverage SC acquired 12 hours later. Characteristics of these two scenes are summarized in table 2; their location and extent are shown on a map in figure 3. This map also shows bathymetric contours at the Gulf of Tehuantepec and the adjacent Pacific Ocean.

Table 2. Characteristics of the two TerraSAR-X images analysed in this study.

Imaging mode	Date and time (UTC)	Path	Track azimuth	Polarization	Coverage (km)
StripMap	20 March 2008 @ 12:19h	Descending	348.6°	HH	30 × 50
ScanSAR	21 March 2008 @ 00:19h	Ascending	191.4°	HH	100 × 150

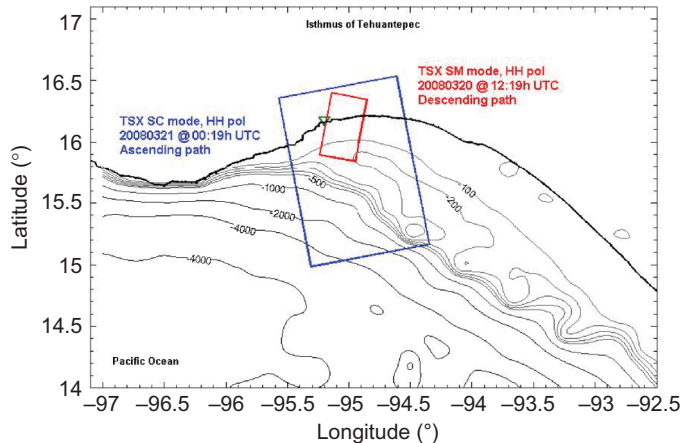


Figure 3. Location and extent of the two TerraSAR-X images analysed in this study. The red rectangle depicts the perimeter of the SM scene acquired on 20 March 2008 at 12:19h UTC; the blue rectangle depicts the perimeter of the SC acquired on 21 March. The small green triangle marks the location of the Port of Salina Cruz. Also shown are bathymetric contours from the Gulf of Tehuantepec and the adjacent Pacific Ocean.

3.3 Method

As mentioned above, estimation of the wind field from TerraSAR-X imagery was based on the X-MOD GMF. While values of θ are given for each pixel on the image annotation file, the azimuth direction ϕ was derived by visual observation of wind streaks and other distinct patterns directly on the image quicklooks; according to Reppucci *et al.* (2008), they tend to align fairly well with the direction of the wind. In their paper, these authors present a flow chart depicting the steps followed to calculate the wind speed using the CMOD5 GMF. In our case, we followed similar steps, but applied the X-MOD instead.

Ocean-wave conditions were derived through the analysis of SAR image intensity spectra since no inversion algorithm has been yet proposed nor validated for the TerraSAR-X SAR. A mosaic of spectra was computed from each scene and its corresponding peak wavenumber k_p was calculated following the steps depicted in the flow chart included in figure 4.

Within the SeaSAR Toolbox, a given image is first read and its corresponding quicklook is created. Before it is processed for wind or waves, the scene is calibrated and, if appropriate, a land mask is applied. A value for sub-image size is input by the

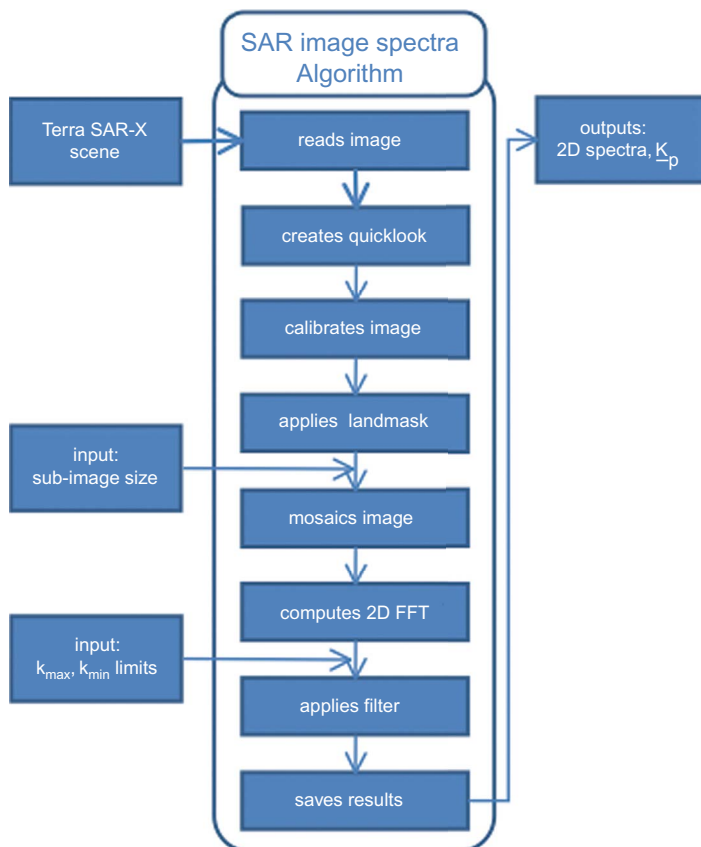


Figure 4. Flow chart of the algorithm followed by the SeaSAR toolbox to compute the two-dimensional SAR image intensity spectrum and its corresponding peak wavenumber k_p .

user and the image is tiled accordingly. A 2D FFT is performed on each sub-image; the result is filtered using maximum and minimum wavenumber limits, usually $k_{\max} = 0.09 \text{ rad m}^{-1}$ and $k_{\min} = 0.01 \text{ rad m}^{-1}$, respectively, which roughly correspond to ocean waves with deep-water wavelengths $L_{\min} = 70 \text{ m}$ and $L_{\max} = 600 \text{ m}$, respectively. These limits however, can be conveniently modified by the user. The resulting matrix is then stored for post-processing, plotting and estimation of k_p . It is worth mentioning that, for our analyses, the wavenumber limits were set to $k_{\max} = 0.063 \text{ rad m}^{-1}$ and $k_{\min} = 0.02 \text{ rad m}^{-1}$ for the SM scene and $k_{\max} = 0.04 \text{ rad m}^{-1}$ and $k_{\min} = 0.01 \text{ rad m}^{-1}$ for the SC, which correspond to shoaling waves with wave periods T of the order of 8–14 s in the first case and $T = 10$ –20 s in the second, typical for ocean swell.

4. Results and discussions

According to ECMWF blended QuikSCAT wind data (CERSAT 2002), a strong gap wind event developed at the Gulf of Tehuantepec late on 19 March 2008. Figure 5 shows a time series plot of wind speed U_{10} extracted from this dataset at three locations: P1 ($16.125^\circ \text{N}, 94.875^\circ \text{W}$), P2 ($15.375^\circ \text{N}, 95.125^\circ \text{W}$) and P3 ($14.625^\circ \text{N}, 95.375^\circ \text{W}$), located approximately 10, 100 and 185 km offshore (along the wind-jet axis), respectively. As can be seen on the graph, the *Tehuano* event quickly intensified, reaching velocities of up to 23 ms^{-1} about 100 km offshore (point P3) on 20 March. Contrastingly, closer to the shore (P1), wind-speed variability was less pronounced. The *Tehuano* decreased down to 5 ms^{-1} late on 21 March before intensifying again the next day. By noon, it reached a second intensity peak, registering wind-speed values above 10 ms^{-1} . The vertical arrows in figure 5 represent the times of acquisition of the two analysed TerraSAR-X images, which as can be noted, correspond to the period of stronger winds. Wind-speed values derived from the 21 March ScanSAR scene, collocated to locations P1 and P2, are included for comparison.

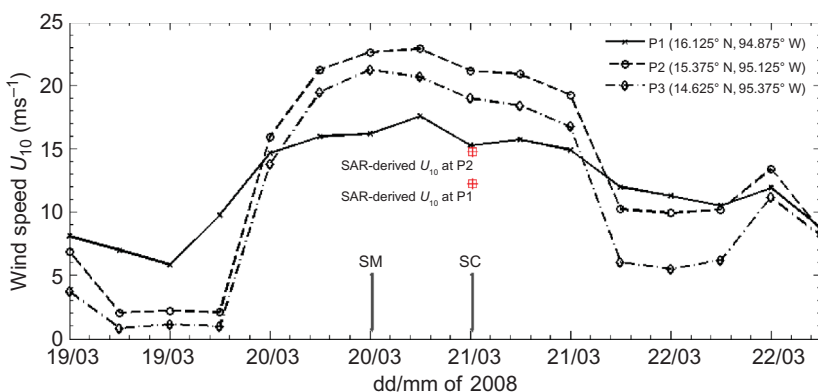


Figure 5. Time series of wind speed U_{10} during the 19–22 March 2008 *Tehuano* event. Points P1, P2 and P3 are located ca. 10 km, 100 km and 185 km away from the shore along the wind-jet axis, respectively (source: ECMWF blended QuikSCAT wind data; CERSAT 2009). The vertical arrows indicate the time of acquisition of the two analysed TerraSAR-X images; red squares indicate wind speed collocated to points P1 and P2 derived from the 21 March 2008 ScanSAR scene.

4.1 SAR-derived wind and wave parameters

Conspicuous wind streaks and other wind-related features of various scales were appreciated by visual inspection on both TerraSAR-X images (figures 6 and 7). Alternating bright and dark patterns extending perpendicular to the shore were observed on the ocean surface as well as on Tehuantepec's coastal lagoons. Larger scale oscillations, presumably atmospheric gravity waves, were observed on the SC scene, apparently propagating perpendicular to the shore.

All these features were used to carefully derive the wind direction α and its angle ϕ with respect to the SAR look direction ψ , required by the X-MOD GMF in order to solve for the wind speed. Once this has been input in the Toolbox, vector fields of wind speed and direction were constructed. Figure 6 shows a map of the estimated wind

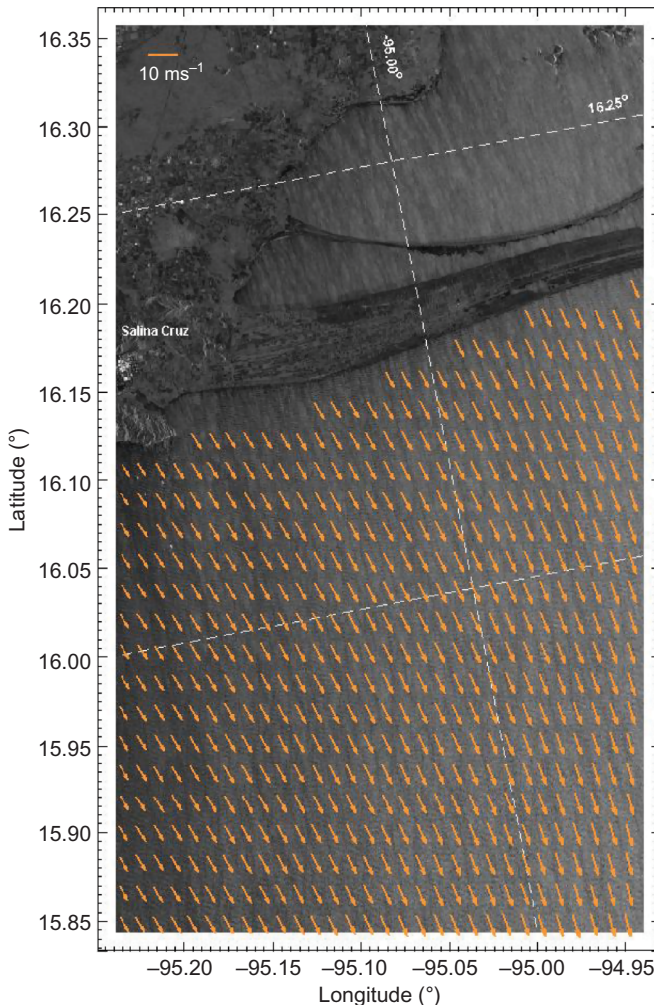


Figure 6. Wind field at the Gulf of Tehuantepec during a strong *Tehuano* event derived from the SM scene acquired on 20 March 2008 at 12:19h UTC. Meridians and Parallels shown as dashed lines.

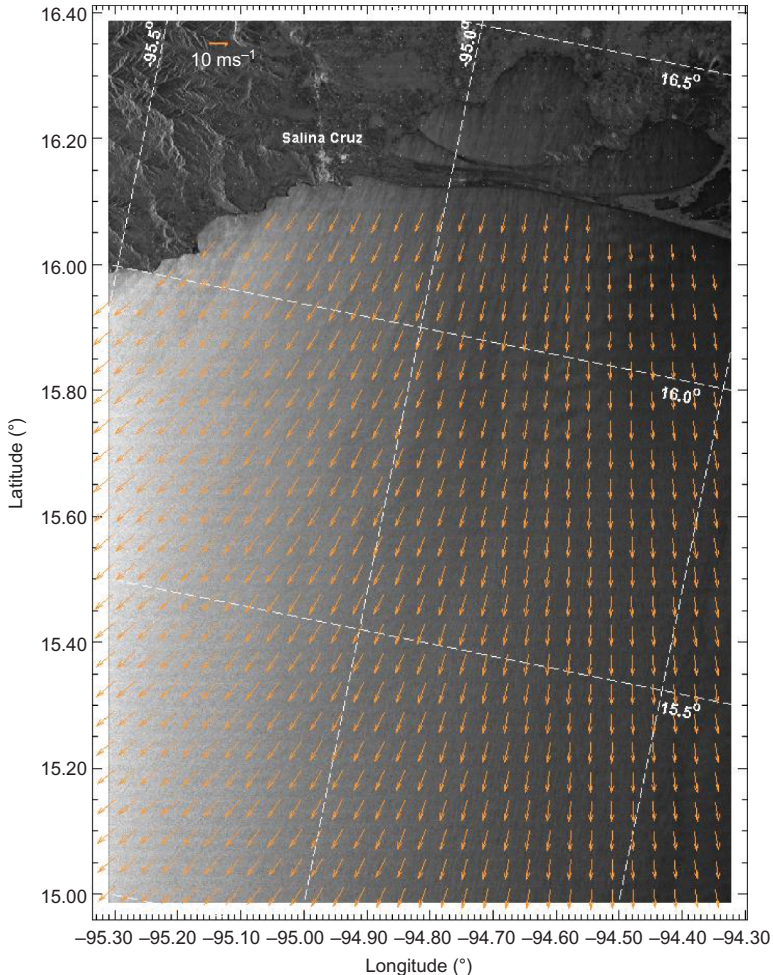


Figure 7. Similar to figure 6: wind vectors derived from the SC scene acquired on 21 March 2008 at 00:19h UTC.

field overlaid on top of a quicklook from the 20 March SM scene. The SAR quicklook is oriented according to the platform flight direction and thus, it points to the top of the page; Meridians and Parallels are shown as dashed lines. Looking carefully, it can be noted that the wind was strongest towards the core of the jet, which laid to the right of the scene; but it also increased away from the coast. SAR-derived wind-speed values retrieved by the X-MOD algorithm range from $U_{10} = 10.5 \text{ ms}^{-1}$ at the left end of the scene to $U_{10} = 15.0 \text{ ms}^{-1}$ on the right, and from $U_{10} = 8.4 \text{ ms}^{-1}$ just off-shore from the port of Salina Cruz to $U_{10} = 15.2 \text{ ms}^{-1}$, 42 km to the southeast. Average wind speed estimated for this scene was $U_{10} = 13.3 \text{ ms}^{-1}$. Similarly, figure 7 shows the wind retrieved from the SC image acquired on 21 March. This larger coverage scene (see table 2) renders a better detail of the fan-shaped spatial distribution of the wind field in the area as described by Chelton *et al.* (2000). It is interesting to observe that the wind streaks on the ocean surface are oriented to the south-southwest, contrasting to those in figure 6, which lay to the south-southeast. This suggests the rotation of the

wind-jet axis as the *Tehuano* event progresses. Because a larger extent of the wind jet is covered by this SC scene, corresponding wind-speed statistics are slightly higher than those estimated from the SM scene: in this case, the higher values are located to the left of the figure and range from $U_{10} = 10.4\text{--}16 \text{ ms}^{-1}$, with average $U_{10} = 13.8 \text{ ms}^{-1}$.

SAR-derived wind values, however, were relatively lower than collocated grid points from the blended QuikSCAT wind data of figure 5. The latter range from $U_{10} = 18.8\text{--}21 \text{ ms}^{-1}$ for 20 March and $10\text{--}21.1 \text{ m s}^{-1}$ for 21 March, with averages of 20 ms^{-1} and 16.8 ms^{-1} , respectively, at the areas covered by the SAR images. According to Ren and Lehner (2008, personal communication), the X-MOD algorithm implemented in the Toolbox has been tuned with a limited number of strong-wind cases and thus, this could be one reason for the underestimation of wind-speed values. Another important cause may be that the X-MOD algorithm was tuned for VV polarization images, and both scenes analysed on this study are HH polarized, which is known to produce weaker backscatter. As discussed by Horstmann *et al.* (2000), additional sources of error include the dependence of the NRCS on the radiometric accuracy of the SAR product, which led to large errors on wind speed, particularly in the case of high wind speeds and small incidence angles. Furthermore, Donelan and Pierson (1987) found that for high wind speeds, σ_0 becomes less sensitive to the wind speed and then decreases as the wind speed increases.

Underlying all the above-mentioned wind-related features, a distinct pattern of shorter wavelength texture associated with ocean waves was observed on the images. Due to its higher resolution, it was particularly evident on the SM scene where at least two sets of wavy features, presumably two ocean-swell systems with different propagation direction, crossed each other and eventually aligned close to the shore. Figure 8(a) shows a map with results from the SeaSAR Toolbox's wave-detection algorithm overlaid on the 20 March 2008 SM scene.

As can be seen in the figure, most of the double-headed vectors representing the wavelength L_p and ambiguous propagation direction α_p of the ocean waves have a quasi-northerly orientation. It was not possible to perform the 180° ambiguity discrimination due to the fact that the scenes were not acquired in complex mode, and thus, no information on the phase of the scatters was available. Nevertheless, given their magnitude and proximity to the coast, it was not difficult to infer that propagation direction was towards the coast. The progressive shortening of the vectors from the bottom of the scene towards the shore represents a decrease in wavelength from approximately $L_p = 330 \text{ m}$ down to about $L_p = 190 \text{ m}$. The latter, along with the shifting in propagation direction α_p , is presumably accounted for by the combined phenomena of wave refraction and shoaling due to decreasing water depth towards the coast. Indeed, as can be seen in figures 3 and 8(a), the water depth at the southern end of the SM scene reaches 200 m, and decreases gently towards the shore.

Figures 8(b)-(d) show a set of 2D SAR image intensity spectra calculated from the three ca. $5 \times 5 \text{ km}$ (2048×2048 pixels) sub-images shown as red squares in figure 8(a). Horizontal and vertical axes are range and azimuth wavenumbers k_x and k_y , respectively, in rad m^{-1} . Colour coding on these plots represents normalized values of image intensity from the 2D FFT, which may be associated with the energy of the ocean waves as suggested by Alpers *et al.* (1981) through

$$S(\mathbf{k}) = \frac{S_I(\mathbf{k})}{(I^{\text{SAR}}(\mathbf{k}))^2}, \quad (8)$$

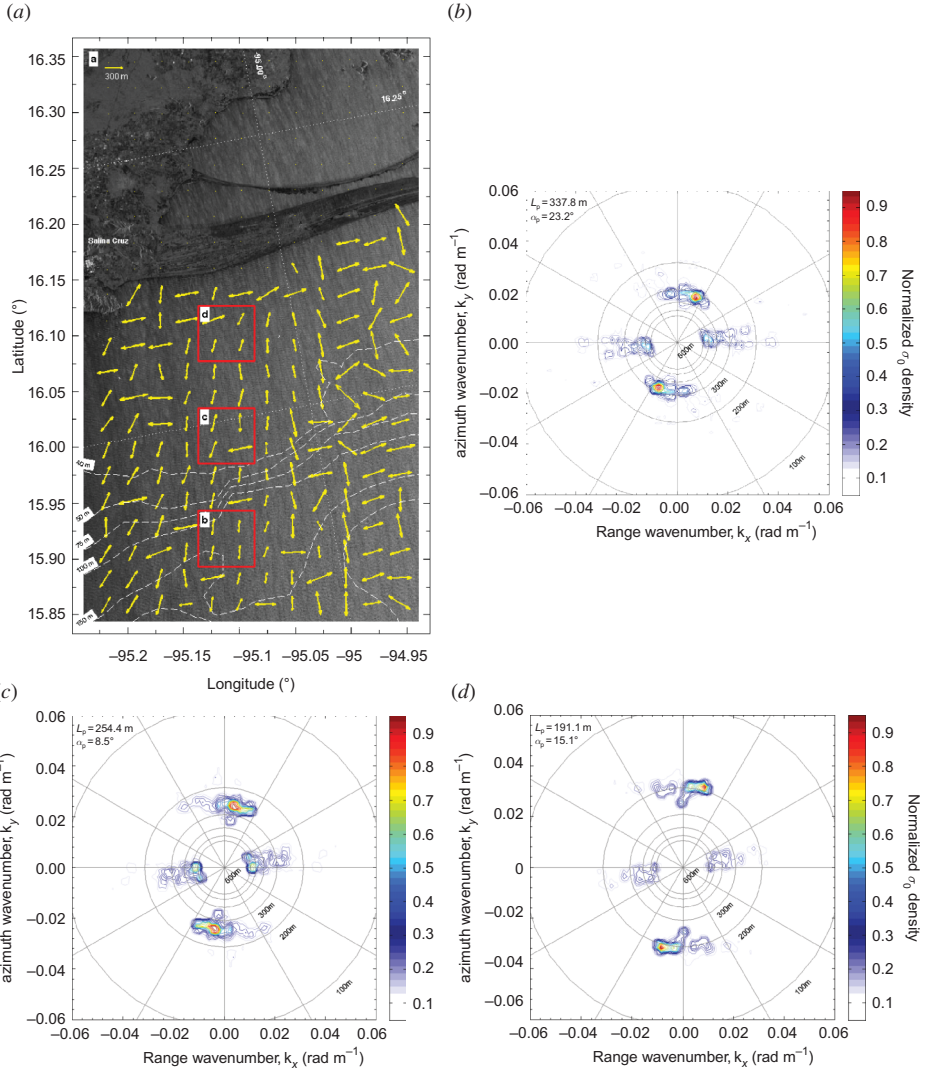


Figure 8. Ocean-wave conditions during a strong *Tehuano* event derived from the SM scene acquired on 20 March 2008. (a) Estimated SAR-image peak wavelength L_p in yellow; two-head arrows represent wave propagation direction with 180° ambiguity. Meridians and Parallels shown as dashed lines; bathymetric contours above 40 m of water depth shown as solid white lines. (b)–(d) Two-dimensional SAR-image intensity spectra calculated from the three ca. 5×5 km sub-images shown as red squares on (a); (d) is closer to the shore. Horizontal and vertical axes are range and azimuth wavenumbers, k_x and k_y , respectively, in rad m $^{-1}$.

where $S(\mathbf{k})$ is the ocean wave spectrum as a function of wavenumber \mathbf{k} , $S_I(\mathbf{k})$ is the intensity spectrum of the SAR image and $I^{\text{SAR}}(\mathbf{k})$ is the SAR MTF corresponding to a linear mapping of the ocean surface. As can be observed on these spectra, a series of high-intensity peaks was estimated by the SeaSAR algorithm. While peaks closely aligned with the horizontal axis ($k_y \approx 0$, $k_x \approx \pm 0.012$ rad m $^{-1}$) were associated with sea-surface roughness patterns induced by the wind, those located close to the vertical

axis ($k_y \approx \pm 0.02\text{--}0.035 \text{ rad m}^{-1}$, $k_x \approx 0$) are believed to be associated with the ocean swell. Phenomena of wave refraction and shoaling mentioned above were also noted on these spectra, as the latter peaks shifted from close to the $L = 300 \text{ m}$ past the $L = 200 \text{ m}$ contours, closer to the shore. Overall shift from these peaks from $L_p = 337.8 \text{ m}$ in figure 8(b) to $L_p = 191.1 \text{ m}$ in figure 8(d) ($k_p = 0.018 \text{ rad m}^{-1}$ to $k_p = 0.032 \text{ rad m}^{-1}$) represent a wavelength decrease of ca. 45% and change in propagation direction of 8° ($\alpha_p = 23.2\text{--}15.1^\circ$).

A similar type of analysis was applied to the SC scene from 21 March 2008. Figure 9 shows the results for 1024×1024 pixel sub-images. A wavelength filter was set to detect intensity peaks within $L = 70\text{--}600 \text{ m}$, which approximately correspond to wave periods of $T \approx 7\text{--}20 \text{ s}$, typical for ocean swell. Arrows on the left half of the scene represent wavelengths of the order of $L_p = 250 \text{ m}$, and are consistent in orientation and length with the incoming swell from the WAM results described in §2. Figures 9(b)-(d) show 2D SAR image spectra calculated for the ca. $17 \times 17 \text{ km}$ (2048×2048 pixels) sub-images shown as red squares in figure 9(a). Though one can hardly appreciate shoaling and refraction of the peaks associated with the swell waves on these spectra ($L_p \geq 300 \text{ m}$), shifting of those located outside the $L = 200 \text{ m}$ contour ($k_x = k_y = 0.031 \text{ rad m}^{-1}$) is far more noticeable.

These secondary peaks with relatively higher wavenumbers ($k_{p-b} = 0.061 \text{ rad m}^{-1}$, $k_{p-c} = 0.063 \text{ rad m}^{-1}$ and $k_{p-d} = 0.073 \text{ rad m}^{-1}$, whose corresponding wavelengths are $L_{p-b} = 103 \text{ m}$, $L_{p-c} = 99.5 \text{ m}$ and $L_{p-d} = 85.5 \text{ m}$; subscripts $b\text{--}d$ refer to the SAR spectra from figure 9(b–d)), which decrease away from the shore (L_p increases) and thus could not be associated with the incoming ocean swell. Based on its wavelength range and increase with distance, we believe that these SAR image intensity peaks could be associated with the fetch-limited wind-sea waves generated by the *Tehuano* winds. These results deserved, nonetheless, further investigation.

4.2 Comparison to parametric relations

In order to examine whether or not the intensity peaks detected on the image spectra shown in figures 9(b)–(d) could correspond to the growing wind-sea waves, our results were contrasted with the parametric wave-prediction relations proposed by Kahma and Calkoen (1992). Figure 10 shows a plot of peak period T_p as a function of fetch X for the case of stable stratification that, according to García-Nava *et al.* (2009), dominate during *Tehuano* events. Curves of wave growth are plotted for wind-speed values $U_{10} = 5\text{--}30 \text{ m s}^{-1}$ every 5 m s^{-1} .

Asterisks indicate the peak periods $T_p = 8.1$, 7.9 and 7.4 s derived, respectively, from the wavelengths $L_{p-(b-d)}$ described above through the deep-water dispersion relation. The associated fetches $X_{b-d} = 122.6$, 91.8 and 57.8 km represent the distances measured from the shore to the centre of the red squares in figure 9(a), closely following the direction of the wind. For comparison, triangles correspond to peak period values calculated directly through Kahma and Calkoen's (1992) relations at fetches X_{b-d} with collocated wind-speed values $U_{10-b-d} = 15.4$, 16.03 and 17.9 ms^{-1} , obtained from the blended QuikSCAT data. Note that predicted values $T_{p-b}' = 6.8 \text{ s}$, $T_{p-c}' = 6 \text{ s}$, $T_{p-d}' = 5.3 \text{ s}$ are about 15–30% lower than those derived from the TerraSAR-X images. Corresponding predicted wavelengths, $L_{p-b-d}' = 73.8 \text{ m}$, 57.3 m and 44.1 m are thus shorter than measured L_{p-b-d} values. Table 3 summarizes these values.

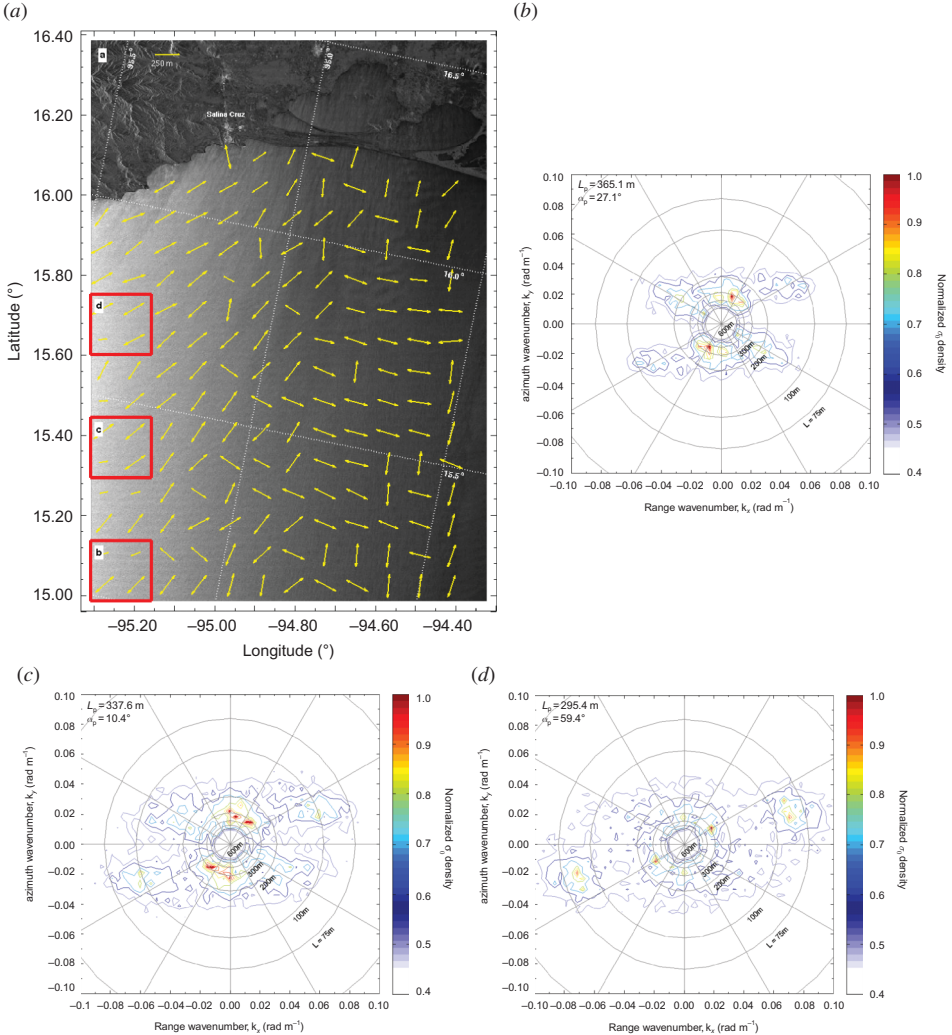


Figure 9. Similar to figure 8, ocean-wave conditions derived from the SC scene acquired on 21 March 2008. (a) Estimated SAR-image peak wavelength L_p in yellow; two-head arrows represent wave propagation direction with 180° ambiguity. Meridians and Parallels shown as dashed lines; bathymetric contours above 40 m of water depth shown as solid white lines. (b)–(d) two-dimensional SAR image intensity spectra calculated from the three ca. 17×17 km subimages shown as red squares on (a); (d) is closer to the shore. Horizontal and vertical axes are range and azimuth wavenumbers, k_x and k_y respectively, in rad m $^{-1}$.

One of the several possible reasons for the differences between SAR-derived and parametric-predicted wave parameters is the fact that the wave-growth relations have been postulated for a straight shoreline perpendicular to the wind direction. This is not the case at Tehuantepec where the wind-jet axis is oblique with respect to the shore and rotates during the evolution of the *Tehuano* event. Other reasons, as underlined by Kahma and Calkoen (1992), include gustiness and variations of surface roughness and air/sea temperature. Although we are inclined to consider that deviations from

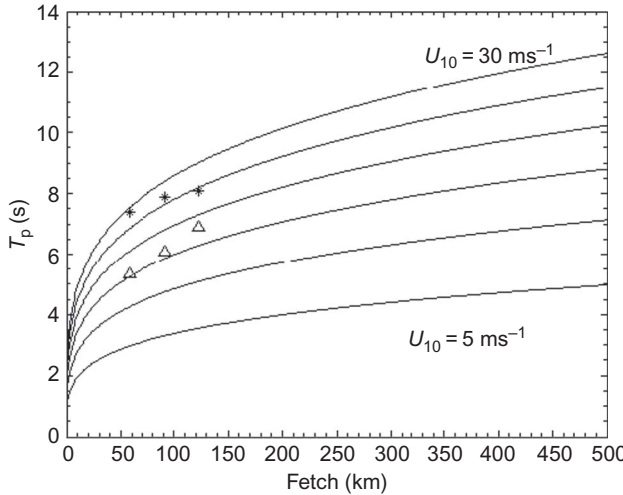


Figure 10. Fetch-limited wave growth derived from parametric prediction relations proposed by Kahma and Calkoen (1992) for the case of stable stratification: peak period T_p as a function of fetch. Solid curves correspond to wind speed $U_{10} = 5\text{--}30 \text{ ms}^{-1}$ every 5 ms^{-1} . Asterisks correspond to the three cases derived from the SAR image intensity spectra; for comparison, triangles correspond to values calculated through these parametric relations for the appropriate fetch and wind speed.

Table 3. Comparison of SAR-derived wave parameters, parameters estimated through the relations of Kahma and Calkoen (1992) and the collocated DWD data. Subscripts $b\text{--}d$ refer to the SAR spectra from figures 9(b)–(d); fetch X was directly estimated from the images; wind speed U_{10} was retrieved from the blended QuikSCAT wind product.

X (km)	U_{10} (ms^{-1})	SAR-derived		Parametric relations			DWD data	
		L_p (m)	T_p (s)	L_p' (m)	T_p' (s)	H_s' (m)	H_s (m)	α_p ($^\circ$)
b	122.6	15.4	103.0	8.1	73.8	6.8	3.0	4.9
c	91.8	16.0	99.5	7.9	57.3	6.0	2.3	4.6
d	57.8	17.9	85.5	7.4	44.1	5.3	1.8	3.9

parametric relations may be due to the modulation of the growing wind-sea by the incoming ocean swell, as suggested by García-Nava *et al.* (2009), our research still awaits the evidence to adequately support such a hypothesis.

4.3 Linearity analysis

Another explanation for these discrepancies may arguably be that the formation of the SAR image is highly nonlinear, and thus a wave-inversion scheme is required to properly derive wave parameters. In order to further explore this idea, we have compiled wind and wave model data from the vicinity of the SAR wave-retrieval results of figures 9(b)–(d) and plotted them on a linearity boundary graph following Alpers *et al.* (1981, figure 8). A condition that has to be fulfilled for azimuth travelling waves to be imaged linearly, i.e. to have a constructive velocity bunching MTF R^{bunch} , is

$$\left| \frac{R}{V} \frac{\partial u_r}{\partial x} \right| \ll 1. \quad (9)$$

Equation (9) may be expressed in terms of ocean-swell and satellite parameters by

$$\left| \frac{R}{V} \frac{\partial u_r}{\partial x} \right| \leq \frac{R}{V} \frac{H}{2} |\mathbf{k}| \omega_k G \cos \Phi \equiv C, \quad (10)$$

where H is the wave height or twice the wave amplitude, $|\mathbf{k}|$ is the modulus of the wavenumber vector, Φ is the angle between the platform flight direction and the wave propagation direction α_p and

$$G(\Phi, \theta) = \sqrt{\sin^2 \theta \sin^2 \Phi + \cos^2 \theta} \quad (11)$$

is called the geometric parameter. $|C| = 0.3$ is mentioned to be a reasonable choice for the linearity limit, where the mapping turns from linear (below each corresponding curve in figure 11) to nonlinear (above).

According to the DWD data for the Gulf of Tehuantepec on 21 March 2008 at 00h UTC, H_s values from both sea and swell are of the same order of magnitude: mean $H_{s-sea} = 2.6$ m and mean $H_{s-swell} = 3.7$ m. These values span $H_{s-swell} = 0.5$ –5.3 m and $H_{s-sea} = 0.2$ –5.1 m, respectively. Model H_s values interpolated and collocated to the image intensity spectra of figures 9(b)–(d) (DWD grid points were located 10 to 15 km away from the centres of the sub-images) were $H_{s-sea-b-d} = 4.9, 4.6$ and 3.9 m, respectively. Hence, propagation direction values relative to north varied from $\alpha_{b-d} = 255$ to 254.6 and 254° , respectively. Satellite parameters used in equation (11) to construct figure 11 are $V_{TSX} = 7.6$ km s $^{-1}$, $\theta_{TSX} = 25^\circ$, heading = 348.6° (ascending path), platform height $h_{plat} = 514.8$ km and $R_{TSX} = h_{plat} / \cos \theta_{TSX}$ for TerraSAR-X. For comparison, linearity boundaries for the Advanced Synthetic Aperture Radar (ASAR) carried onboard ENVISAT have also been derived. ENVISAT's parameters are: $V_{ENV} = 7.55$ km s $^{-1}$, $\theta_{ENV} = 22^\circ$, heading = 347.9° , platform height $h_{plat} = 800$ km and $R_{ENV} = h_{plat} / \cos \theta_{ENV}$.

It is not surprising to observe in figure 11 that TerraSAR-X linearity boundaries (thick solid and dashed lines) allow for a relatively larger linear regime than ENVISAT (thin lines). It is worth noting that curves corresponding to the case where $\Phi \neq 0$ for both platforms have a relatively higher slope due to the fact that the wind-sea waves generated by the *Tehuano* propagate are almost perpendicular to the azimuth direction. While asterisks represent the location of waves with wavelengths L_p derived from the SAR image analyses and significant wave height H_s interpolated from the DWD wave-model data, triangles represent predicted wave parameters L_{p-b-d}' and H_{s-b-d}' estimated through the parametric relations of Kahma and Calkoen (1992) (see §4.2).

The latter cases are located in the nonlinear regime; contrastingly, squares found on TerraSAR-X's linear regime represent the case of L_p derived from the SAR analysis and the corresponding predicted parametric H_{s-b-d}' , which, as noted in table 3, are almost half the model H_s values. Steeper waves are thus likely to lie in the nonlinear regime and hence, are not correctly imaged by the SAR.

Since two out of three cases lie on the nonlinear regime close to the boundary, it is arguable whether or not an inversion scheme should be applied to properly derive fetch-limited wave parameters under such strong wind cases. Though not presented here, similar results obtained for the swell waves from the DWD data provided additional evidence to suggest that a wave-inversion scheme is desirable.

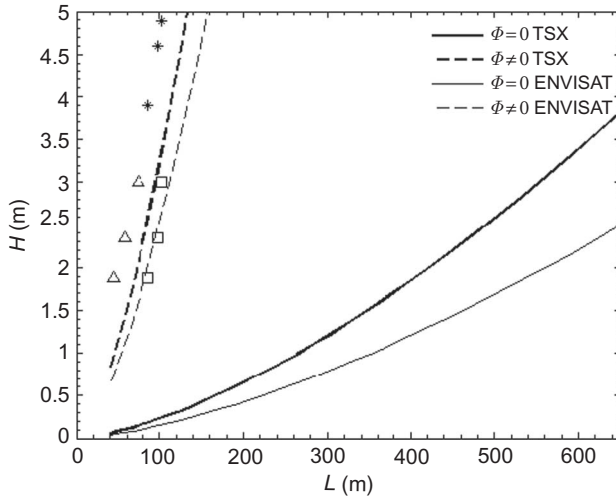


Figure 11. Regions where the velocity bunching modulation transfer function, R^{bunch} , changes from linear to nonlinear (below and above the curves, respectively; after Alpers *et al.* (1981)). Thick lines are for the TerraSAR-X platform with an incidence angle $\theta = 25^\circ$; thin lines are for the ENVISAT satellite with an incidence angle $\theta = 22^\circ$. Solid lines represent the case of waves propagating parallel to the satellite flight direction, $\Phi = 0$; dashed lines are for waves travelling at an angle, $\Phi \neq 0$, with respect to the satellite track. Asterisks represent a case with L_p derived from the SAR analyses and H_s interpolated from DWD wave-model data; triangles are for a case where L_p' and H_s' were estimated through the parametric relations of Kahma and Calkoen (1992); squares are for the composite of L_p derived from SAR data and H_s' calculated from the parametric relations.

5. Conclusions

The results shown and discussed in this paper are examples of the great potential that high-resolution TerraSAR-X images have for revealing the detailed spatial evolution of the ocean surface. Synoptic wind and wave conditions at the Gulf of Tehuantepec and the adjacent Pacific Ocean during a strong *Tehuano* event were estimated from a 30×50 km SM scene, as well as from a larger 100×150 km SC scene acquired on 20 and 21 March and 2008 at 12:19h and 00:19h UTC, respectively. Wind retrieval based on the X-MOD algorithm reported a fan-shaped distribution of the wind with the wind-jet axis rotating over time. Although average wind-speed values derived from the X-band SAR were in reasonable agreement with model data, maxima values were underestimated. Similarly, inferred wave information was consistent with model results and provided evidence of the spatial evolution of shoaling and refracting waves in the nearshore. This is in support of the idea of Li *et al.* (2009) that high-resolution TerraSAR-X imagery is a particularly good tool to observe the spatial variability of coastal ocean-wave behaviour.

Additional analysis on the spatial evolution of SAR image intensity spectral peaks located 60–120 km away from the coast in the downwind direction suggest the presence of wave energy propagating to the west–southwest, closely aligned with the offshore blowing winds. Comparison of the corresponding wavelengths to parametric wave-prediction relations proposed by Kahma and Calkoen (1992) showed that the secondary peak values derived from the SAR analyses are larger than

predicted. Since a number of relevant explanations for these deviations have risen, further analyses are required, and will be conducted in the near future. A small exercise following Alpers *et al.* (1981) demonstrated that two out of three cases of steep fetch-limited waves generated by the strong gap winds at the Gulf of Tehuantepec lie within the nonlinear regime of the SAR image formation, but close to its limit when the reasonable value of $C = 0.3$ was established. Based on these results, we suggest that a wave-inversion scheme, similar to the ones long proposed for the C-band SAR carried out on European satellites and extensively validated, is desirable to properly derive true wave parameters from TerraSAR-X imagery.

Acknowledgements

This study was developed as part of an academic stay at the Remote Sensing Institute, DLR, under the supervision of Dr S. Lehner. Our profound gratitude to the people in IMF-DLR who contributed to the success of this work: Dr T. König, Y. Ren, P. Held and T. Hantl. Special thanks to Dr P. Osuna from DPO-CICESE and Dr W. Rosenthal from GAUSS mbH for their revisions and comments to the manuscript. We gratefully acknowledge T. Bruns from DWD for providing access to the Global Wind and Wave data. This study was possible thanks to support from the Mexican Government (*Programa de Becas-Mixtas*, CONACYT; DirocIOA project 62520), UABC (*Departamento de Cooperación Internacional e Intercambio Académico*) and DLR (project *Synergy of ocean remote sensing information in oceanic and coastal waters: direct applications from DLR receiving antenna station in Chetumal, QR, Mexico*). Access to TerraSAR-X was possible through project OC-0506 *Study of ocean wave-spectrum evolution under gap-wind and hurricane conditions on Mexican coastal waters using high resolution TerraSAR-X imagery*.

References

- ALPERS, W., ROSS, D. and RUFENACH, C., 1981, On the detectability of ocean surface waves by real and synthetic aperture radar. *Journal of Geophysical Research*, **86**, pp. 6481–6498.
- ÁLVAREZ, L., BADÁN-DANGÓN, A. and VALLE, A., 1989, On coastal currents off Tehuantepec. *Estuarine, Coastal and Shelf Science*, **29**, pp. 89–96.
- ARDHUIN, F. and JENKINS, A., 2005, On the effect of wind and turbulence on ocean swell. *Proceedings of The Fifteenth (2005) International Offshore and Polar Engineering Conference*. Seoul, Korea, June 19–24, 2005, pp. 429–434.
- ARDHUIN, F. and JENKINS, A., 2006, On the interaction of surface waves and upper ocean turbulence. *Journal of Physical Oceanography*, **36**, pp. 551–557.
- ARDHUIN, F., O'REILLY, W., HERBERS, T. and JESSEN, P., 2003, Swell transformation across the continental shelf - part I: attenuation and directional broadening. *Journal of Physical Oceanography*, **33**, pp. 1921–1939.
- ARDHUIN, F., HERBERS, T., VAN VLEDDER, G.P.H., WATTS, K.P., JENSEN, R. and GRABER, H., 2007, Swell and slanting fetch effects on wind wave growth. *Journal of Physical Oceanography*, **37**, pp. 908–931.
- BEAL, R., TILLEY, D. and MONALDO, F., 1983, Large- and small-scale spatial evolution of digitally processed ocean wave spectra from SEASAT SAR. *Journal of Geophysical Research*, **88**, pp. 1761–1778.
- BEAL, R., GERLING, T., IRVINE, D., MONALDO, F. and TILLEY, D., 1986, Spatial variations of ocean wave directional spectra from the SEASAT SAR. *Journal of Geophysical Research*, **91**, pp. 2433–2449.

- BRUSCH, S., LEHNER, S., FRITZ, T., SOCCORSI, M., SOLOVIEN, A., and VAN SCHIE, B., 2010, Ship surveillance with TerraSAR-X. *IEEE Transactions in Geoscience and Remote Sensing*, in print.
- BRUSCH, S., LEHNER, S. and SCHULZ-STELLENFLETH, J., 2008, Synergetic use of radar and optical satellite images to support severe storm prediction for offshore wind farming. *Journal of Selected Topics in Applied Earth Observations and Remote Sensing*, **1**, pp. 57–66.
- CENTER FOR SATELLITE EXPLOITATION AND RESEARCH (CERSAT), 2002, *QuikSCAT Scatterometer Mean Wind Field Products - User Manual*. Version 1.0., Document C2-MUT-W-03-IF. IFREMER, February 2002.
- CHELTON, D., FREILICH, M. and ESBENSEN, S., 2000, Satellite observations of the wind jets off the Pacific Coast of Central America - part I: case studies and statistical characteristics. *Monthly Weather Review*, **128**, pp. 1993–2018.
- COLLARD, F., ARDHUIN, F. and CHAPRON, B., 2005, Extraction of coastal ocean wave fields from SAR images. *Journal of Oceanic Engineering*, **30**, pp. 526–533.
- COLLARD, F., MOUCHE, A., CHAPRON, B., DANILLO, C. and JOHANNESSEN, J., 2008, Routine high resolution observation of selected major surface currents from space. In *Proceedings of SeaSAR 2008*, 21–25 January 2008, Frascati, Italy (ESA SP-656).
- DÍAZ MÉNDEZ, G., OCAMPO-TORRES, F.J., OSUNA, P., GARCÍA, H. and DURAZO, R., 2008, Effects of gap-winds on multi-modal ocean swell systems at the south Pacific Coast of Mexico. In *Proceedings of SeaSAR 2008*, 21–25 January 2008, Frascati, Italy (ESA SP-656).
- DONELAN, M.A. and PIERSON JR., W.J., 1987, Radar scattering and equilibrium ranges in wind-generated waves with application to scatterometry. *Journal of Geophysical Research*, **92**, pp. 4971–5029.
- ENGEN, G. and JOHNSEN, H., 1995, SAR ocean wave inversion using image cross spectra. *IEEE Transactions in Geoscience and Remote Sensing*, **33**, pp. 1047–1056.
- FRITZ, T. and EINEDER, M., 2008, *TerraSAR-X Ground Segment Basic Product Specification Document*. Cluster Applied Remote Sensing, DLR. Document TX-GS-DD-3302, issue 1.5.
- GARCÍA-NAVA, H., OCAMPO-TORRES, F.J., OSUNA, P. and DONELAN, M.A., 2009, Wind stress in the presence of swell under moderate to strong wind conditions. *Journal of Geophysical Research*, **114**, C12008.
- HASAGER, C.B., ASTRUP, P., NIELSEN, M., CHRISTIANSEN, M.B., BADGER, J., NIELSEN, P., SØRENSEN, P.B., BARTHELME, R.J., PRYOR, S.C. and BERGSTRÖM, H., 2007, *SAT-WIND Project – Final Report*. Risø-R-1586, Risø National Laboratory, Technical University of Denmark.
- HASSELMANN, K. and HASSELMANN, S., 1991, On the non-linear mapping of an ocean wave spectrum into a Synthetic Aperture Radar image spectrum and its inversion. *Journal of Geophysical Research*, **96**, pp. 10 713–10 729.
- HASSELMANN, S., HEIMBACH, P. and BENNEFELD, C., 1998, *The WASAR Algorithm for Retrieving Ocean Wave Spectra from SAR Image Spectra*. Technical Report 14, Deutsches Klimarechenzentrum.
- HASSELMANN, S., BRÜNING, C., HASSELMANN, K. and HEIMBACH, P., 1996, An improved algorithm for the retrieval of ocean wave spectra from synthetic aperture radar image spectra. *Journal of Geophysical Research*, **101**, pp. 16 615–16 629.
- HERSBACH, H., STOFFELEN, A. and DE HAAN, A., 2005, *CMOD5: an Improved Geophysical Model Function for ERS C-band Scatterometry*. ECMWF Internal Report no. 395.
- HORSTMANN, J., LEHNER, S., KOCH, W. and TONBOE, R., 2000, Computation of wind vectors over the ocean using spaceborne Synthetic Aperture Radar. *John Hopkins APL Technical Digest*, **21**, pp. 100–107.
- HORSTMANN, J., KOCH, W., THOMPSON, D.R. and GRABER, H., 2006, Observation of hurricane winds using Synthetic Aperture Radar. In *Proceedings of SeaSAR 2006*, 23–26 January 2006, Frascati, Italy (ESA SP-613).
- HWANG, W., JOHANNESSEN, J., ALPERS, W., YANG, J. and GAN, J., 2008, Spatial and temporal variations of internal wave sea surface signatures in the northern South China Sea

- studied by spaceborne SAR imagery. In *Proceedings of SeaSAR 2008*, 21–25 January 2008, Frascati, Italy (ESA SP-656).
- IRVINE, D. and TILLEY, D., 1988, Ocean wave directional spectra and wave-current interaction in the Agulhas from the shuttle imaging radar-B synthetic aperture radar. *Journal of Geophysical Research*, **93**, pp. 15 389–15 401.
- JOHANNESSEN, J., SHUCHMAN, R., LYZENGA, D., WACKERMAN, C., JOHANNESSEN, O. and VACHON, P., 1996, Coastal ocean fronts and eddies imaged with ERS-1 synthetic aperture radar. *Journal of Geophysical Research*, **101**, pp. 6651–6667.
- KAHMA, K. and CALKOEN, C., 1992, Reconciling discrepancies in the observed growth of wind-generated waves. *Journal of Physical Oceanography*, **22**, pp. 1389–1405.
- KATSAROS, K., VACHON, P., LIU, T. and BLACK, P., 2002, Microwave remote sensing of tropical cyclones from space. *Journal of Oceanography*, **58**, pp. 137–151.
- KROGSTAD, H.E., SAMSET, O. and VACHON, P.W., 1994, Generalizations of the non-linear ocean–SAR transform and a simplified SAR inversion algorithm. *Atmosphere – Oceans*, **32**, pp. 61–82.
- LI, X., LEHNER, S. and HE, M., 2008, Ocean wave measurements based on satellite synthetic aperture radar (SAR) and numerical wave model (WAM) data - extreme sea state and cross sea analysis. *International Journal of Remote Sensing*, **29**, pp. 6403–6416.
- LI, X., LEHNER, S. and ROSENTHAL, W., 2009, Investigation of ocean surface wave refraction using TerraSAR-X data. *Transactions in Geoscience and Remote Sensing*, **48**, pp. 830–840.
- MASTENBROEK, C. and DE VALK, C.F., 2000, A semiparametric algorithm to retrieve ocean wave spectra from synthetic aperture radar. *Journal of Geophysical Research*, **105**, pp. 3497–3516.
- MASUKO, H., OKAMOTO, K., SHIMADA, M. and NIWA, S., 1986, Measurement of microwave backscattering signatures of the ocean surface using X-band and Ka-band airborne scatterometers. *Journal of Geophysical Research*, **91**, pp. 13 065–13 084.
- OCAMPO-TORRES, F., 2001, On the homogeneity of the wave field in coastal regions as determined from ERS-2 and RADARSAT SAR images of the ocean surface. *Scientia Marina*, **65**, pp. 215–228.
- OCAMPO-TORRES, F. and VACHON, P., 2000, Spatial variations of ocean wave spectra in coastal regions from RADARSAT and ERS synthetic aperture radar images. In *Proceedings 6th International Conference on Remote Sensing for Marine and Coastal Environments*, Charleston, SC. EEUU.
- OCAMPO-TORRES, F.J., DÍAZ MÉNDEZ, G., GARCÍA, H. and DURAZO, R., 2007, Ocean-swell spectrum evolution in the Gulf of Tehuantepec, Mexico. In *Proceedings of ENVISAT Symposium 2007*, 23–27 April 2007, Montreux, Switzerland (ESA SP-636).
- OUCHI, K., 1994, Modulation of waveheight spectrum and radar cross section by varying surface currents. *IEEE Transactions on Geoscience and Remote Sensing*, **32**, pp. 995–1003.
- REPPUCCI, A., LEHNER, S., SCHULZ-STELLENFLETH, J. and YANG, C., 2008, Extreme wind conditions observed by satellite synthetic aperture radar in the North West Pacific. *International Journal of Remote Sensing*, **29**, pp. 6129–6144.
- SCHULZ-STELLENFLETH, J. and LEHNER, S., 2004, Measurement of 2-D Sea Surface Elevation Fields using complex synthetic aperture radar data. *IEEE Transactions in Geoscience and Remote Sensing*, **46**, pp. 1149–1160.
- SCHULZ-STELLENFLETH, J., LEHNER, S. and HOJA, D., 2005, A parametric scheme for the retrieval of two-dimensional ocean wave spectra from synthetic aperture radar look cross spectra. *Journal of Geophysical Research*, **110**, p. C05004.
- SNODGRASS, F.E., GROVES, G.W., HASSELMANN, K., MILLER, G.R., MUNK, W.H., and POWERS, W.H., 1996, Propagation of ocean swell across the Pacific, *Proceeding of the Royal Society of London*, **A249**, pp. 431–497.

- STOFFELEN, A. and ANDERSON, D., 1997, Ambiguity removal and assimilation of scatterometer data, *Quarterly Journal of the Royal Meteorological Society*, **123**, pp. 491–518.
- VACHON, P.W. and DOBSON, F.W., 1996, Validation of wind vector retrieval from ERS-1 SAR images over the ocean. *The Global Atmosphere and Ocean System*, **5**, pp. 177–187.
- VESECKY, J. and STEWART, R., 1982, The observation of ocean surface phenomena using imagery from the Seasat synthetic aperture radar: an assessment. *Journal of Geophysical Research*, **87**, pp. 3397–3430.
- VIOLANTE-CARVALHO, N., OCAMPO-TORRES, F.J. and ROBINSON, I.S., 2004, Buoy observations of the influence of swell on wind waves in the open ocean, *Applied Ocean Research*, **26**, pp. 49–60.
- WAMDI GROUP: HASSELMAN, K., HASSELMAN, S., JANSSEN, P.A.E.M., KOMEN, G.J., BERTOTTI, L., LIONELLO, P., GUILLAUME, A., CARDONE, V.C., GREENWOOD, J.A., REISTAD, M., ZAMBRESKY, L. and EWING, J.A., 1988, The WAM model –a third generation ocean wave prediction model. *Journal of Physical Oceanography*, **18**, pp. 1775–1810.

**III. ANÁLISIS DE LA VARIABILIDAD DEL OLEAJE LIBRE
BAJO CONDICIONES DE VIENTO MODERADO EN EL GOLFO DE
TEHUANTEPEC UTILIZANDO RADAR DE APERTURA SINTÉTICA**

Artículo en revisión

Resumen

Se ha realizado un estudio para estimar la variabilidad espacial del campo de oleaje durante el proyecto "Análisis del intercambio entre el océano y la atmósfera en el Golfo de Tehuantepec (INTOA)" a través del análisis de imágenes de radar de apertura sintética (SAR) de la superficie del mar. Durante el INTOA se midieron las condiciones de viento y oleaje en el Golfo de Tehuantepec, México, del 22 de febrero al 4 de abril de 2005 utilizando diferentes instrumentos. De particular interés son los resultados correspondientes a cuando menos ocho eventos *Tehuanos* –vientos de chorro, de intensidad moderada a fuerte, que soplan de tierra hacia el mar con duración de 14 a 70 horas– característicos del área de estudio. Se calcularon espectros direccionales de oleaje $S(k,\alpha)$ a partir de tres juegos de cuatro imágenes complejas tipo mono-vista (SLC del inglés *single-look complex*) adquiridas por el SAR del satélite europeo ENVISAT sobre el Golfo de Tehuantepec los días 26 de febrero, 2 y 18 de marzo de 2005, coincidiendo con la etapa final de tres

eventos *Tehuanos*. A través del análisis de estos espectros se observó que el SAR tiene la capacidad de detectar campos de oleaje complejos, con sistemas múltiples de oleaje libre, en el área de estudio en condiciones de mar débil, con valores máximos de pendiente significantes $s = 0.008$. Se encontró que el campo de oleaje calculado con SAR no es homogéneo en un área de 100 por 100 km, como se ha supuesto en otros estudios; por el contrario, varía significativamente a escala de decenas de kilómetros. Se analiza la variabilidad espacial de la longitud de onda del oleaje lejano, del orden de 7–17%, a lo largo de su dirección de propagación con el fin de determinar la ubicación geográfica de las tormentas que le generaron, así como el instante de generación t_0 correspondiente.

Synthetic Aperture Radar analysis of ocean-swell variability at the Gulf of Tehuantepec under moderate off-shore winds.

G. M. Díaz Méndez¹, F. J. Ocampo-Torres² and B. Chapron³

¹ Facultad de Ciencias Marinas, Universidad Autónoma de Baja California (UABC). Km 103 carretera Tijuana-Ensenada, Ensenada, Baja California. 22880. Mexico. diaz.guillermo@uabc.edu.mx

² Departamento de Oceanografía Física, Centro de Investigación Científica y Educación Superior de Ensenada (CICESE). Km 107 carretera Tijuana-Ensenada, Ensenada, Baja California. 22860. Mexico. ocampo@cicese.mx

³ Laboratoire d'Océanographie Spatiale, Centre de Brest, Institut Française de Recherche pour l'Exploitation de la Mer (IFREMER). 13 Rue du Chatellier, F-29280 Plouzané. 29280. France. Bertrand.Chapron@ifremer.fr

Abstract

Research has been carried out to study the spatial variability of the wave field during the Gulf of Tehuantepec Air-Sea Interaction (INTOA) experiment through the analysis of synthetic aperture radar (SAR) images of the ocean surface. During INTOA, wind and wave conditions were recorded at the Gulf of Tehuantepec, Mexico, using different measuring techniques from 22 February to 4 April 2005. Particularly interesting are results corresponding to at least eight *Tehuanos*, moderate to strong gap-wind events blowing off-shore with persistence of 14–70 hours, characteristic of the study area.

Ocean-swell directional spectra $S(k, \alpha)$ were derived from three sets of four adjacent single-look complex (SLC) images acquired by the advanced synthetic aperture radar (ASAR) onboard the European Environmental Satellite (ENVISAT) over the Gulf at the final stage of three different *Tehuano* events, on 26 February, 2 and 18 March 2005. Through the analysis of these spectra it was observed that the SAR is capable of detecting complex, multi-peaked wave fields at the study area during low sea-state conditions, with maximum significant slopes $s = 0.008$. We found that the SAR-derived wave field is not homogeneous in an ocean surface of 100 km by 100 km, as assumed in previous studies; rather, it varies significantly in scales as small as tens of kilometers. Along-path wavelength variability, in the order of 7–17%, is analyzed to investigate the swells' time of generation t_0 and the location of the corresponding source storms.

1. Introduction

A large amount of research efforts have been addressed/directed to advance our understanding of ocean-atmosphere interaction and selected the Gulf of Tehuantepec, located at the south Pacific coast of Mexico, as their study area. Given its unique characteristics, led by the occurrence of strong gap-winds locally known as *Tehuanos* or *Nortes*, it has been long regarded as a natural laboratory, ideal to study many physical-, biological- and/or chemical-oceanography processes induced by or associated to these off-shore blowing jets of wind [see *Brandhorst*, 1958; *Roden*, 1961; and *Blackburn*, 1962 as examples]. One such effort was the *INTOA* experiment [*Ocampo-Torres et al.*, 2011], conducted from 22 February to 4 April 2005 with the main objective of

determining the effect of surface waves on the momentum flux of the ocean-atmosphere interface, as well as its dependence on environmental conditions. During INTOA, several types of recording devices were set to acquire in situ and remotely sensed information on the wave-field conditions, including three acoustic Doppler current profilers (ADCP; Nortek-Aquadopp), a highly instrumented air-sea interaction spar (ASIS) buoy [Graber, *et al.*, 2000], two phase-arrayed high-frequency (HF) radar stations and a series of synthetic aperture radar (SAR) images acquired by the European environmental satellite ENVISAT. The main idea being to simultaneously and complementary assess the temporal and spatial evolution of the wave spectrum during the strong off-shore wind events.

As opposed to the Eulerian perspective of recording the time evolution of a small area of the ocean-surface, remote sensing techniques, such as the SAR, bring the possibility of studying the quasi-instantaneous spatial distribution of ocean waves over tens to thousands of square meters of sea surface. For instance, Monaldo [1991] studied the spatial evolution of the wave field through the analyses of ERS-1 SAR imagery. He found that variations in wavenumber k and propagation direction α could represent either the variability of ocean parameters or the instability of the SAR image formation mechanisms. Analysis of the spatial evolution of SAR derived 2D spectra allowed Holt *et al.* [1998] to calculate the position of storm-generated swell. In their study, they assumed that the wave field was homogeneous throughout a single 100 by 100 km SAR Precision image. Later, Violante-Carvalho *et al.* [2010] made the same assumption (homogeneity of the wave field on a 100 by 100 km ERS-1 and -2 SAR Precision

Image) in order to study the effects of the wind-field on the waves. They proposed that detected variability of k and α should be due to inhomogeneity of the wind field near the coast. In our work, we followed a different approach and assumed that the wave field is homogeneous only at spatial scales in the order of a few tens of swell wavelengths (approximately 2.5 to 6 km).

The present paper is based on the analysis of three sets of four contiguous ENVISAT ASAR SLC images acquired over the Gulf of Tehuantepec and adjacent Pacific Ocean during the INTOA experiment. Our main objective has been to investigate the evolution of the SAR-derived spectrum $S(k, \alpha)$ and determine the spatial variability of the ocean-swell under moderate to strong, opposing wind conditions. In this work, we've attempted to relate the spatial distribution of 2D swell spectrum derived from SAR observations to the 2D spectrum evolution derived from in situ measurements.

This paper is organized in six sections including the Introduction. Section 2 presents an overview of the wind conditions prevailing at the study area during the times of acquisition of the SAR images analyzed in this work. In section 3, the methodology followed to estimate the characteristics of the wave field from these images is described. Next, results from the analysis of the SAR-inverted wave-spectrum evolution are presented. This is followed by a discussion on the spatial variability of the ocean-swell systems described in the preceding section. The last section includes a comparison of the SAR-derived wave field with time series of wave parameters recorded in situ during the INTOA campaign. It is shown that the along-path variability of a SAR-derived wave system may be used to approach its time of generation and the location of its generating

storm. An example is discussed where these results agree reasonably well with the location of source-storms derived from in situ measurements.

2. Synoptic wind conditions

At least eight *Tehuano* gap-wind events are documented to have occurred at the Gulf of Tehuantepec during the INTOA experiment, when the strongest reached wind-speed values just above 18 ms^{-1} and persisted for more than 24 hours. As shown in figure 1, the three sets of SLC images were acquired during the final stages of one moderate and two strong *Tehuano* events. While maximum wind speeds U_{10} recorded with a sonic anemometer mounted on the ASIS buoy were approximately 11 ms^{-1} , 16 ms^{-1} and 16 ms^{-1} , respectively, U_{10} collocated with the SAR acquisition times $t_{\text{SAR_1}}$, $t_{\text{SAR_2}}$, and $t_{\text{SAR_3}}$, were about 5 ms^{-1} , 5 ms^{-1} and 8 ms^{-1} .

Synoptic wind conditions at the Gulf of Tehuantepec and adjacent Pacific have been derived from the QuikSCAT scatterometer wind-speed estimates blended into a global grid [CERSAT, 2002] with a spatial resolution of 0.25° by 0.25° and a temporal resolution of six hours. Even though results from this blended QuikSCAT wind product are rather underestimated in comparison to the ASIS buoy's U_{10} records (particularly during the peaks of the *Tehuanos*), they provide a good insight of the wind-field conditions a few hours before or after the times of acquisition of the SAR images.

2.1. 26 February 2005

Figure 2a shows a map of the study area with results from the blended QuikSCAT data for 26 February 2005 at 06 h UTC, about 1.5 hours after t_{SAR_1} . Background color corresponds to wind speed in ms^{-1} while arrows correspond to vectors of wind-speed and direction. Mooring location of the ASIS buoy, approximately 20 km south-east off Salina Cruz harbor, is represented by a black asterisk; the four dashed squares depict the area covered by the SAR images. As can be noted in the figure, trace of a *Tehuano* event can be observed only at the head of the Gulf, where wind speed was moderate and direction, $75\text{--}85^\circ$ clockwise from north (oceanographic convention). Further off-shore, U_{10} decreased towards the south and south-east. Overall wind speed averaged 3 ms^{-1} over the whole area, but reached just above 6.5 ms^{-1} close to the mooring of the ASIS buoy, where it recorded $U_{10} = 5.1 \text{ ms}^{-1}$ at 4:41 h UTC. It can be noted that higher wind speeds (5 ms^{-1}) occur to the east of the area covered by the two northern images while winds lower than 2.5 ms^{-1} dominate at the southern half of the southernmost scene.

2.2. 2 March 2005

Low winds ($U_{10} < 3 \text{ ms}^{-1}$) also dominated the study area 1.5 hours after t_{SAR_2} , at 18 h UTC on 2 March 2005. As can be seen on figure 2b, moderate winds occurred to the north, close to the ASIS buoy, where model results averaged 4.1 ms^{-1} ; contrastingly, a wind-speed value $U_{10} = 2.3 \text{ ms}^{-1}$ was registered in situ at 17:45 h UTC. At this location, wind direction varies significantly: winds blow on-shore closer to the coast and to the south-east further off-shore. South of latitude 15.5° N and east of longitude 95° W , the

latter direction persists. To the west, wind direction is ca. 100° clockwise from north; the wind is weaker, particularly south of 14° N, where it drops below $U_{10} = 2 \text{ ms}^{-1}$.

2.3. 18 March 2005

According to the ASIS buoy's records, the sixth *Tehuano* event registered during the INTOA experiment peaked at 1:30 h UTC, about 15 hours before t_{SAR_3} . Even though it finished around 19 h UTC, the wind field shown in figure 2c, corresponding to 18 March 2005 at 18 h UTC, still displays the typical distribution described by *Chelton et al.* [2000]: fan-shaped wind vectors at the head of the Gulf, and inertial effects, i.e., winds rotating towards the west, further off-shore. Overall conditions are of higher winds ($U_{10} > 5 \text{ ms}^{-1}$) at the head of the Gulf and along the wind jet axis, while lower ($U_{10} < 2 \text{ ms}^{-1}$) towards the south-east. Model values close to the ASIS average $U_{10} = 5.6 \text{ ms}^{-1}$, which agree well to those recorded by the buoy at 17:34 h, $U_{10} = 4.8 \text{ ms}^{-1}$.

3. Estimation of the wave field

A small number of ENVISAT ASAR images were acquired over the Gulf of Tehuantepec and adjacent Pacific Ocean during the INTOA experiment. This SAR collection includes three sets of four consecutive full-resolution image-mode SLC images, VV polarized, acquired on 26 February at 04:19–20 h UTC (ascending path), 2 March at 16:20–21 h UTC (descending path) and 18 March at 16:17–18 h UTC (also descending). This type of SAR images has a nominal resolution of 9 by 6 m and coverage of about 100 by 100 km. Each set of four consecutive images provides,

therefore, information on the characteristics of the ocean surface in an area of 100 km by 380 km long, approximately, since some along-path overlapping does exist. Figures 3a, 3b and 3c show composites of the SAR image dataset analyzed in this study and their location at the Gulf of Tehuantepec and adjacent Pacific Ocean. It is important to note the large regions of low backscatter, presumably due to low sea-surface roughness, present in the 26 February and 2 March sets. Location of these patches agrees reasonably well with the low wind-speed values ($U_{10} < 3 \text{ ms}^{-1}$) observed in figures 2a and 2b from the blended QuikSCAT product. Accurate derivation of the wave field from SAR depends, among other things, on the homogeneity of the radar backscatter signal associated to the sea-surface roughness with wavelength approximately equal to the radar wavelength λ_0 . Since the above mentioned low σ_0 patches induced additional variability during the estimation of wind and wave conditions, some were excluded from our analysis.

In order to study the quasi-instantaneous characteristics of the wave field at the times of acquisition, SAR images were divided into smaller subimages from which 2-D SAR image intensity spectra $S(\mathbf{k})$ were estimated through conventional Fourier techniques. Evolution of the swell spectrum was studied using full-resolution subimages of two different sizes: 512 by 512 pixels (12 by 12 km, approximately) and 256 by 256 pixels (6 by 6 km, approximately). Each SLC scene was thus divided into mosaics of 7 by 9 and 15 by 18 subimages, respectively. SAR-inverted directional ocean-swell spectra $S(k, \alpha)$ were then calculated from the latter following the procedure presented by *Collard et al.* [2005], which extends the application of the original algorithm of *Chapron et al.*

[2001] over a wider range of incidence angles, θ . A simple partition scheme was applied to multi-peaked spectra in order to identify individual wave systems and to evaluate their spatial evolution. Partition was accomplished by first integrating $S(k,\alpha)$ with respect to k ; then, from $S(\alpha)$, selecting all peaks above a certain threshold. Once individual propagation directions α_{p_n} (where n represents a given partition) were found, the 2D spectrum was queried for its corresponding wavenumber k_{p_n} and peak energy level E_{p_n} .

4. Evolution of the SAR-inverted wave spectrum

Inverted wave spectra $S(k,\alpha)$ successfully derived from the three sets of SLC scenes revealed that at least two well defined swell systems co-exist in the study area at all times, $t_{\text{SAR_1-3}}$. Even though single- or double-peaked cases are far more common, multi-peaked spectra were frequently observed. Figure 4 shows examples of wave spectra derived from two 256-by-256-pixel subimages of the 2 March 2005 set: a four-peaked spectrum observed at the south end of the SAR strip, about 400 km away from the coast (figure 4a), and a two peak spectrum approximately corresponding to the mooring location of the ASIS buoy, about 22 km off Salina Cruz harbor (figure 4b), where water depth was approximately 60 m. In figure 4a, three shorter and one longer (but less energetic) swell systems, $L_{p_1-3} \approx 250$ m and $L_{p_4} \approx 400$ m, respectively, are observed propagating towards the directional range $\alpha = 330^\circ\text{--}60^\circ$ clockwise from North. Contrastingly, the spectrum in figure 4b shows only two peaks: the longer $L_{p_4} = 300$ m and one of the shorter ones $L_{p_1} = 227$ m, presumably the most energetic. Corresponding propagation directions are $\alpha_{p_4} = 10^\circ$, and $\alpha_{p_1} = 355^\circ$, respectively. Loci of these peaks

are thus shifted on the spectral space (k, α) with respect to those in figure 4a, $L_{p_1} = 244$ m and $\alpha_{p_1} = 350^\circ$, and $L_{p_4} = 398$ m and $\alpha_{p_4} = 35^\circ$, respectively. This represents a wavelength reduction of approximately 7% and 25% (larger for longer waves) and a directional shift of +5° and -25°, respectively, in comparison to deep-water values from figure 4a.

A similar behavior (L_p decrease and shifting of α_p) is observed on spectra derived from near shore subimages, particularly those located in water depths under 100–200 m (see figure 5), in all sets of SAR images. Shortening and angular shifting of the latter are believed to be the result of shallow-water transformations, i.e. shoaling and refraction. Spectral evolution due to such shallow-water effects has been reported before. *Ocampo-Torres* [2001] evaluated refraction and diffraction near the Baja California coast from ERS-2 and RADARSAT images; *Collard et al.* [2005] reported a significant decrease in H_s due to the sheltering effect of islands, high shoals and headlands at the western English Channel through the analysis of ENVISAT ASAR images; and *Li et al.* [2010] observed crossed seas and evaluated strong diffraction in the lee of Terceira island from a TerraSAR-X StripMap scene. Nonetheless, the larger sea-surface covered by our contiguous set of images allowed us to study spatial variations of the several swell systems conforming the multi-peaked spectra detected.

5. Variability of the ocean-swell

In order to evaluate the spatial variability of the wave field, successfully derived spectra were analyzed to identify individual wave systems: after integration with respect

to k , identified peaks were considered only if their maximum energy rose above a value equal to 10% of the most energetic peak. A maximum of four individual systems, $n \leq 4$, were selected per spectrum. Figure 5 shows the spatial distribution of identified SAR-derived swell systems, corresponding to acquisition times $t_{\text{SAR_1-3}}$. Even though this analysis was performed on both sizes of subimages (256 by 256 and 512 by 512 pixels), examples shown correspond to the latter. Wavelength vectors ($L_{p_n} = 2\pi/k_{p_n}$, α_{p_n}) for swell systems $n = 1-4$ are represented by arrows, which are scaled relative to each other but not with respect to the map. Since very low σ_0 values dominate the southernmost SLC scene from the 26 February set (see figure 3a), figure 5a shows results from only three consecutive images. Single- and double-peaked spectra are far more common than multi-peaked cases. On the $t_{\text{SAR_1}}$ set (figure 5a), three-peaked spectra were found at the western half of the SAR strip, as well as south of latitude 15.25° , approximately. On the 2 March set ($t_{\text{SAR_2}}$, figure 5b), three-peaked spectra are found only at the near-range half of the SAR strip, south of latitude 14° N. Contrasting with the above, multi-peaked spectra dominate at the northern one-third of the 18 March 2005 SAR strip (figure 5c). While most of the identified swell systems propagate towards the head of the Gulf, a few cases were observed where wave energy propagated to the east and south-east ($t_{\text{SAR_1}}$ and $t_{\text{SAR_3}}$). Their signal, however, was never detected shoreward of latitude 15.25° . This is likely because the western end of the Gulf of Tehuantepec would play an obstructing role to swell waves generated at the north and western Pacific [Ocampo-Torres *et al.*, 2011].

Figures 6–8 include a set of maps derived from the previous analysis, where

wavelength vectors from individual wave systems $n = 1\text{--}4$ are shown. Identified systems were grouped according to their propagation direction, which was then used as a separation criterion. Hence, panels a) include waves propagating in the range $\alpha_{p_1} = 315^\circ\text{--}357.5^\circ$; b) in the range $\alpha_{p_2} = 357.6^\circ\text{--}30^\circ$ ($357.6^\circ\text{--}15^\circ$ for the t_{SAR_2} set); c), $\alpha_{p_3} = 30.1^\circ\text{--}90^\circ$ ($15.1^\circ\text{--}35^\circ$ for t_{SAR_2}); and d), $\alpha_{p_4} = 90.1^\circ\text{--}125^\circ$ ($35.1^\circ\text{--}70^\circ$ for t_{SAR_2}). Besides the scaled vectors, color has been included to easily distinguish wavelength variations. Figures 6a–d show the four different swell systems detected from the February 26 SAR images, with mean propagation directions $\alpha_{p_1} \approx 345^\circ$, $\alpha_{p_2} \approx 10^\circ$, $\alpha_{p_3} \approx 65^\circ$ and $\alpha_{p_4} \approx 110^\circ$, respectively. It may be noted that $n = 1$ is the dominant wave system, closely followed by $n = 4$ (431 & 313 observations respectively, out of 1087 total). Mean wavelength values are $L_{p_1} = 255$ m and $L_{p_4} = 260$ m, respectively. System $n = 2$, with an average $L_{p_2} = 245$ m, it is the shortest system of the set. Corresponding standard deviations are $L_{p_1_std} = 38$ m, $L_{p_2_std} = 42$ m and $L_{p_4_std} = 40$ m and thus, their variability (i.e. deviation from average) may be estimated as 15%, 17% and 15%, respectively. As may be observed in figure 6a, longer waves (warm colors) seem to dominate at the southern half of the SAR strip, south of latitude 15° N, while shorter waves (cold colors) occur near the coast, to the north-east of the strip. The shortest waves from $n = 1$ ($L_{p_1} \leq 150$ m) however, are associated to the low backscatter patches discussed in section 3 and are not included in the statistics. This behavior appears to be valid also for $n = 2$ (figure 6b), where shorter waves dominate the northern half of the strip, besides those associated to the low backscatter patches just mentioned. It would not be the case for system $n = 4$, which seem to have originated at the north-west Pacific.

Figure 7 shows results from the 2 March set of SAR images. In this case, system $n = 2$ includes the dominant waves (794 observations, out of 1377 total), while $n = 1$, the second largest group (343/1377). Corresponding mean wavelength and propagation directions are $L_{p_2} = 247$ m, $\alpha_{p_2} = 3^\circ$, $L_{p_1} = 244$ m and $\alpha_{p_1} = 348^\circ$, respectively. Estimated wavelength variability values for the above are 7% and 13%, respectively. It is interesting to note, on figure 7b, an abrupt decrease in wavelength close to the shore (colder colors), likely due to shallow water wave transformations (i.e., shoaling and refraction) discussed in section 4. Figures 7c and 7d show two additional wave systems: one with a α_p value closely matching system $n = 2$, but much longer ($L_{p_3} \geq 350$ m); and another, composed also of longer waves ($L_{p_4} \approx 400$ m) propagating to $\alpha_{p_4} = 48^\circ$. The southern right half of the SAR strip in figure 7c shows the spatial distribution of an additional system, the lower-energy peak from the three shorter ones shown on the inverted spectrum $S(k,\alpha)$ of figure 4a. Figure 8b includes the dominant system detected from the 18 March imagery. Swell systems $n = 1$ and 2 have similar wavelength values, $L_{p_1} = 287.9$ m and $L_{p_2} = 288.2$ m, respectively, but corresponding propagation directions $\alpha_{p_1} = 343^\circ$ and $\alpha_{p_2} = 16^\circ$. Wavelength standard deviations are $L_{p_1_std} \approx 16$ m and $L_{p_2_std} \approx 19$ m; estimated variability is therefore 5% and 6% from their means, respectively. It is quite interesting to observe, particularly on panel b), a gradual evolution of this system's wavelength along the approximately 350-km propagation path. Shorter waves at the south end of the SAR strip are preceded by longer ones to the north, up to a zone approximately coinciding with the 100-m bathymetry contour (see figure 5c). This behavior is also noticed, though not as evident, for system $n = 1$. Again, an

abrupt reduction of wavelength values approximately coincides with the same water depth. Detailed investigation of this along- α evolution will be included in section 6 below.

A summary of the main SAR-derived swell systems is presented in table 1. Figures 9a–c show joint-distribution plots of L_p and α_p , which graphically summarize these results. They have been constructed from the 256-by-256-pixel analysis and depict the joint distribution for all identified systems. Radius represents wavelength value, azimuth angle represents propagation direction (where the waves propagate to), and color, the number –or "density"– of occurrence of a given pair of L_p and α_p . The angular width and radial extent of a given patch, therefore, provide an estimation of the observed wave-field variability. In these figures, dominant systems have been labeled based on their density of occurrence, and their mean propagation directions α_n as well as mean wavelengths L_n . Patches not labeled indicate that the occurrence of detected peaks was below 15% of the total.

It is important to note that mean propagation direction of the most frequently detected wave systems appears aligned with the satellite track in all three cases (347.9° , 192.1° and 192.1° clockwise from North, for t_{SAR_1-3} , respectively). This effect has been documented by various authors [Wang & Jansen, 1998; Johnsen *et al.*, 2004] and is believed to be the result of the velocity bunching modulation transfer function R^{bunch} , which is the dominant imaging mechanism for the long swell recorded in Tehuantepec. Velocity bunching is known to control the overall loss of azimuth resolution but it also has the potential to act as a constructive modulation mechanism, particularly under low

wind conditions; either case has the potential to affect the strength and location of the true wave spectral peak. Nonetheless, there are other mechanisms playing an important role in the SAR imaging of ocean waves, like the so-called hydrodynamic modulation, which is still not fully understood and thus, subject of on-going research.

6. Comparison to in situ wave measurements

During the INTOA experiment, wave conditions were recorded at the Gulf of Tehuantepec by means of an ASIS buoy and three ADCP (Nortek-Aquadopp) from 22 February to 4 April 2005. The buoy was moored at 16° N and 95° W, about 22 km south-east of Salina Cruz harbor, at approximately 60 m of water depth. ADCP's were deployed at three coastal locations, where water depth was about 20 m: stations *Espigon* at 16.145° N, 95.202° W; *Castillo* at 16.088° N, 95.265° W; and *Chipehua* at 16.031° N, 95.356° (see figure 1 in *Ocampo-Torres et al.*, 2011). Sea-state conditions recorded in situ around the times of acquisition of the SAR images were relatively low, with $H_s < 1.5$ m overall and $H_{s\text{swell}} < 1.2$ m, corresponding to the swell partition. A summary of in situ wave records, averaged over four individual and consecutive measurements, is presented in Table 2. For convenience, registered peak frequencies f_p have been converted to wavelength L_p through the Fenton & McKee [1990] shallow water approximation given in equation (1), considering $h = 60$ m at the location of the ASIS buoy and $h = 20$ m, in the case of the three ADCP.

$$L = L_0 \tanh \left\{ \left(\frac{\omega^2 h}{g} \right)^{3/4} \right\}^{2/3} \quad (1)$$

where, ω is the radian wave frequency, defined from the so called wave dispersion relation as $\omega^2=gk\tanh(kh)$, g is the acceleration of gravity, k is the wavenumber and L_0 is the deep-water approximation of the wavelength L . As shown on this table, values recorded by the ADCP are quite consistent with those from the buoy, particularly H_s . Discrepancies, especially on wavelength and direction, may be explained by the shallower water depth at which ADCP were deployed: while differences in $H_{s\text{swell}}$ values are only slightly relevant on the 18 March case (i.e., ADCP records are consistently smaller), ADCP reported shorter waves, up to 25–35%, than the buoy. Large differences in $\alpha_{p\text{swell}}$ values are presumably due to wave refraction induced by local bathymetry.

SAR-derived wave parameters collocated to in situ measurements are available only from the 26 February and 2 March set of images; the ground-track of the 18 March set ran too far east and missed the location of all instruments (figure 3c). Table 3 shows collocated wave parameters derived from the 256-by-256- and 512-by-512-pixel subimages. For statistical robustness, included values have been averaged from up to four (three) contiguous subimages in the case of the 256-by-256-pixel (512-by-512-pixel) set. According to our results, the SAR-derived H_s and L_p values from the 26 February 256-by-256-pixel subimage set agree quite well with in situ measurements (table 2), particularly with those recorded by the buoy, where differences lie within 10% of the true (i. e., in situ) value. Larger differences, up to 22%, exist with respect to ADCP stations *Espigon* and *Chipehua*. Propagation directions α_p agree the least, with angular differences of 10–30°. Overall agreement tends to improve when comparing the wave

field derived from the 512-by-512-pixel subimages. L_p agreement advances to 7% while α_p differences fall to ca. 0–30°. Wave height differences, however, increase from 5% to 15%.

Contrastingly, the SAR-derived H_s corresponding to the 2 March set is consistently overestimated with respect to measured values, by 30% in average, but raising up to 90% close to the ASIS buoy. While the measured wave height corresponding to the swell partition averages $H_{s\text{swell}} = 1$ m, SAR-derived $H_{s\text{SAR}} \approx 1.5$ m overall, increasing to 90% overestimation when compared to the ASIS data. Overestimation of H_s by the SAR has been reported in previous studies. *Collard et al.* [2005] suggest that an overestimation of up to 70% in H_s values, particularly at low incidence angles, may be the result of an underestimation of the tilt modulation transfer function R^{tilt} during low wind conditions. In a previous study, *Johnsen et al.* [2004], propose that an overestimation of SAR-derived H_s at low wind speeds could be due to the effect of using the low-resolution scatterometer-based CMOD [*Stoffelen & Anderson*, 1997] geophysical function in the wave retrieval. Regarding L_p and α_p values, discrepancies in the order of 20% and 30° respectively, exist. This is slightly larger than values reported by *Wang & Jansen* [1998], who confirmed the results of previous studies where the mean absolute differences between SAR and in situ measurements of peak wavelength and direction were approximately 15% and 15°, respectively. Nonetheless, larger differences may be due mainly because in our case, the SAR registered two well-defined wave systems (see spectrum in figure 4b above) at these locations, whereas only one system was recorded by the buoy. A similar behavior was observed by *Johnsen et al.* [2004], who reported

cases where the ENVISAT ASAR consistently added information on ocean-swell beyond what a numerical model predicted. *Wang & Jansen* [1998] also suggested that velocity bunching tends to shift α_p values towards the azimuth direction while shortening their corresponding wavelengths. In our study, we observe this type of behavior since most of the SAR-derived L_p values are shorter than measurements (see tables 2 and 3).

Figures 10 and 11 show examples of in situ $S(f,\alpha)$ and SAR-derived $S(k,\alpha)$ spectra representing the wave fields from t_{SAR_1} and t_{SAR_2} , respectively. As may be appreciated on figures 10a and 10b, spectral shapes are not identical but integral parameters agree relatively well; particularly H_s values, which differ by a few centimeters. Wavelength and propagation direction differ by some 45 m and 30°, respectively. As discussed above, the SAR-derived spectrum shows information not included by the ASIS's spectrum, corresponding to three additional swell systems (two longer and one shorter than the peak) all propagating to 0–10°. Figures 10c and 10d depict in situ and SAR-derived spectra corresponding to station *Castillo*, respectively. Well in accordance to literature, the more energetic hence steeper peak appears shorter $L_{p,\text{SAR}} = 212$ m and shifted to the west $\alpha_{p,\text{SAR}} = 350^\circ$, towards the azimuth direction (348° in ascending path), in comparison to ground-truth value $L_{p,\text{ADCP}} = 234$ m ($f_{p,\text{ADCP}} = 0.058$ Hz at $h = 20$ m). A shorter swell-system ($L_{p,\text{SAR}} \approx 180$ m) propagating to the NE is not well defined on the ADCP spectrum.

Contrasting with the above, in situ spectra corresponding to t_{SAR_2} show well-defined narrow-banded energy representing longer-crested swell-systems (figures 11a and 11c). While the ASIS buoy detected only one single system which propagated to the NE,

further inshore *Espigon* station registered three: two longer ones propagating to the NE and a shorter one, less energetic to the NW. Total significant wave height $H_{s_{\text{tot}}}$ agrees well among in situ records, but it's significantly overestimated ($\sim 100\%$) by the SAR (figures 11b and 11d). According to literature, SAR-derived wavelength $L_{p_{\text{SAR}}}$ is shorter close to the buoy, $L_{p_{\text{SAR}} @ \text{ASIS}} = 301 \text{ m}$ and $L_{p_{\text{ASIS}}} = 327 \text{ m}$ ($f_{p_{\text{ASIS}}} = 0.062 \text{ Hz}$ at $h = 60 \text{ m}$), but slightly longer further inshore, $L_{p_{\text{SAR}} @ \text{ADCP Espigon}} = 262 \text{ m}$ and $L_{p_{\text{ADCP}}} = 234 \text{ m}$ ($f_{p_{\text{ADCP}}} = 0.058 \text{ Hz}$ at $h = 20 \text{ m}$), respectively. Nonetheless, note that the peak of the energy on the SAR-derived spectrum in figure 11b is not detected by the buoy (figure 11a). While the latter propagates towards the NE ($\alpha_{p_{\text{ASIS}}} = 21^\circ$), the former, much shorter, propagates to $\alpha_{p_{\text{SAR}} @ \text{ASIS}} = 355^\circ$; it is a secondary peak, less energetic, the one that propagates to the NE at $\alpha_{p_{2,\text{SAR}} @ \text{ASIS}} = 10^\circ$. Again, as mentioned by *Wang & Jansen* [1998] it appears shifted towards the satellite's azimuth direction, which in this case is approximately 192° (descending path). This behavior seems not have any effect on the spectrum in figure 11d in which SAR-derived peak waves near *Espigon* propagate slightly east $\alpha_{p_{\text{SAR}} @ \text{ADCP Espigon}} = 35^\circ$ of those recorded in situ, $\alpha_{p_{\text{ADCP}}} = 25^\circ$ (figure 11c).

6.1. Location of source-storms

In order to complement the limited comparison between in situ measurements and collocated SAR-derived wave parameters, an extended analysis may be achieved by comparing the time evolution of peak frequency f_p with the space evolution of peak wavelength L_p along its corresponding mean propagation direction $\alpha_{p_{\text{mean}}}$. The former analysis has been long performed in order to determine the origin and location of storms,

sources of basin-persistent swell waves (see for example *Snodgrass et al.*, 1966 and more recently, *Collard et al.*, 2009). We found evidence of eleven swell-events on the ASIS buoy's records. Figure 12 shows a time series of wave frequency spectra $S(f)$; shades of blue clearly depict the typical slanting ridges of spectral energy. Peak frequencies have been overlaid as black marks and pink dashed lines represent their corresponding least-squares fit to individual swell-events. According to theory, the intercept with the x-axis indicates the temporal origin t_0 of a given event, while the distance from the buoy to the source-storm Δ is related to the slope of the fit (df/dt) through equation (2)

$$\Delta = \frac{g}{4\pi} \frac{dt}{df} \quad (2)$$

where t and f are the time and frequency axes, respectively. In this figure, the vertical axis (frequency) stops at $f = 0.12$ Hz in order to focus only on swell events; hence, the fetch-limited wind waves generated locally by the strong *Tehuano* events shown in figure 1 are not included. It may be noted that the signal corresponding to at least two swell-events (in the frequency interval 0.05 Hz $< f < 0.11$ Hz) occur all times. In particular, at the times of acquisition of the three sets of SAR images (t_{SAR_1-3}), swell-events E01–02, E03–05 and E09–11, respectively, were recorded. According to our calculations, all these were generated at an average distance of 11,500 km away from the buoy. Time of swell generation t_0 and propagation distance Δ are summarized in Table 4. Date and time of swell arrival, as well as travel time in hours, is also included for all

eleven events.

Figure 13 shows a plot of SAR-derived peak wavelength L_p against propagation distance Δ_a in degrees of arc along its mean propagation direction $\alpha_p = 16.5^\circ$. Data corresponds to swell system $n = 2$ from the March 18 set of images shown in figure 8b. L_p values seem to increase gently with distance, up to a point where a sudden decrease occurs, near the coast, due to shoaling. The dashed line represents the least-squares fit to the data and its positive slope confirms the wavelength increase along-path. It is important to mention that decreasing L_p values corresponding to water depths shallower than 200 m (shown at the far right on figure 13) have not been considered in the analysis. Based on the principle discussed above, we were able to determine a given swell-system's distance to its origin through

$$\Delta_1 = (\Delta_2 + \Delta_a) \sqrt{\frac{L_{p2}}{L_{p1}}} \quad (3)$$

where Δ_1 is the distance between the hypothetical source-storm and the origin of the fit line in figure 13 ($\Delta_a = 0$), $\Delta_2 = \Delta_1 + \Delta_a$, and L_{p1} and L_{p2} are wavelength values corresponding to Δ_1 and Δ_2 , respectively. Once Δ_1 is derived through an iterative process, it is possible to approximate the location of the source-storm by back-tracking its full propagation distance Δ along its mean peak direction α_{p_mean} . Time of swell generation t_0 is simply estimated by subtracting the system's travel time (Δ divided by the group celerity c_g) from the corresponding SAR acquisition time. Distance to origin and time of swell generation were found to be $\Delta = 8,500$ km and $t_0 = 9$ March 2005 at 17:00 h UTC

for the example in figure 13. While the latter agrees quite well with results from E10 shown in table 4, $t_0 = 9$ March 2005 at 11:00 h UTC, distance to origin differs by nearly 1,500 kilometers. Nonetheless, these results agree relatively well with the location of a storm system derived from the blended QuikSCAT wind product described in section 2.

This analysis was performed on all three sets of SAR images; however, fits with positive slopes $dL_p/d\Delta_a$ (where wavelength values increase with distance along-path) were found only for systems $n = 4$ from the 26 February set, $n = 1-2$ from the 2 March set and $n = 1$ and 4 from the 18 March set (apart from $n = 2$ presented above). Table 5 shows the results from this analysis; except those from the 2 March set, results look reasonable. Distances to origin Δ and travel time in hours are comparable to the corresponding values derived from the ASIS buoy's records (shown in table 4). The large values from the 2 March set are due to the relatively low fit slopes $dL_p/d\Delta_a$ compared to the other cases. This in turn is due to the fact that, for these particular swell partitions, wavelength distribution along the observed travel path is rather homogeneous. Along-path homogeneity could reflect a generating storm relatively steady (and/or stationary) over a long period of time. Source-storm location based on this analysis has been contrasted nonetheless with wind-field maps derived once again from the blended QuikSCAT data. Strong, storm-force winds have been identified at or close to the location of the point-source indicated by the SAR results of table 5: Δ along α_{p_mean} at t_0 . An overall good agreement was found when considering the ca. 15° mean absolute differences confirmed by *Wang & Jansen [1998]*.

7. Conclusions

The spatial variability of the wave field during the INTOA experiment was studied through the analysis of SAR images of the ocean surface. With the main objective of investigating the evolution of the SAR-derived ocean wave spectrum $S(k, \alpha)$, our study was based on the analysis of three sets of four consecutive ENVISAT ASAR SLC images acquired over the Gulf of Tehuantepec and adjacent Pacific on 26 February, 2 and 18 March 2005, close to the final stage of three moderate–strong gap-wind events. SAR-inverted spectra, derived following *Collard et al.* [2005], revealed a strong variability of the wave field over a sea-surface of approximately 100 km by 400 km, with complex, multi-peaked spectra frequently estimated. An interesting such case was observed on the 26 February set, off the gulf, where long swells generated at the southern hemisphere met those generated by North Pacific storms. Spectral energy from the latter was seldom observed north of about latitude 15.25° , likely because the western end of the Gulf of Tehuantepec would play an obstructing role to these waves. SAR analysis showed that overall sea-state conditions in deep waters were low to moderate, with dominant systems (i.e., the most frequently observed) ranging $L_p = 190\text{--}311$ m and $H_s = 0.3\text{--}1.9$ m and propagating towards the coast, closely aligned to the azimuth direction. Intermediate- and shallow-water transformations (shoaling and refraction) were consistently observed on spectra derived from nearshore subimages, particularly those located in water depths under 100–200 m.

Wavelength variability from individual swell systems was of 11% in average for scales as small as tens of kilometers. Joint-distribution plots of L_p and α_p revealed that

the mean propagation direction of the dominant wave systems approximately coincide with the satellite track in all three cases: 347.9° , 192.1° and 192.1° clockwise from North, for $t_{\text{SAR_1-3}}$, respectively. This effect has been documented before and is believed to be the result of the velocity bunching modulation transfer function R^{bunch} , which is the dominant SAR imaging mechanism in our case (long swell propagating in the near-azimuth direction).

SAR-inverted spectra as well as derived wave parameters compared relatively well with in situ measurements registered during INTOA: three ADCP deployed at approximately 20-m water depth and an ASIS buoy moored at the 60 m bathymetry contour, whose calculated spectra reflected the complex, multi-system nature of the wave field observed through SAR analysis. Subimages collocated to in situ records were available only from the 26 February and 2 March set of images, since the ground-track of the 18 March set ran too far east and missed the location of all instruments. SAR-derived H_s from the 26 February set agreed quite well with measurements, where differences lie within 10% of true (i.e., in situ) value. Larger deviations, up to 22%, exist with respect to L_p values, the SAR usually underestimating the field records; especially with respect to ADCP stations. Propagation directions α_p agree the least, with angular differences of $10\text{--}30^\circ$. Contrastingly, L_p values derived from the 2 March set overestimated ADCP values by 18% in average, but underestimated the buoy's by as much as 30%. SAR-derived H_s was consistently overestimated with respect to measured values, by 30% in average, but rising up to 90% when compared to the buoy's records. While ADCP-measured wave height corresponding to the swell partition averaged $H_{s,\text{swell}}$

$= 1$ m, SAR-derived $Hs_{SAR} \approx 1.5$ m overall. Wave height overestimation by the SAR has been reported in literature to be the result of an underestimation of the tilt modulation transfer function R^{tilt} during low wind conditions, or the effect of using the low-resolution scatterometer-based CMOD geophysical function in the wave retrieval. In any case, deviations from measured values extend a little beyond ranges reported in literature by *Wang & Jansen* [1998], *Johnsen et al.* [2004] and *Collard et al.* [2005; 2009].

Finally, analysis of wavelength variability along the mean peak propagation direction allowed us to approximate the time of generation t_0 and origin of some of the detected swell systems. Even though agreement with respect to traditional [*Snodgrass et al.*, 1966] and recent [*Collard et al.*, 2009] methodologies is not strong, results are quite promising. We believe nevertheless that accuracy should improve for longer along-path propagation distances Δ_a .

8. Acknowledgements

Most of this work was performed while on an academic stay at LOS-IFREMER under the supervision of its director, Dr. B. Chapron. Stay was possible thanks to financial support from IFREMER, UABC and CONACyT (Programa de Becas Mixtas). Authors would like to acknowledge the assistance of Dr. F. Collard from CLS-BOOST who granted access to the SAR processing software SARTool ©. Our gratitude goes as well to Dr. S. Lehner from the German Aerospace Center (DLR) for providing a compilation of Matlab © routines for additional SAR image processing. Acknowledge goes as well to ESA for providing access to ENVISAT ASAR imagery. Additional

support was provided by CONACyT through project DIROC-IOA (CB-2006/62520).

9. References

- Blackburn, M. (1962), An oceanography study of the Gulf of Tehuantepec, *U. S. Fish Wildl. Serv. Spec. Sci. Rep. Fish.*, 404, 28 pp.
- Brandhorst, W. (1958), Thermocline topography, zooplankton standing crop, and mechanisms of fertilization in the Eastern Tropical Pacific. *Conseil Permanent International Exploration de la Mer, Journal du Conseil*, 24(1), 16–31.
- CERSAT (2002), QuikSCAT Scatterometer mean wind field products - user manual. Version 1.0., *Document C2-MUT-W-03-IF. IFREMER*, February 2002.
- Chapron, B., H. Johnsen and R. Garello (2001), Wave and wind retrieval from SAR images of the ocean, *Ann. Telecommun.*, 56, 682–699.
- Chelton D., M. Freilich and S. Esbensen (2000), Satellite observations of the wind jets off the Pacific Coast of Central America - part I: case studies and statistical characteristics, *Monthly Weather Review*, 128, 1993–2018.
- Collard, F., F. Arduin, and B. Chapron (2009), Monitoring and analysis of ocean swell fields from space: New methods for routine observations, *J. Geophys. Res.*, 114, C07023, doi: 10.1029/2008JC005215.
- Collard, F., F. Arduin, and B. Chapron (2005), Extraction of coastal ocean wave fields from SAR images, *IEEE J. Oceanic Eng.*, 30(3), 526– 533.
- Díaz Méndez, G. M., F. J. Ocampo-Torres, P. Osuna, H. García and R. Durazo (2008), Effects of gap-winds on multi-modal ocean swell systems at the south Pacific coast of

- Mexico, paper presented at SeaSAR 2008 Workshop, European Space Agency, Frascati, Italy.
- Fenton, J. D. and W. D. McKee (1990), On calculating the lengths of water waves, *Coastal Engng.*, 14(6), 499–513, doi: 10.1016/0378-3839(90)90032-R.
- Graber H. C., E. A. Terray, M. A. Donelan, W. M. Drennan, J. C. V. Leer and D. B. Peters (2000), ASIS - a new air-sea inter-action spar buoy: design and performance at sea, *J. Atmos. Ocean. Technol.*, 17, 708–720
- Holt, B., A. Liu, D. Wang, A. Gnanadesikan, and H. Chen (1998), Tracking storm-generated waves in the northeast Pacific Ocean with ERS-1 synthetic aperture radar imagery and buoys, *J. Geophys. Res.*, 103(C4), 7917–7929.
- Johnsen, H., G. Engen and B. Chapron (2004), Validation of ASAR wave mode level 2 product using WAM and buoy spectra, paper presented at Coastal and Marine applications of SAR, European Space Agency, SP-565, Svalbard, Norway.
- Li, X., S. Lehner and W. Rosenthal (2010), Investigation of ocean surface wave refraction using TerraSAR-X data, *IEEE Trans. Geosci. Remote Sens.*, 48, 830–840.
- Monaldo, F. (1991), The consequences of sampling variability on the estimation of wave number and propagation direction from spaceborne SAR image spectra, *IEEE Trans. Geosci. Remote Sens.*, 29(1), 113–119.
- Ocampo-Torres, F. J. (2001), On the homogeneity of the wave field in coastal regions as determined from ERS-2 and RADARSAT synthetic aperture radar images of the ocean surface, *Sci. Mar.*, 65, 215–228.
- Ocampo-Torres, F. J., H. Garcia-Nava, R. Durazo, P. Osuna, G. M. Díaz Méndez. and H.

- C. Graber (2011), The intOA Experiment: a study of ocean-atmosphere interactions under moderate to strong offshore winds and opposing swell conditions in the Gulf of Tehuantepec, Mexico, *Boundary-Layer Meteorology*, 138, 433–451, doi 10.1007/s10546-010-9561-5.
- Roden, G.I. (1961), On the wind driven circulation in the Gulf of Tehuantepec and its effect upon surface temperature, *Geofísica Internacional* 1(3), 55–72.
- Snodgrass, F. E., G.W. Groves, K. Hasselmann, G. R. Miller, W. H. Munk and W. H. Powers, (1966), Propagation of ocean swell across the Pacific, *Philos. Trans. R. Soc. London, Ser. A*, 249, 431–497.
- Stoffelen, A. and D. Anderson (1997), Ambiguity removal and assimilation of scatterometer data, *Quarterly Journal of the Royal Meteorological Society*, 123, 491–518.
- Violante-Carvalho, N., I. Robinson, C. Gommenginger, L. M. Carvalho and B. Golstein (2010), On the spatial homogeneity of the wave spectra in deep water employing ERS-2 SAR Precision Image, paper presented at SeaSAR 2010 Workshop, European Space Agency, Bergen, Norway.
- Wang, H. T. and R. W. Jansen (1998), Approximate evaluation of the distortion to the peak ocean wavelength and direction derived from SAR image spectra, *Ocean Engng.*, 25(4–5), 243–259

Tables

Table 1. Summary of swell systems detected from the SAR-inverted spectral analysis.

Date (mm/dd)	swell system	occurrence (%)	L_p (m)		α_p (deg)	
			mean	std	mean	std
02/26	1	38.6	258.9	38.4	345	7
	2	30.4	260.9	40.6	115	7
	3	24.8	245.7	42.0	10	6
03/02	1	57.6	246.9	18.6	3	6
	2	24.9	243.7	33.3	348	3
03/18	1	51.8	288.2	18.9	16	4
	2	24.7	287.9	16.4	343	9

Table 2. Summary of in situ measurements (averaged over four consecutive measurements) approximately coinciding with the SAR-image acquisition times t_{SAR_1} (February 26 2005 at 4:20h UTC), t_{SAR_2} (March 2 2005 at 16:20h UTC) and t_{SAR_3} (March 18 2005 at 16:17h UTC).

SAR set	H_{swell} (m)				$L_{\text{p_swell}}$ (m)				$\alpha_{\text{p_swell}}$ (deg)			
	ASIS	Espi.	Cast.	Chip.	ASIS	Espi.	Cast.	Chip.	ASIS	Espi.	Cast.	Chip.
t_{SAR_1}	0.5	0.5	0.5	0.4	233	234	237*	252	22*	25	8*	339
t_{SAR_2}	1.0	1.2	1.0	0.8	322	234	234	237	21	23	355	340
t_{SAR_3}	0.9	0.7	0.7	0.5	278	185	187	186	**	1	346	327

* Averaged from only two consecutive measurements, due to significant variation of the spectral peaks.

** Directional wave information was not available from the ASIS buoy after March 7 2005.

Table 3. Summary of SAR-derived wave parameters collocated to in situ measurements.

For statistical robustness, included values have been averaged from up to four (two) contiguous subimages in the case of the 256-by256-pixel (512-by-512-pixel) set.

SAR set	H_s _{swell} (m)				L_p _{swell} (m)				α_p _{swell} (deg)			
	ASIS	<i>Espi.</i>	<i>Cast.</i>	<i>Chip.</i>	ASIS	<i>Espi.</i>	<i>Cast.</i>	<i>Chip.</i>	ASIS	<i>Espi.</i>	<i>Cast.</i>	<i>Chip.</i>
$t_{\text{SAR_1}}$												
256_x	0.5	0.5	0.5	0.5	236	190	220	220	3	359	352	12
512_x	0.5	0.4	0.3	0.4	257	220	228	252	351	352	354	348
$t_{\text{SAR_2}}$												
256_x	1.9	1.4	1.3	-	244	281	311	-	355	30	27	-
512_x	1.7	1.4	1.4	-	251	281	281	-	352	*	*	-

* Veered from 20° westward to 355°

Table 4. Point-source (time of generation t_0 and distance to recording device Δ ; after *Snodgrass et al.*, 1966) of swell events registered by the ASIS buoy during the winter–spring 2005 campaign at the Gulf of Tehuantepec.

event	date & time (UTC) of swell arrival	travel time (h)	t_0	Δ (km)
E-01	Feb 25 @ ~ 11 h	214	Feb 16 @ ~ 12 h	10,844
E-02	Feb 25 @ ~ 23 h	220	Feb 16 @ ~ 19 h	12,293
E-03	Feb 27 @ ~ 23 h	225	Feb 18 @ ~ 14 h	10,191
E-04	Mar 01 @ ~ 13 h	225	Feb 20 @ ~ 03 h	12,284
E-05	Mar 03 @ ~ 14 h	231	Feb 21 @ ~ 23 h	12,857
E-06	Mar 06 @ ~ 14 h	254	Feb 23 @ ~ 23 h	14,602
E-07	Mar 08 @ ~ 07 h	148	Mar 02 @ ~ 02 h	8,408
E-08	Mar 09 @ ~ 23 h	187	Mar 02 @ ~ 03 h	11,294
E-09	Mar 13 @ ~ 08 h	230	Mar 03 @ ~ 18 h	14,131
E-10	Mar 17 @ ~ 09 h	190	Mar 09 @ ~ 11 h	10,202
E-11	Mar 18 @ ~ 20 h	172	Mar 11 @ ~ 16 h	9,203

Table 5. Time of generation t_0 and distance to origin Δ for swell-systems derived through SAR analysis of peak wavelength variability along mean propagation direction α_{p_mean} . It is important to note that systems $n = 4$ from sets t_{SAR_1} and t_{SAR_3} originated in the northern hemisphere and were thus not measured by the ASIS buoy. System $n = 2$ from t_{SAR_3} corresponds to swell event E-10; while $n = 1$ and $n = 1$ and 2 from t_{SAR_2} do not show a clear correspondence to the swell events from table 4.

SAR set	swell system n	α_{p_mean} (deg)	travel time (h)	t_0	Δ (km)
t_{SAR_1}	4	115	294	Feb 13 @ ~ 12 h	10,672
t_{SAR_2}	1	348	406	Feb 13 @ ~ 18 h	14,450
	2	3	896	Jan 24 @ ~ 08 h	31,981
t_{SAR_3}	1	343	234	Mar 8 @ ~ 22 h	9,118
	2	16	213	Mar 9 @ ~ 17 h	8,395
	4	106	180	Mar 11 @ ~ 04 h	7,070

Figures.

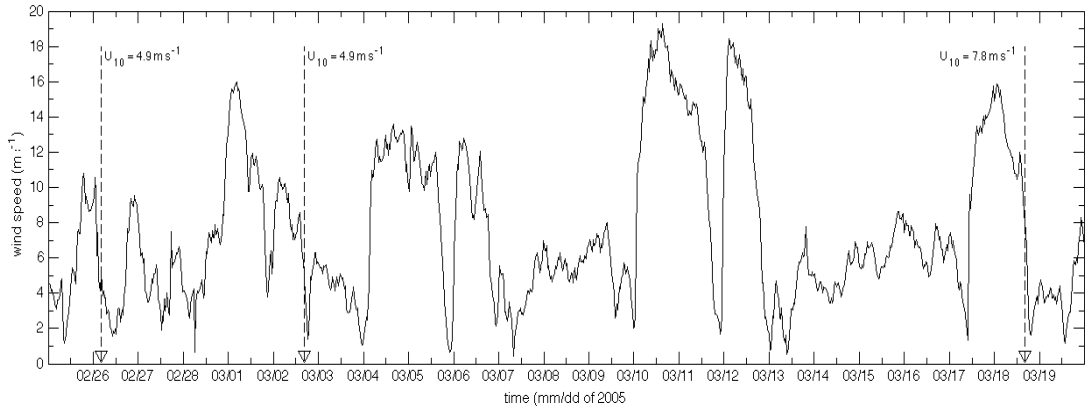


Figure 1. Time series of wind speed U_{10} (m s^{-1}) measured by the ASIS buoy during the INTOA experiment. Vertical dashed lines indicate the times of acquisition of the three sets of SAR SLC images $t_{\text{SAR_1-3}}$ analyzed in this study; Buoy's U_{10} recorded at are indicated.

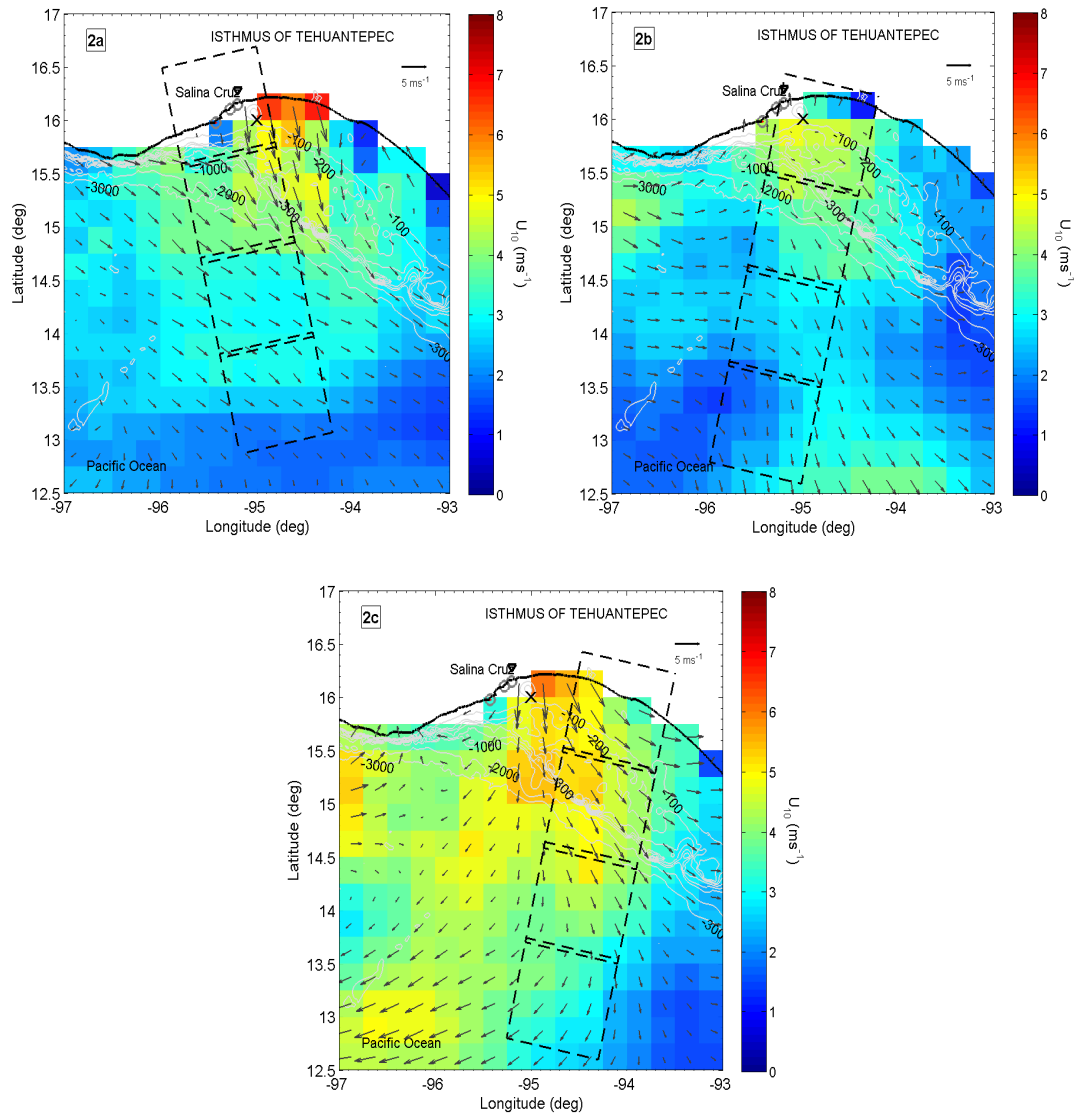


Figure 2. Synoptic wind field U_{10} at the study area derived from the blended QuikSCAT wind product [CERSAT, 2002] for a) February 26 2005 at 06h, b) March 2 2005 at 18h and, c) March 18 2005 at 18h UTC. Dash line squares represent the area covered by the corresponding SAR images. Black x mark indicates the location of the ASIS buoy; open circles, location of the three ADCP deployed during the INTOA experiment.

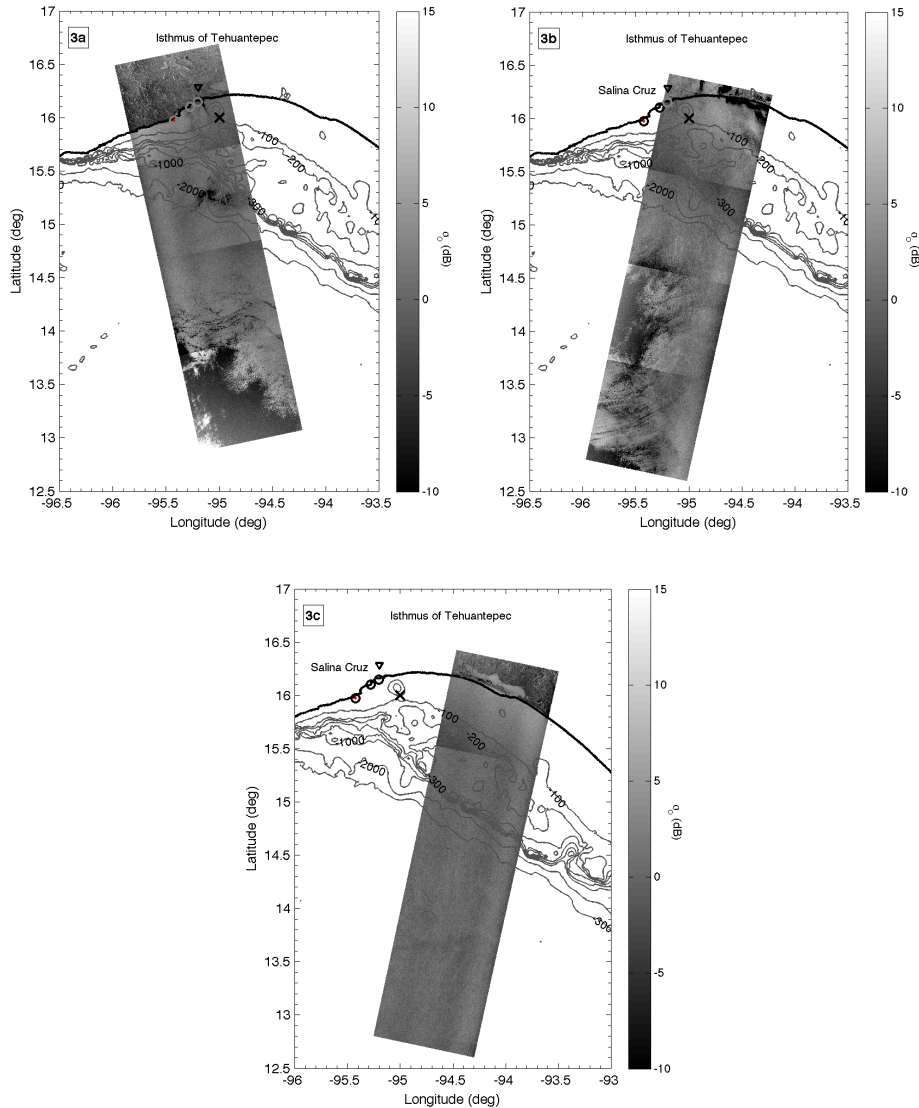


Figure 3. Location and coverage of the three sets of consecutive ENVISAT ASAR SLC images analyzed in this study, corresponding to a) February 26 2005 at 04:19–20 h, b) March 2 2005 at 16:20–21 h and, c) March 18 2005 at 16:17–18 h UTC. Black x mark indicates the location of the ASIS buoy; open circles, location of the three ADCP deployed during the INTOA experiment. Bathymetry contours are shown for reference.

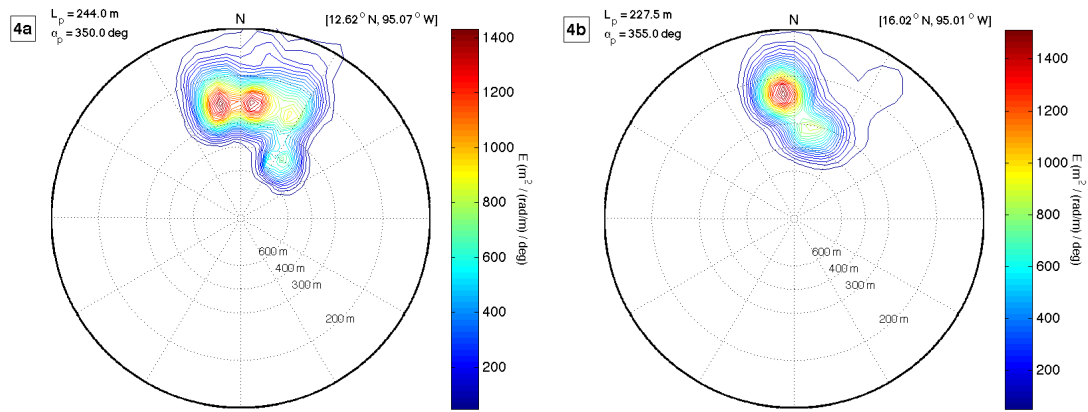


Figure 4. Examples of multi-peaked SAR-inverted wave spectra derived from two 256-by-256-pixel subimages of the March 2 2005 set: a) located about 400 km off-shore at 12.62°N and 95.07°W ; b) located close to the mooring of the ASIS buoy, at 16.02°N and 95.01°W , about 22 km SE of Salina Cruz harbor.

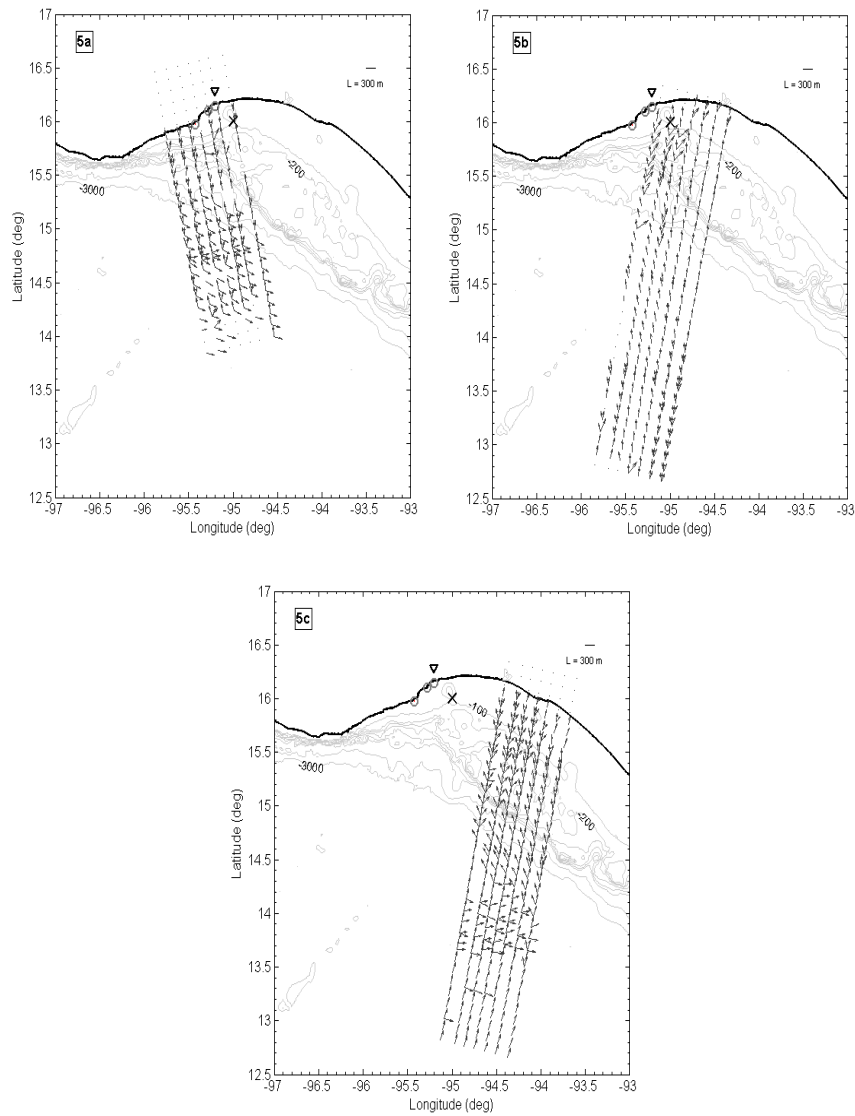


Figure 5. Spatial distribution of identified SAR-derived swell systems corresponding to acquisition times $t_{\text{SAR},1-3}$: a) February 26 2005 at 04: 19–20 h UTC, b) March 2 2005 at 16:20–21 h UTC and, c) March 18 2005 at 16:17–18 h UTC. Arrows correspond to vectors of wavelength L_p and propagation direction α_p . For simplicity, results from the 512-by-512-pixel analysis are shown.

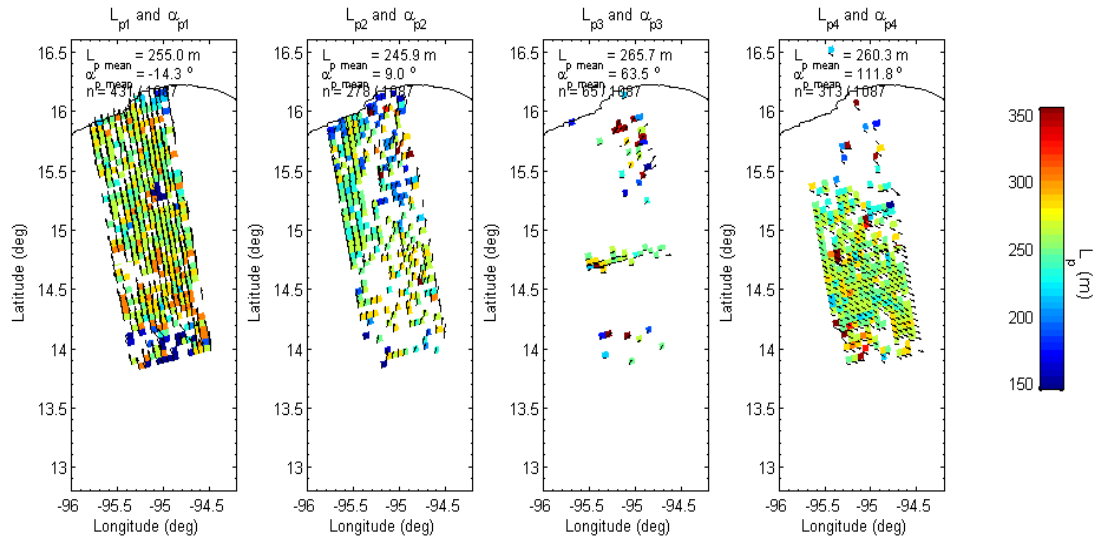


Figure 6. Maps of SAR-derived wavelength L_p and propagation direction α_p corresponding to the different partitions identified from the February 26 set. Colors indicate wavelength scale in meters; arrows, direction where waves propagate to.

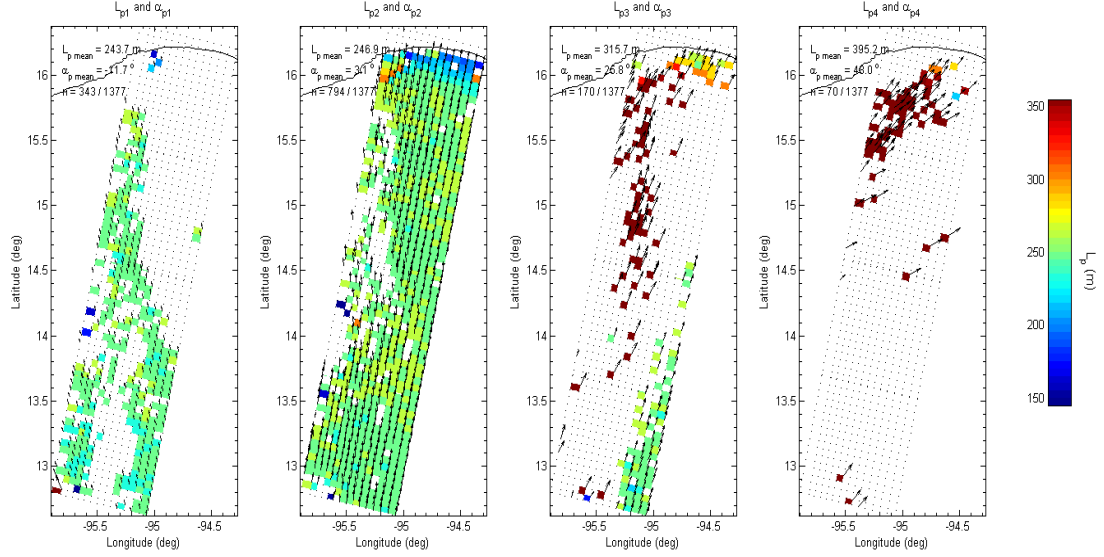


Figure 7. Maps of SAR-derived wavelength L_p and propagation direction α_p corresponding to the different partitions identified from the March 2 set. Colors indicate wavelength scale in meters; arrows, direction where waves propagate to.

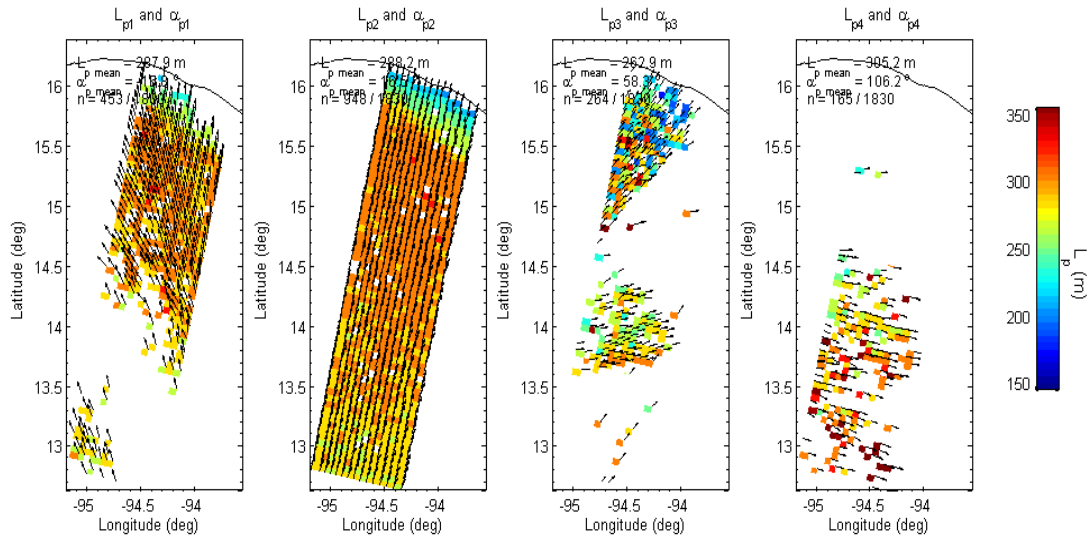


Figure 8. Maps of SAR-derived wavelength L_p and propagation direction α_p corresponding to the different partitions identified from the March 18 set. Colors indicate wavelength scale in meters; arrows, direction where waves propagate to.

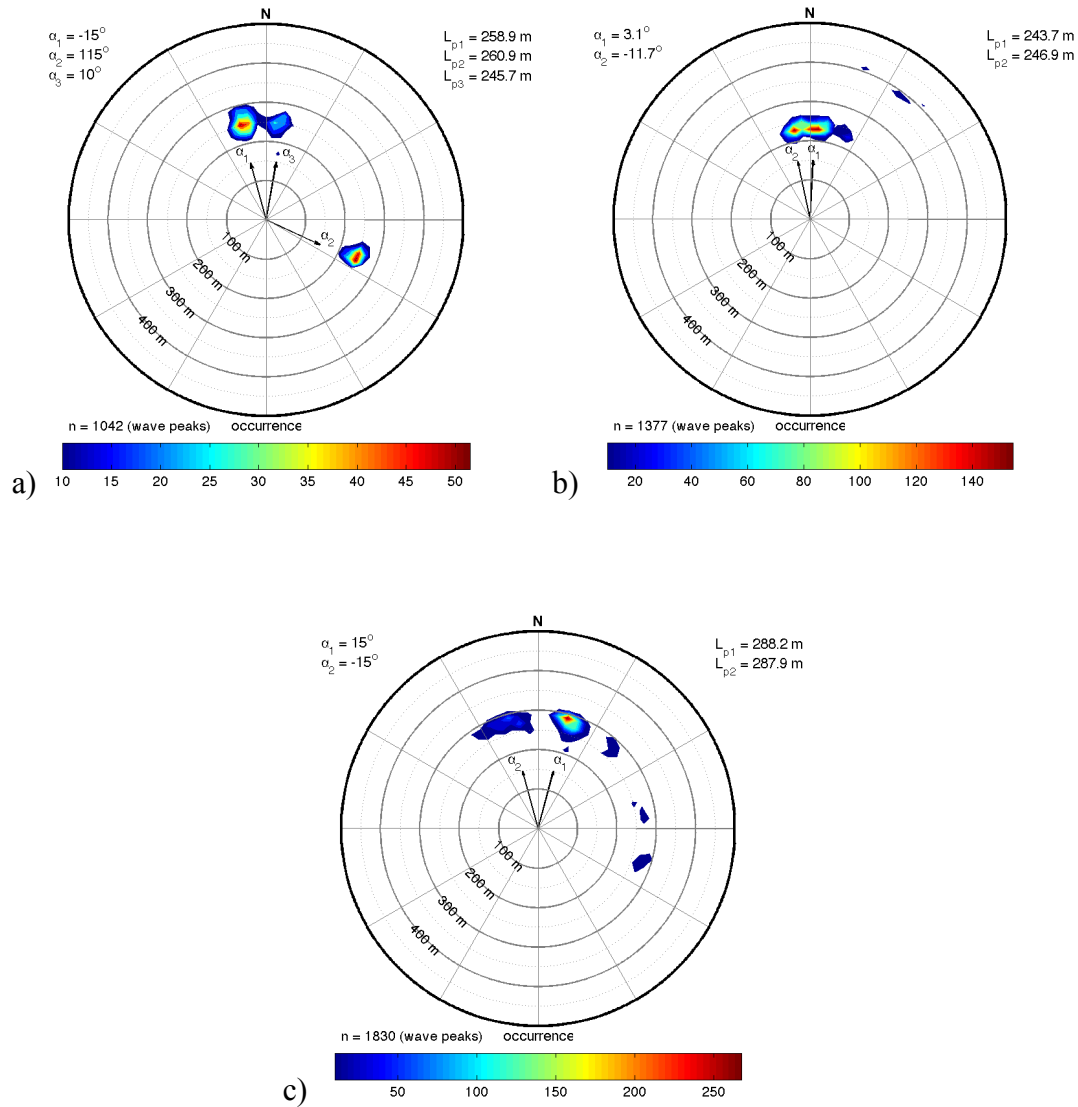


Figure 9. Joint-distribution plots of L_p and α_p for the various swell systems derived through SAR analysis from a) the February 26 set, b) March 2 and c) March 18 set. Black arrows indicate the mean propagation direction from the dominant systems.

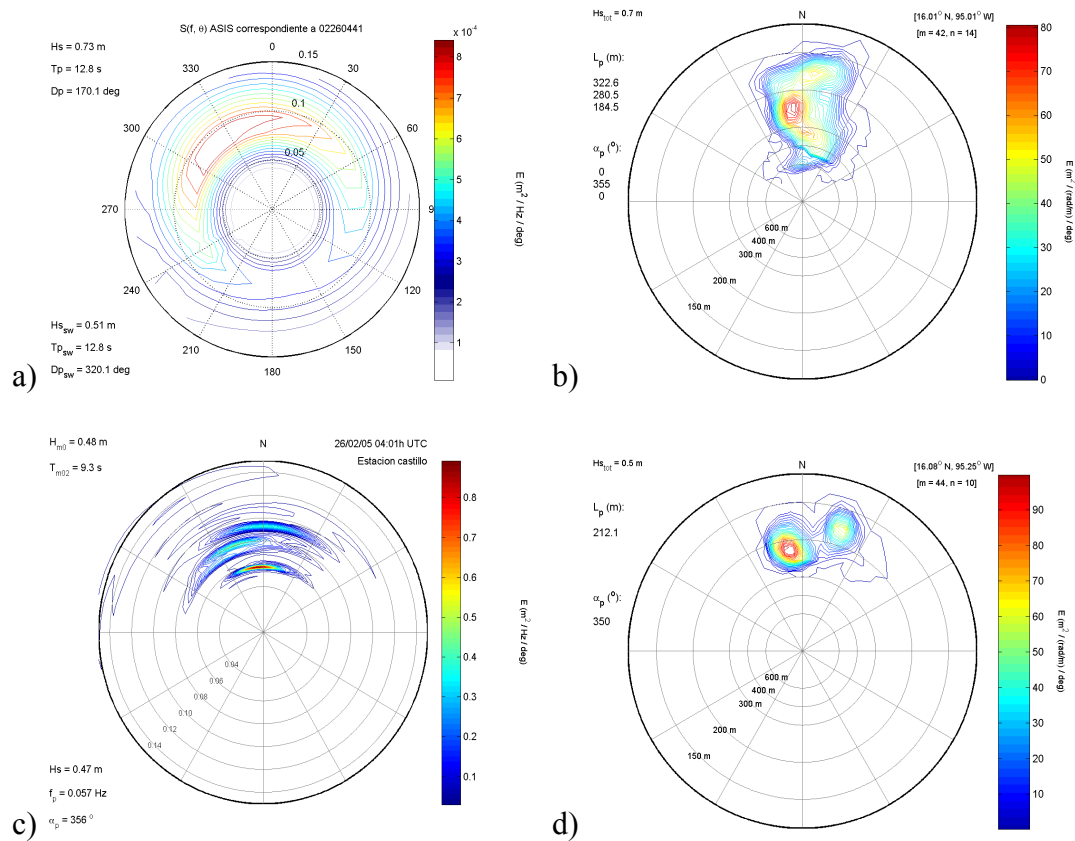


Figure 10. Directional wave spectra corresponding to 26 February 2005: a) derived from the ASIS buoy's records at 04:41h UTC; b) collocated SAR-derived spectrum from the 256 by 256 pixel subimage; c) derived from ADCP records at station *Castillo* at 04:01h UTC; and d) collocated SAR-derived spectrum

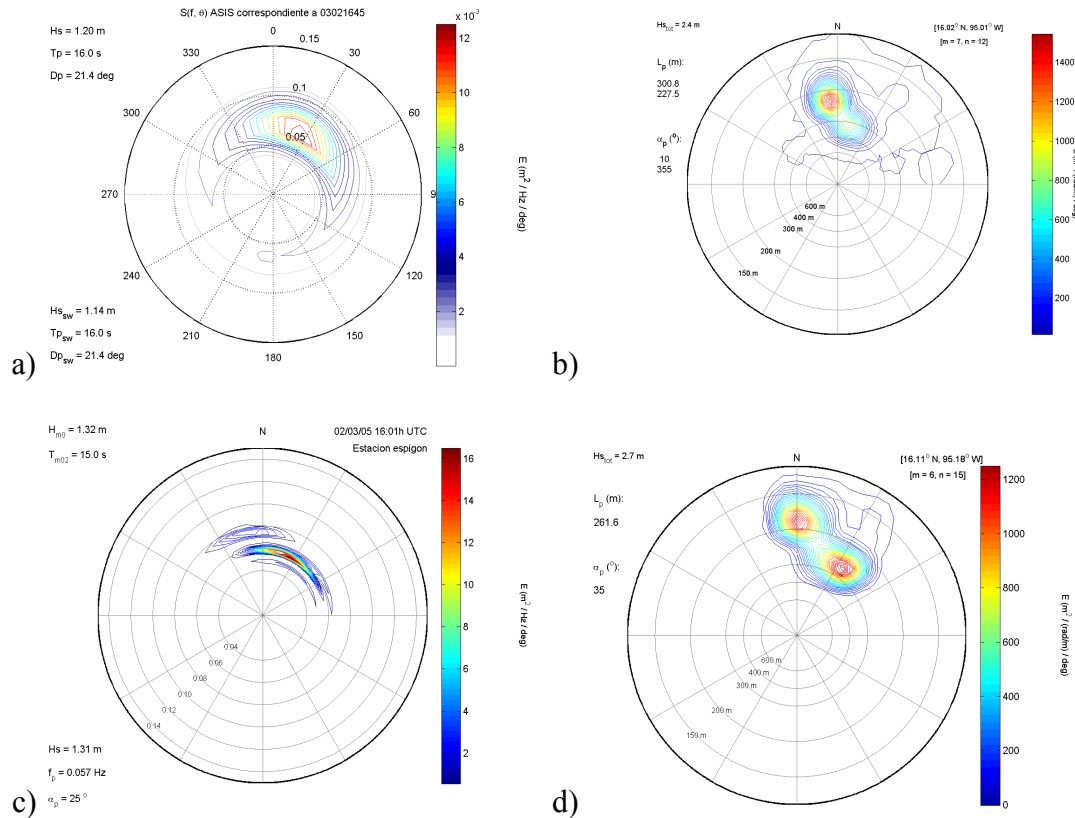


Figure 11. Directional wave spectra corresponding to 2 March 2005: a) derived from the ASIS buoy's records at 16:45h UTC; b) collocated SAR-derived spectrum from the 512 by 512 pixel subimage; c) derived from ADCP records at station *Espigon* at 16:01h UTC; and d) collocated SAR-derived spectrum

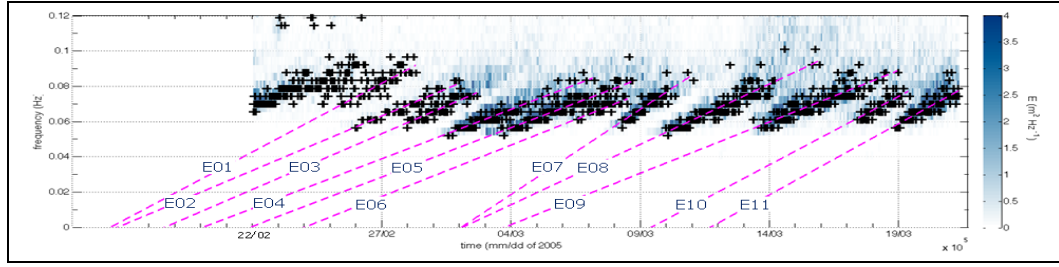


Figure 12. Time series of wave frequency spectra $S(f)$ registered by the ASIS buoy in 2005, during the INTOA experiment. Black crosses indicate peak frequency f_p from individual bursts (one every 30 minutes). Pink dashed lines represent least-square fits to clouds of f_p values corresponding to identified swell events.

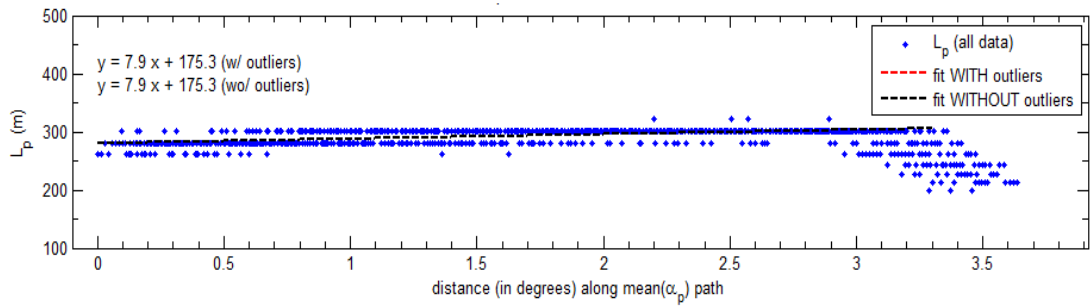


Figure 13. SAR-derived peak wavelength $L_{p,SAR}$ as a function of distance along its mean propagation direction $\alpha_{p,\text{mean}}$ corresponding to swell system $n = 2$ from the March 18 set. Blue dots (L_p values) at the right end of the plot represent wavelength shortening due to intermediate- and shallow-water effects; these data were not considered for the least-square fit (dashed black line).

IV. ESTIMACIÓN DEL ESPECTRO DE OLEAJE A PARTIR DE IMÁGENES DE LA SUPERFICIE DEL MAR ADQUIRIDAS CON TerraSAR-X.

Artículo en preparación

Resumen

El algoritmo propuesto por *Lai y Delisi* [2010] para obtener longitud de onda L y altura significante H_s del oleaje libre a partir de imágenes SAR en banda C de la superficie del mar ha sido adaptado y utilizado con imágenes de banda X del satélite alemán TerraSAR-X. Con el objetivo principal de investigar la evolución espacial del campo de oleaje en el Golfo de Tehuantepec y océano Pacífico adyacente durante eventos de viento intenso, esta primera aproximación nos ha permitido estimar el espectro bidimensional del oleaje libre a partir de una serie de imágenes de alta resolución del TerraSAR-X. Nuestra implementación difiere de su predecesor porque depende en información externa de viento requerida para calcular el nivel de energía del espectro en el rango de equilibrio, y tiene la limitación de no poder resolver la ambigüedad de 180° .

Estimation of wave spectrum from TerraSAR-X images of the ocean surface.

G. M. Díaz Méndez¹, F. J. Ocampo-Torres² and Pedro Osuna³

¹ Facultad de Ciencias Marinas, Universidad Autónoma de Baja California (UABC). Km 103 carretera Tijuana-Ensenada, Ensenada, Baja California. 22880. Mexico. Email: diaz.guillermo@uabc.edu.mx.

² Departamento de Oceanografía Física, Centro de Investigación Científica y Educación Superior de Ensenada (CICESE). Km 107 carretera Tijuana-Ensenada, Ensenada, Baja California. 22860. Mexico. Email: ocampo@cicese.mx.

³ Departamento de Oceanografía Física, Centro de Investigación Científica y Educación Superior de Ensenada (CICESE). Km 107 carretera Tijuana-Ensenada, Ensenada, Baja California. 22860. Mexico. Email: osunac@cicese.mx.

Abstract

The algorithm proposed by *Lai & Delisi* [2010] to retrieve swell wavelength L and significant wave height H_s from C-band synthetic aperture radar (SAR) images of the ocean surface has been adapted and applied to X-band SAR imagery from the German satellite TerraSAR-X (TSX). With the main objective of investigating the spatial evolution of the wave-field at the Gulf of Tehuantepec and adjacent Pacific during strong off-shore gap-wind conditions, this first approach allowed us to derive the 2D swell wave spectrum from a series of high-resolution TSX products. Our implementation

differs from its predecessor in that it relies on external wind information to derive the energy level at the equilibrium range of the spectrum, and has the shortcoming that it cannot resolve the 180° ambiguity of the spectrum. Nonetheless, it has been successfully tested on a dozen single-look complex (SLC) images acquired by the advanced SAR carried on-board the European environmental satellite (ENVISAT-ASAR) and proved to compare reasonably well to in situ wave records collected during a field campaign at the Gulf of Tehuantepec, Mexico in 2005. The algorithm has been then applied to standard 30-by-50-km TSX StripMap and larger coverage ScanSAR scenes with encouraging results. SAR-inverted wave parameters, H_{SAR} in the order of 0.7–1.5 m, $L_{\text{p,SAR}}$ in the order of 230–460 m and corresponding propagation directions $\alpha_{\text{p,SAR}} = -45^\circ$ to 45° , are in good agreement with Acoustic Doppler Current Profiler (ADCP) wave data recorded during a field campaign in 2008. Furthermore, moderate $H_{\text{SAR}}-L_{\text{p,SAR}}$ value pairs lie within the linear imaging regime proposed by *Alpers et al.* [1981] and investigated in *Díaz Méndez et al.* [2010].

Although originally developed for the RADARSAT and ENVISAT SAR imagery, our work sets forth the possibility to reliably derive wave parameters from new generation of X-band, lower-orbit missions, including TerraSAR-X, TanDEM-X and the Italian COSMO-SkyMed constellation.

1. Introduction

Launched in 2007, the German satellite TerraSAR-X carries an advanced X-band SAR system which delivers various types of microwave images of the Earth's surface

with ground resolution as high as one meter. TerraSAR-X images of the ocean surface have been used to investigate physical processes of both natural and anthropic origin. *Li et al.* [2009] used Spotlight (SL) and StripMap (SM) mode scenes to analyze wave refraction and diffraction around Terceira Island at the Azores. *Lehner* [2008, personal communication] used ScanSAR (SC), SM and SL scenes to derive high-resolution wind fields over the open ocean. Contrastingly, *Brusch et al.* [2010] took advantage of TerraSAR-X SAR's high spatial resolution to include them in ship surveillance and security applications. And in a previous analysis, *Díaz Méndez et al.* [2010] detected the signal of the fetch limited waves locally generated by gap-winds at the south Pacific coast of Mexico. However, to the best of our knowledge, there is no algorithm currently available to derive the 2D wave spectrum from TerraSAR-X or other X-band SAR. And there is a need, because there are other X-band SARs in space, such as the German TanDEM-X and the Italian COSMO-SkyMed mission, which is a constellation of four medium-size satellites.

Rationale for our work: This study departs from the recommendations of *Díaz Méndez et al.* [2010] who observed, on a series of TerraSAR-X image intensity spectra, a near-range signal presumably associated to the sea surface waves generated locally by the *Tehuano* gap-winds. Wave-number vectors \mathbf{k}_p corresponding to this signal were closely aligned with the off-shore blowing winds and decreased with distance to the shore, along the wind path, thus suggesting the possibility that they could be associated to the *Tehuano* waves. They compared the corresponding wavelengths L_p with the parametric wave-growth relations proposed by *Kahma & Calkoen* [1992] and found that

measured values were larger than predicted. They finally concluded that in order to further investigate these results, a wave-inversion scheme was desirable to properly derive true wave parameters from TerraSAR-X products. Therefore, the main objective of our work is to investigate the spatial evolution of the wave-field at the Gulf of Tehuantepec during strong off-shore wind conditions using high resolution X-band SAR images of the ocean surface like those acquired by the German satellite TerraSAR-X. In order to accomplish this, we have selected to adapt the wave-retrieval algorithm developed by *Lai & Delisi* [2010] for the high resolution TerraSAR-X imagery of the ocean surface.

This paper is organized in six sections including this Introduction. Section 2 presents the theoretical background which supports the inversion algorithm. Section 3 describes the algorithm. In section 4, validation exercises are presented. Section 5 includes the estimation of wave spectra and integral parameters from a few sets of TerraSAR-X images acquired over the Gulf of Tehuantepec. Finally, section 6 summarizes the findings of our work.

2. Theoretical background

The wave inversion algorithm for TerraSAR-X imagery presented in this paper has been adapted from the C-band algorithm proposed by *Lai & Delisi* [2010]. Their algorithm is based on the quasi-linear model of *Hasselmann & Hasselmann* [1991], where a complex modulation transfer function (MTF) relates the 2D-wave spectrum $S(\mathbf{k})_{\text{waves}}$ to the SAR image intensity spectrum $S(\mathbf{k})_{\text{SAR}}$ through

$$S(\mathbf{k})_{\text{SAR}} = M(\mathbf{k}) S(\mathbf{k})_{\text{waves}} \quad (1)$$

If the image forming mechanism is linear, the forward mapping expression given in (1) can be readily inverted to derive $S(\mathbf{k})_{\text{waves}}$ from a given SAR image intensity spectrum. According to *Hasselmann & Hasselmann* [1991], $M(\mathbf{k})$ represents the sum of various mechanisms which modulate the distribution of the microwave scatterers on the sea surface. *Lai & Delisi* [2010] proposed the following form

$$M(\mathbf{k}) = e^{-k_{\text{azim}}^2 \zeta^2} [iM^{\text{tilt}}(\mathbf{k}) + M^{\text{hydr}}(\mathbf{k}) + M^{\text{vb}}(\mathbf{k})] \quad (2)$$

where $M^{\text{tilt}}(\mathbf{k})$ refers to the tilt MTF, $M^{\text{hydr}}(\mathbf{k})$ is called the hydrodynamic MTF and $M^{\text{vb}}(\mathbf{k})$ represents the velocity bunching MTF. The exponential factor $\exp[-k_{\text{azim}}^2 \zeta^2]$ is an azimuthal cutoff factor in which k_{azim} is the ocean-swell wave-number vector component in the satellite flight (azimuth) direction and ζ^2 , the mean square azimuthal displacement of the scattering elements, defined as

$$\zeta^2 = \frac{\beta^2}{2|\mathbf{k}_0|^2} (\tau^{-2} + T_i^{-2}) \quad (3)$$

In Eq. (3), β is the slant range R to platform velocity V_{sat} ratio, k_0 is the radar wave-number, τ is a correlation time defined by *Plant & Zurk* [1997] and T_i is the SAR integration time. According to *Hasselmann & Hasselmann* [1991], the inclusion of this

factor represents a uniformly valid approximation of the non-linear SAR imaging theory for the entire spectrum.

Tilt modulation refers to variations on the radar cross-section σ_0 backscattered from the Bragg waves due to their location along the tilting profile of the longer (swell) waves. Its functional forms are [from *Hasselmann & Hasselmann* 1991]:

$$M^{tilt}(\mathbf{k}) = 8ik_{range}(\sin 2\theta)^{-1} \quad (4a)$$

$$M^{tilt}(\mathbf{k}) = 4ik_{range}\cot\theta(1+\sin^2\theta)^{-1} \quad (4b)$$

for horizontal (HH) and vertical (VV) polarizations, respectively; θ is the radar incidence angle and k_{range} is the swell wave-number vector component in the range direction. The hydrodynamic MTF relates the modulation of the scattering elements by the convergence and divergence of the ocean surface due to the propagation of the long waves. According to *Alpers et al.* [1981], it is characterized by a non-uniform distribution of the short waves with respect to the long ocean wave-field, attributed to the interactions between ripples and swell waves. They state that these interactions are valid for a relatively smooth sea, where non-linear effects which lead to steepening and eventually to breaking of the waves, are unimportant. Developed by *Alpers & Hasselmann* [1978], it is given by

$$M^{hydr}(\mathbf{k}) = \frac{\omega - i\mu}{\omega^2 + \mu^2} \frac{\omega}{|\mathbf{k}|} (\mathbf{k} \cdot \mathbf{k}_{Bragg}) \left[\left(\frac{\mathbf{k}}{E_{Bragg}} \cdot \frac{\partial E_{Bragg}}{\partial \mathbf{k}_{Bragg}} \right) - \gamma \frac{(\mathbf{k} \cdot \mathbf{k}_{Bragg})}{|\mathbf{k}_{Bragg}|^2} \right] \quad (5)$$

where ω is the radian frequency of the ocean waves, μ is a relaxation rate factor dependent on the near-surface wind, $\mathbf{k} = (k_{\text{azim}}, k_{\text{range}})$ is the wave-number vector of the ocean waves, $\mathbf{k}_{\text{Bragg}}$ is the wave-number vector of the Bragg backscattering waves, E_{Bragg} is the spectral energy density of the Bragg waves, and γ is a factor dependent on the surface tension and the density at the ocean surface. Following *Lai & Delisi* [2010], E_{Bragg} was derived from the equilibrium range part of the wave-number spectrum model from *Donelan & Pierson* [1997].

While the modulation processes mentioned above are characteristic of real aperture radar (RAR) systems, the velocity bunching MTF is characteristic of SAR systems. It is caused by the fact that SAR finds azimuth location of a target via the Doppler coordinate and that the motion of a target in range belies this relation. In the case of ocean waves, velocity bunching may produce wavelike patterns on the image even if no modulation of σ_0 by long waves occurs. A thorough discussion of the velocity bunching mechanism is presented in *Alpers et al.* [1981]. The functional form of the velocity bunching MTF is given by

$$M^{\text{vb}}(\mathbf{k}) = -\beta \omega k_{\text{azim}} \left(\cos \Phi - i \sin \Phi \frac{k_{\text{range}}}{\mathbf{k}} \right) \quad (6)$$

where Φ is the angle between the ocean waves and $\mathbf{k}_{\text{Bragg}}$ (which is aligned with the SAR look direction). According to these authors, the wave-field is mapped linearly onto the SAR image through the velocity bunching mechanism for a relatively narrow range of

sea-state conditions; and it is desirably so since, as mentioned above, in such case derivation of $S(\mathbf{k})_{\text{waves}}$ from a given SAR image intensity spectrum is possible. They presented a condition that needs to be fulfilled for velocity bunching to be a linear process. An expression in terms of the platform configuration β and the average velocity of the scatterers in the SAR look-direction, which is in turn related to the orbital motions of the ocean-swell. *Díaz Méndez et al.* [2010] analyzed this linearity condition for the case of young swell at the Gulf of Tehuantepec, presumably generated locally by the *Tehuano* winds, and found that for two of three cases, SAR imaging was nonlinear.

Finally, the 2D swell-spectrum is derived from

$$S(\mathbf{k})_{\text{waves}} = \frac{\rho_{\text{azim}} \rho_{\text{range}}}{4\pi^2 N_{\text{azim}} N_{\text{range}}} \frac{S(\mathbf{k})_{\text{SNR}}}{M(\mathbf{k})} \quad (7)$$

where ρ_{azim} , ρ_{range} , N_{azim} and N_{range} are the scene's resolutions and number of independent looks in the azimuth and range directions, respectively, and $S(\mathbf{k})_{\text{SNR}}$ is the signal-to-noise-ratio (SNR) spectrum defined as the ratio between the SAR image intensity spectrum $S(\mathbf{k})_{\text{SAR}}$ and the clutter noise level. The latter is assumed to be white and its value is obtained by averaging the lowest 2% of spectral values in a SAR spectrum [*Alpers & Hasselmann* 1982].

3. X-band wave inversion algorithm.

As mentioned earlier, the wave inversion algorithm implemented in this study to

derive wave parameters from the X-band SAR carried on-board the German satellite TerraSAR-X was adapted from the wave inversion algorithm set forth by *Lai & Delisi* [2010]. Figure 1 shows a flow diagram of the wave inversion algorithm adapted for TerraSAR-X imagery. As can be observed, a full size SAR image is subdivided into smaller n - by n -pixel size sub-image from which the corresponding 2D backscatter intensity spectrum is calculated. For convenience of the Fourier analysis, n is usually one of the following powers of two: 2^8 , 2^9 or 2^{10} . In order to estimate the corresponding MTFs, a series of SAR parameters are required, including the platform's height, speed V_{sat} and heading, the radar's nominal frequency f_0 , the system's integration time T_i , the scene's geographical coordinates, incidence angle θ , the azimuth and range resolutions and number of looks ρ_{azim} , ρ_{range} , N_{azim} and N_{range} , respectively, etc.

In their work, wind speed and direction required to estimate E_{Bragg} for $M^{\text{hydr}}(\mathbf{k})$ is derived directly from the SAR image through the CMOD4 geophysical model function (GMF) developed by *Stoffelen & Anderson* [1997] for VV-polarized scatterometer data. In our case, given the unavailability of a reliable CMOD-type GMF for X-band instruments, the required wind information is obtained from an external source. In many cases nevertheless, wind direction may be visually inferred from the SAR image itself through the signature which roll vortices, wind streaks and similar features imprint upon the ocean surface. If present, their orientation may be easily calculated through regular Fourier analysis. Therefore, in order to adequately reproduce the wind conditions at the Gulf of Tehuantepec, three different sources were compared to in situ data recorded during the INTOA experiment in 2005. These datasets are the blended QuikSCAT wind

product [CERSAT 2002] produced by CERSAT, IFREMER; the Cross-Calibrated Multi-Platform (CCMP) ocean surface wind product developed by NOAA/NASA [*Atlas et al.* 2009] and a special run of the ECMWF wind model kindly supplied by L. Cavalleri. Figure 2 shows a time series plot of measured wind speed U_{10} [details can be found in *Ocampo-Torres et al.* 2011] compared to these three wind products.

It may be easily noted that the special ECMWF data (red line) reproduces the measurements (green) pretty closely, particularly during the strong gap-wind events from March 2005. While all three sets have a spatial resolution of 0.25 degrees, ECMWF set has the best time resolution: one hour as opposed to the 6-hour interval of the other two. Therefore, this dataset will be used to supply wind data for the C-band SAR validation exercises in section 4. Given the fact that it is a special run processed for the 2005 INTOA campaign, its temporal coverage is rather limited and thus, the blended QuikSCAT wind product has been used otherwise.

It is important to mention that one of the shortcomings of our methodology is that it does not include a procedure to resolve the 180° ambiguity on the spectrum, like that proposed by *Engen & Johnsen* [1995].

4. Implementation validation

In order to test the performance of our implementation, a series of validation exercises have been carried out. These included the comparison of inverted swell-spectra and integral parameters derived from a series of C-band ENVISAT-ASAR SLC scenes to in situ wave data recorded at the Gulf of Tehuantepec in 2005. Table 1 lists the

general characteristics of these three sets of four consecutive SAR images. The table includes as well the characteristic of five X-band TerraSAR-X scenes to which the algorithm has been applied to, which will be discussed in the following section. The ENVISAT images were acquired at the final stage of three moderate-to-strong gap-wind events whose off-shore winds reached maximum values above 10 m s^{-1} . For a thorough description of these images as well as the corresponding synoptic wind and wave conditions please refer to *Díaz Méndez et al.* [in preparation], as well as to *Ocampo-Torres et al.* [2011] for a description of in situ data and campaign results.

Figure 3 shows examples of 2D wave spectra estimated from in situ measurements $S(f,\alpha)$ and collocated SAR-inverted spectra $S(k_x,k_y)$ derived through our algorithm implementation from an ENVISAT scene acquired on 2 March 2005 at 16:20h UTC. At a glance, spectral shapes from the $S(f,\alpha)$ and $S(k_x,k_y)$ spectra look very different, but they all exhibit a well-defined swell system propagating approximately to azimuth = 25° . All except the ASIS buoy's were able to resolve a second system of shorter waves, propagating closer to true North. Significant wave-height H_s values, nonetheless, match closely: $H_{s\text{swell}} = 1.1 \text{ m}$ from the buoy's (swell partition) and $H_{s\text{SAR}} = 1.4 \text{ m}$ from the SAR-inversion (figures 3a and 3c respectively); and $H_{s\text{ADCP}} = 1.3 \text{ m}$ from the ADCP at station Espigon, and $H_{s\text{SAR}} = 1.1 \text{ m}$, (figures 3b and 3d respectively).

One of the main differences between the buoy's and the ADCP's records is the water depth to which measurements belong: while the ADCP was deployed much closer to shore, at a depth of approximately 20 m, the buoy was moored 20 km off-shore, at a depth of 60–80 m. Any given deepwater wavelength L_0 would therefore be reported

shorter by the ADCP than by the ASIS buoy. Another important difference is that the buoy's records represent 30-minute averages, while the ADCPs sampled in hourly intervals. The SAR-inverted spectra were derived from 256-by-256-pixel sub-images; since the pixel size for these scenes is approximately 30 by 30 m, the spectra correspond to instantaneous images of a 7.6-by-7.6-km ocean surface. This is likely the main reason why measured and SAR-derived peak wavelengths Lp differ: $Lp_{\text{ASIS}} = 327$ m and $Lp_{\text{SAR}} = 437$ m; and $Lp_{\text{ADCP}} = 238$ m and $Lp_{\text{SAR}} = 266$ m.

SAR-derived spectra have been converted to $S(f)_{\text{SAR}}$ following *Johnsen et al.* [2003] in order to perform additional comparisons to in situ $S(f)_{\text{ASIS}}$ and $S(f)_{\text{ADCP}}$ spectra. Figure 4a shows a composite of seven spectra constructed from the ASIS's data, from 15:44h to 18:51h UTC, approximately one hour before and two after the time of acquisition of the SAR image (March 2 2005 at 16:20h UTC). The composite have been averaged and the resulting synthetic "mean" spectrum is plotted (thick black curve) as a summary. While the mean peak-frequency $f_{p_mean} = 0.0608$ has been calculated from this mean spectrum, the mean significant wave height $Hs_{\text{mean}} = 1.1$ m corresponds to the average of the Hs values from each spectrum of the composite. Similarly, figure 4b includes a composite derived from the ADCP's records at station Espigon. Spectra corresponds to 2 March 2005 from 15:01h to 18:01h UTC. As expected, average values are quite similar to the buoy's, $Hs_{\text{mean}} = 1.2$ m and $f_{p_mean} = 0.0596$. The main difference between the two is that the ADCP detected a third swell-system at a lower frequency than the peak; meanwhile, the buoy detected only two systems.

Validation of the algorithm has also been carried out through direct comparison to

wave-inversion results derived following *Collard et al.* [2005]. Figure 5a shows a scatter plot of swell significant wave-height $H_{s\text{swell}}$ derived from the latter and results from our implementation. This example corresponds to ENVISAT-ASAR SLC image acquired on 2 March 2005 at 16:20h UTC and subimage size is 512 pixels on the side. As may be noted of the figure, our algorithm tends to underestimate $H_{s\text{swell}}$ values by as much as 50%. Nonetheless, overall mean values agree relatively well: $H_{s\text{swell}} = 1.2$ m from SARTool and $H_{s\text{swell}} = 0.9$ m from our implementation. Correlation coefficient $r = 0.83$, normalized root mean square error ($NRMSE$) = 0.45 and normalized bias (NB) = 0.24. The same analysis has been made for SAR-derived peak wavelengths $L_{p\text{SAR}}$. It is interesting to note in figure 4b that $L_{p\text{SAR}}$ data is divided into two well-defined groups, corresponding to the two observed swell systems propagating into Tehuantepec. Deviations from the $r = 1$ line (dashed) are mainly due to the fact that no partition has been included in the analysis and thus, systems are mixed in the analysis. Nonetheless, statistics are in better agreement than : $r = 0.88$, $NRMSE = 0.36$ and $NB = -0.37$.

5. Estimation of wave spectra and derivation of integral parameters from TerraSAR-X images of the ocean surface.

Once evaluated on ENVISAT imagery, performance of the algorithm has been tested on two TerraSAR-X scenes acquired over the Gulf of Tehuantepec during a strong *Tehuano* event on 20 and 21 march 2008. Acquisition was part of a field campaign during which the sea-state was recorded in situ at two of the three near-shore stations where ADCP (Nortek Aquadopp) were deployed as part of the INTOA experiment in

2005. Figure 6 shows the location of the two stations where waves were recorded in situ at the Gulf of Tehuantepec. The map shows as well the area covered by the two TerraSAR-X scenes coinciding with the field campaign.

In a similar fashion as above, figure 7 shows a comparison between wave spectra estimated from in situ measurements and wave spectra derived from the inversion algorithm implemented for the TerraSAR-X imagery.

Once the wave-inversion has been reasonably validated, an additional set of TerraSAR-X images has been used to estimate the near-shore wave-field at the Gulf of Tehuantepec. As shown in Table 1, additional scenes include a StripMap scene acquired on 6 November 2008 at 12:20h and two ScanSAR mode scenes, acquired on 7 and 12 November at 00:19h and 12:11h UTC, respectively.

6. Summary and concluding remarks

In this work, a wave-inversion algorithm for TerraSAR-X images of the ocean surface has been made. This first approach has been adapted from the algorithm developed by *Lai & Delisi* [2010] for the C-band SAR. The main difference between the two is that in our work, wind information required to estimate the contribution of the hydrodynamic MTF is not obtained directly from the SAR image but supplied from an external database. This is due to the fact that a GMF to reliably derive wind speed from X-band imagery, analogous to the scatterometer CMOD4 GMF, is not currently

available. Therefore, a few wind databases were compared to in situ data gathered during a field campaign at the south Pacific coast of Mexico in 2005. Given its performance and availability, the blended QuikSCAT wind product developed at IFREMER [CERSAT 2002] was selected as the best source.

7. Acknowledgements

Funding for this study has been supplied from the Mexican Council for Science and Technology (CONACyT) through the project PE-oleajePBC (S0019-2009-01/119798). ENVISAT-ASAR images have been supplied by the European Space Agency while TerraSAR-X products, by the German Aerospace Center (DLR) through project OCE0506. Our gratitude goes to Dr. D. Lai from NorthWest Research Laboratory for its comments regarding their wave inversion algorithm. Special thanks to Dr. S. Lehner from DLR for providing a compilation of Matlab © routines for additional SAR image processing.

8. References

- Alpers, W. and K. Hasselmann, "The two-frequency microwave technique for measuring ocean-wave spectra from an airplane or satellite", *Boundary-Layer Meteorology*, vol. 13, pp. 215–230, 1978.
- Alpers, W. R., D. B. Ross and C. R. Rufenach, "On the detectability of ocean surface waves by real and synthetic aperture radar", *Journal of Geophysical Research*, vol. 86, no. C7, pp. 6481-6498, July, 1981.

Atlas, R., R. N. Hoffman, J. Ardizzone, M. Liedner and J. C. Jusem, "Development of a new cross-calibrated, multi-platform (CCMP) ocean surface wind product", paper presented at the *13th Conference on Integrated Observing and Assimilation Systems for Atmosphere, Oceans, and Land Surface (IOAS-AOLS)*, Phoenix, AZ, January, 2009.

Brusch, S., S. Lehner, T. Fritz, M. Soccorsi, A. Soloviev & B. van Schie, "Ship surveillance with TerraSAR-X", *IEEE Transactions on Geoscience and Remote Sensing*, vol. 49, no. 3, pp. 1092–1103, October, 2010.

CERSAT, "QuikSCAT Scatterometer Mean Wind Field Products - User Manual", Version 1.0., Document C2-MUT-W-03-IF, IFREMER, February 2002.

Collard, F., F. Arduin, and B. Chapron, "Extraction of coastal ocean wave fields from SAR images", *IEEE Journal of Oceanic Engineering*, vol. 30, no. 3, pp. 526–533, July, 2005. doi: 10.1109/JOE.2005.857503 .

Díaz Méndez, G. M., F. J. Ocampo-Torres and B. Chapron, "Synthetic aperture radar analysis of ocean-swell variability at the Gulf of Tehuantepec under moderate-offshore winds", submitted to *Journal of Geophysical Research - Oceans*, on May, 2011.

Díaz Méndez, G. M., S. Lehner, F. J. Ocampo-Torres, X. Li and S. Brusch, "Wind and wave observations off the south Pacific coast of Mexico using TerraSAR-X imagery", *International Journal of Remote Sensing*, vol. 31, no. 17, pp. 4933–4955, September, 2010.

Engen, G. and H. Johnsen, "SAR-ocean wave inversion using image cross spectra",

IEEE Transactions on Geoscience and Remote Sensing, vol. 33, no. 4, pp. 1047–1056, July, 1995.

García-Nava, H., F. J. Ocampo-Torres, P. Osuna, and M. A. Donelan, "Wind stress in the presence of swell under moderate to strong wind conditions", *Journal of Geophysical Research*, vol. 114, no. C12008, December, 2009. DOI: 10.1029/2009JC005389.

Hasselmann, K. and S. Hasselmann, "On the nonlinear mapping of an ocean wave spectrum into a synthetic aperture radar image spectrum and its inversion", *Journal of Geophysical Research*, vol. 96, no. C6, pp. 10713–10729, 1991.

Johnsen, H., G. Engen & B. Chapron, "Validation of ASAR WaveMode Level 2 product using WAM and buoy spectra", paper presented at the Coastal and marine applications of SAR, *ESA Special Publications SP-565*, Svalbard, Norway, September, 2003.

Kahma, K. K. and C. J. Calkoen, C., "Reconciling discrepancies in the observed growth of wind-generated waves", *Journal of Physical Oceanography*, vol. 22, pp. 1389–1405, December, 1992.

Lai, D. and D. Delisi, "Spatial distribution of surface wave field in coastal regions using space-borne synthetic aperture radar", *International Journal of Remote Sensing*, vol. 31, no. 17, pp. 4915–4931, September, 2010.

Li, X. M., S. Lehner & W. Rosenthal, "Investigation of ocean surface wave refraction using TerraSAR-X data", *IEEE Transactions on Geoscience and Remote Sensing*, vol. 48, no. 2, pp. 830–840, November, 2009.

- Ocampo-Torres, F. J., H. García-Nava, R. Durazo, P. Osuna, G. M. Díaz Méndez, and H. C. Graber, "The intOA Experiment: a study of ocean-atmosphere interactions under moderate to strong offshore winds and opposing swell conditions in the Gulf of Tehuantepec, Mexico", *Boundary-Layer Meteorology*, vol. 138, pp. 433–451, 2011. DOI: 10.1007/s10546-010-9561-5.
- Ocampo-Torres, F. J. and I. S. Robinson, "Wind-directional effects on the hydrodynamic modulation of microwave radar images of ocean waves", *International Journal of Remote Sensing*, vol. 10, no. 8, pp. 1339–1355, August, 1989.
- Plant, W. J. and L. M. Zurk, "Dominant wave directions and significant wave heights from synthetic aperture radar imagery of the ocean", *Journal of Geophysical Research*, vol. 102, no. C2, pp. 3473–3482, February, 1997.
- Stoffelen, A. and D. Anderson, "Ambiguity removal and assimilation of scatterometer data", *Quarterly Journal of the Royal Meteorological Society*, vol. 123, no. 538, pp. 491–518, January, 1997.

Tables

Table 1. Characteristics of the various SAR images analyzed in this study.

Platform (band) & imaging mode	date & time (UTC)	path	track azimuth	polarization	coverage [km]
Envisat (C) Image mode, SLC	26 Feb 2005 @ 04:20h	A	347.5°	VV	100 by 100
Envisat (C) Image mode, SLC	02 Mar 2005 @ 16:20h	D	192.5°	VV	100 by 100
Envisat (C) Image mode, SLC	18 Mar 2005 @ 16:17h	D	192.5°	VV	100 by 100
TerraSAR-X (X) StripMap	20 Mar 2008 @ 12:19h	D	348.6°	HH	30 by 50
TerraSAR-X (X) ScanSAR	21 Mar 2008 @ 00:19h	A	191.4°	HH	100 by 150
TerraSAR-X (X) StripMap	06 Nov 2008 @ 12:20h	D	348.6°	VV	30 by 50
TerraSAR-X (X) ScanSAR	07 Nov 2008 @ 00:19h	A	191.4°	VV	30 by 50
TerraSAR-X (X) ScanSAR	12 Nov 2008 @ 12:11h	D	348.6°	HH	100 by 150

SLC - single-look complex; A - ascending; D - descending

Figures

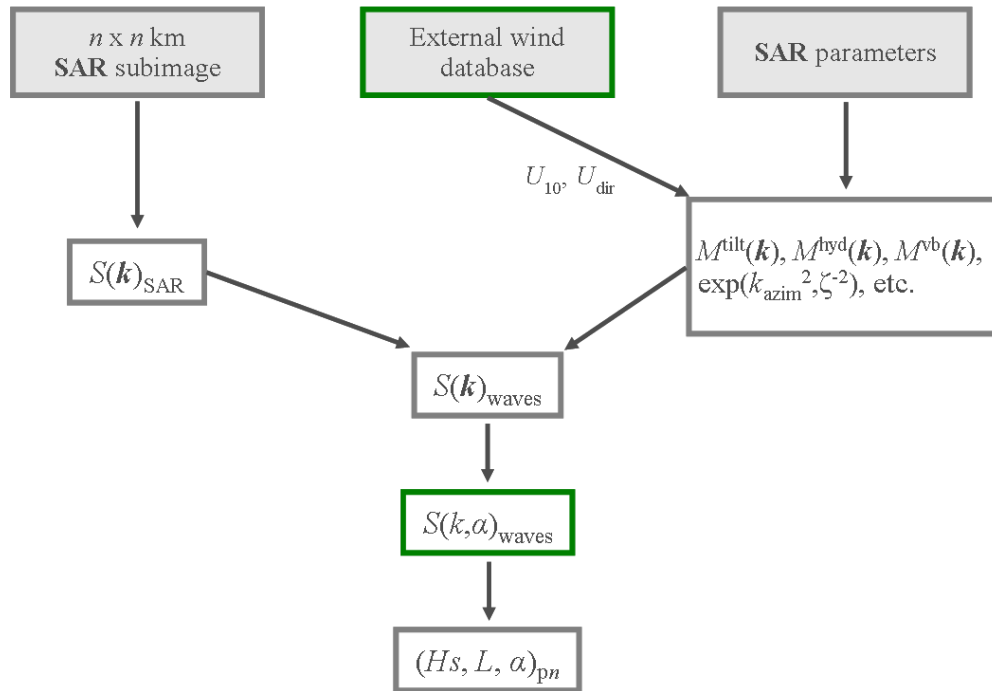


Figure 1. Flow diagram of the wave-inversion algorithm for TerraSAR-X imagery proposed in this study.

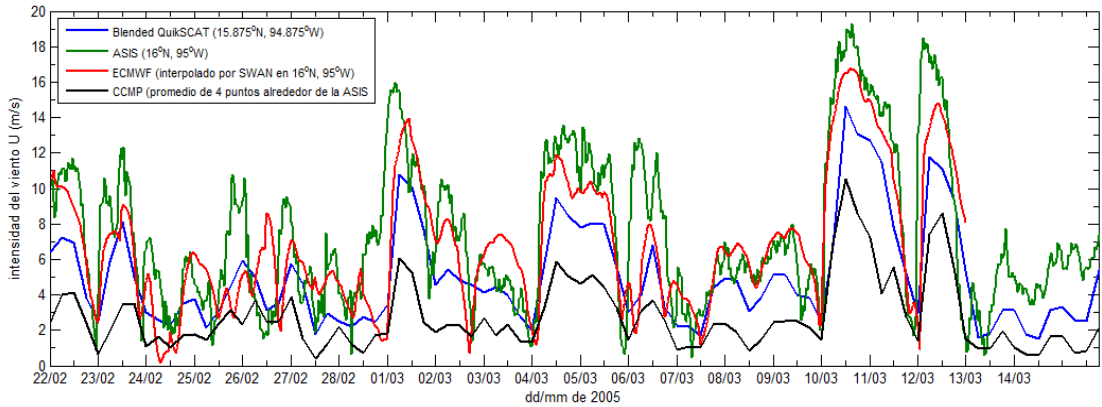


Figure 2. Comparison of model-derived wind speed U_{10} to time series of in situ data (green line) measured during the 2005 field campaign at the Gulf of Tehuantepec. Data sets are: ECMWF special run (red line), blended QuikSCAT (blue) and CCMP (black). Note that while ECMWF matches best the measured data, particularly during the strong peaks in March, CCMP significantly underestimates these maxima.

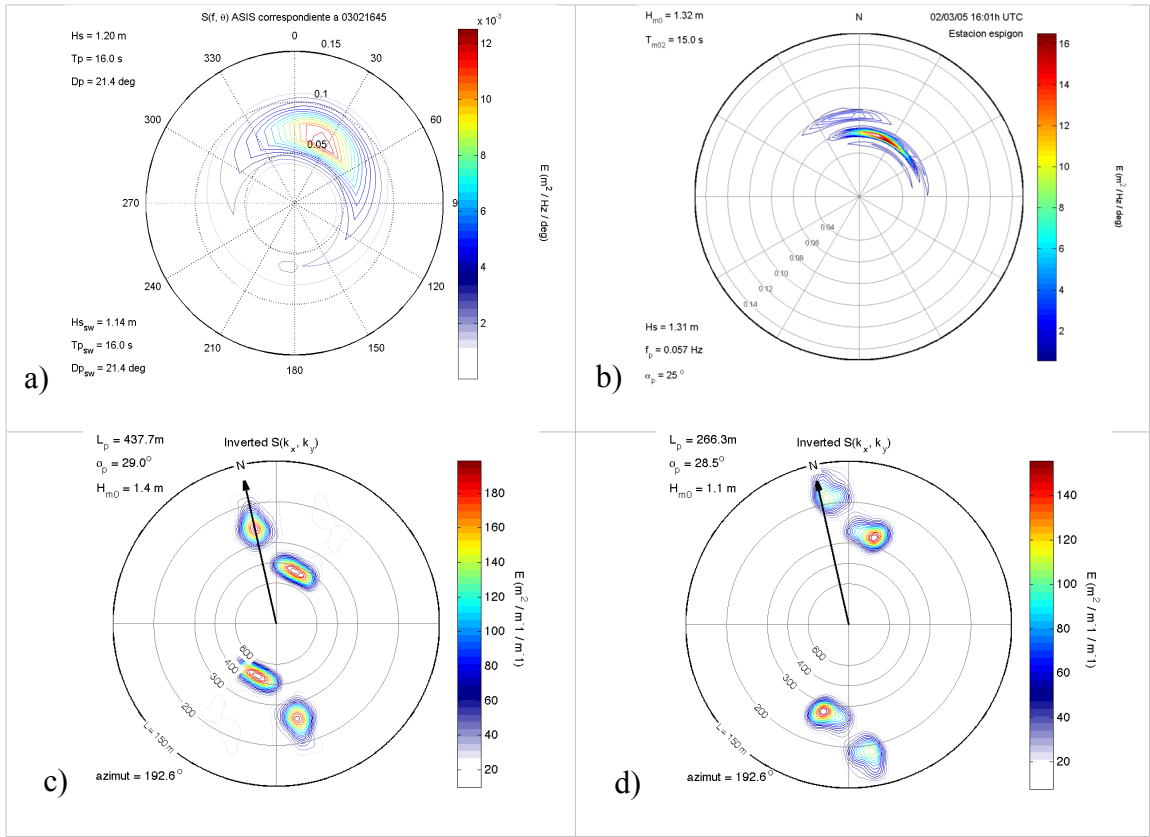


Figure 3. Comparison of 2D wave spectra estimated through in situ measurements to nearly collocated SAR-inverted wave spectra estimated from a C-band ENVISAT-ASAR scene acquired on 2 March 2005 at 16:20h UTC: a) $S(f,\alpha)$ derived from the ASIS buoy, moored at 60-m water depth; b) $S(f,\alpha)$ derived from an ADCP (Aquadopp, Nortek) deployed 5 km offshore, at 20-m of depth; c) and d) $S(k_x, k_y)$ derived from our inversion algorithm, approximately collocated to a) and b), respectively.

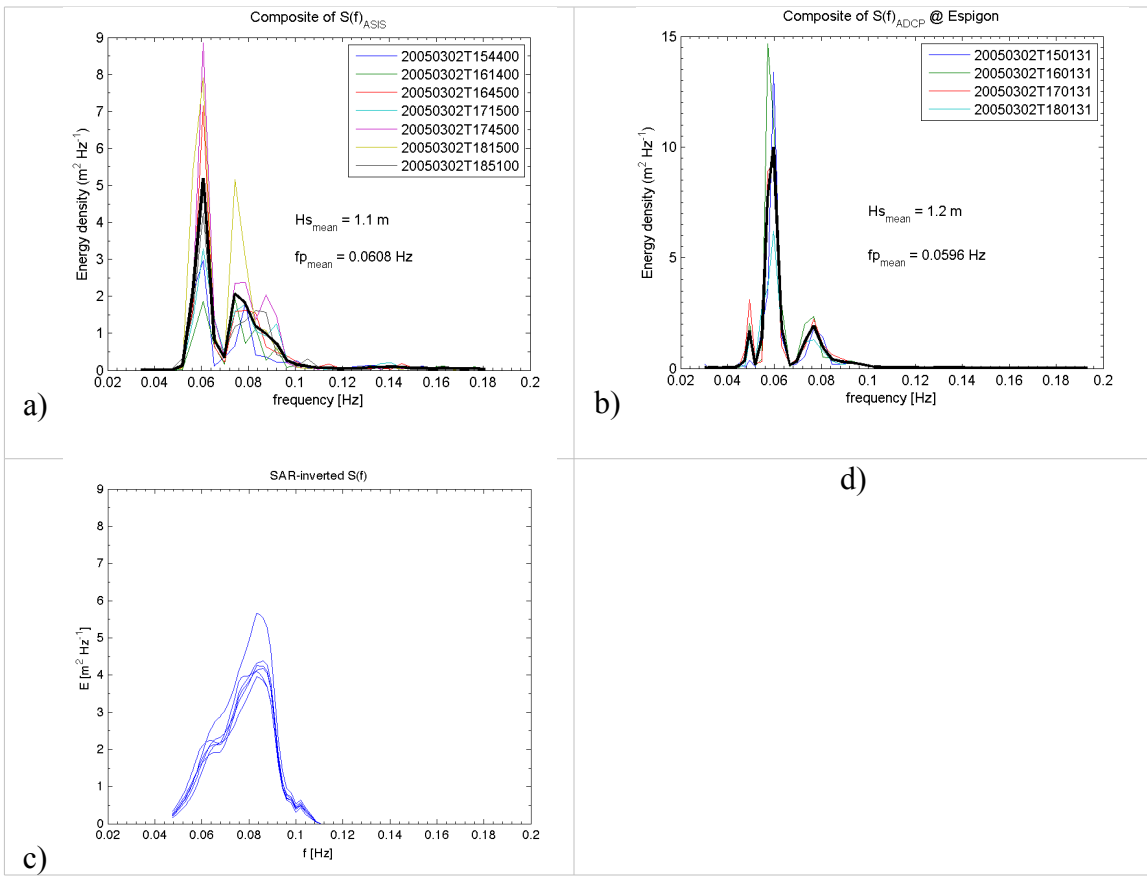


Figure 4. Comparison of wave frequency-spectra $S(f)$ estimated from in situ records

from the inTOA campaign with nearly-collocated $S(f)_{\text{SAR}}$ derived from our inversion algorithm.

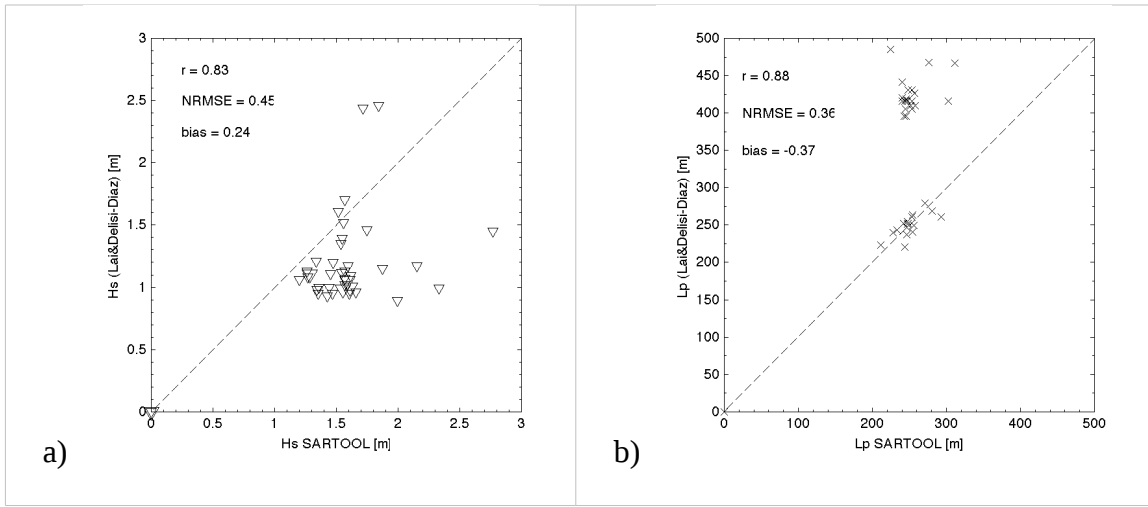


Figure 5. Comparison of integral wave parameters derived following *Collard et al.* [2005] and derived from our implementation. This example corresponds to ENVISAT ASAR SLC scene acquired on 2 March 2005 at 16:20h UTC. a) H_s _{SAR}. b) L_p _{SAR}.

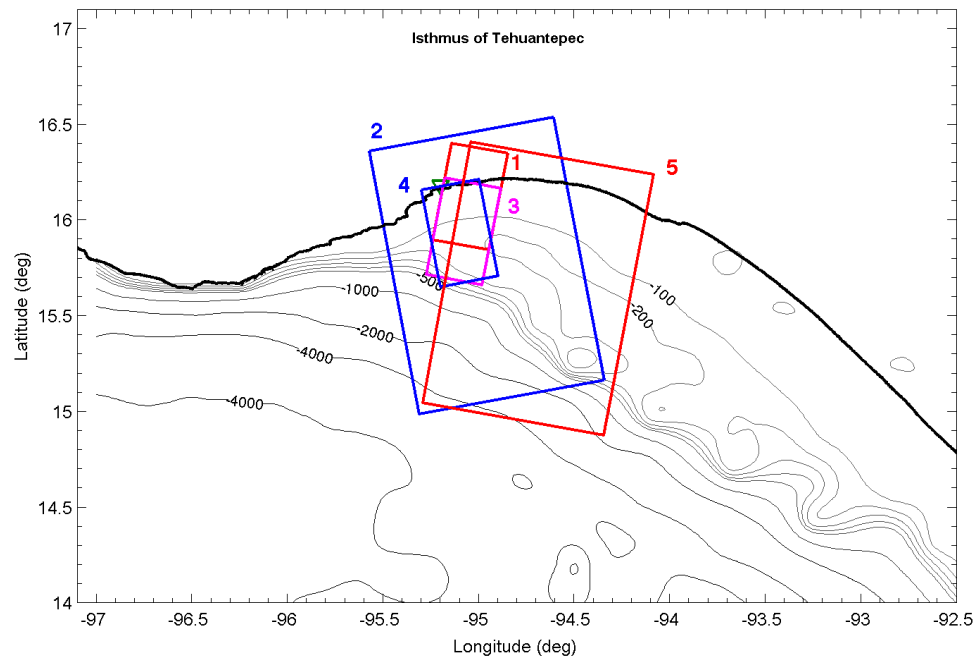


Figure 6. Map with the location of the five TerraSAR-X images used in this study.

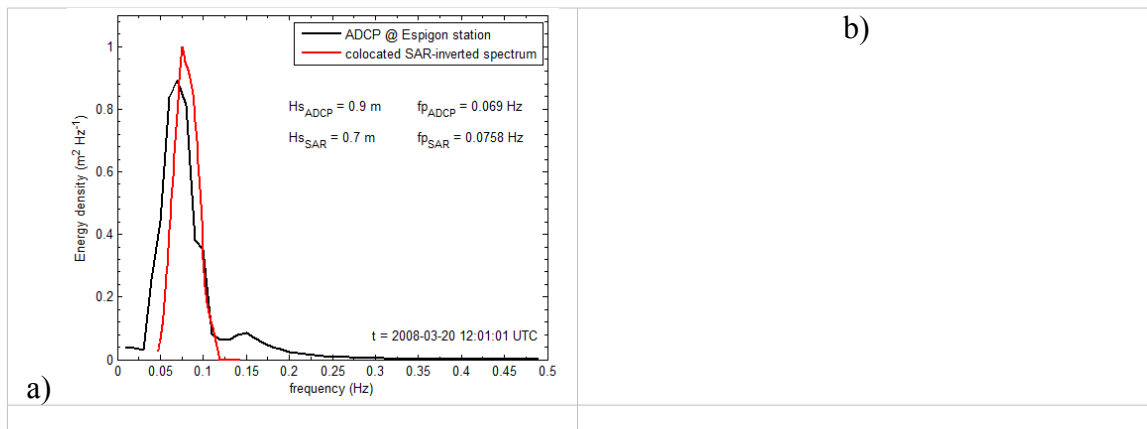


Figure 7. Comparison of wave spectra derived from in situ measurements recorded during the 2008 field campaign in Tehuantepec and from inverted TerraSAR-X images.

V. CONCLUSIONES GENERALES

El presente trabajo de tesis doctoral ha tenido por objeto contribuir al estado del conocimiento sobre la evolución del oleaje en el Golfo de Tehuantepec y océano Pacífico adyacente, bajo las condiciones de viento intenso características de este área de estudio. Para ello se han utilizado, como fuente principal de información, imágenes de la superficie del océano adquiridas desde satélites mediante SAR. Las características de los campos de oleaje y viento estimados mediante SAR han sido comparadas con parámetros correspondientes, calculados a partir de mediciones de campo y resultados de simulación numérica.

Con base en los análisis realizados se puede concluir que, de manera general, el campo de oleaje en el Golfo de Tehuantepec se caracteriza por presentar estados de mar dominados por múltiples sistemas de oleaje libre coexistiendo simultáneamente, con valores típicos (asociados a los picos del espectro) de longitud de onda $L_p = 200\text{--}400$ m, altura significante $H_s = 0.5\text{--}4$ m y dirección de propagación en el sector azimutal $\alpha_p = 335^\circ\text{--}135^\circ$. Estos sistemas se propagan a lo largo de hasta 14,000 km, principalmente desde el Pacífico sudoccidental frente a la costa Antártica, así como también desde el Pacífico norte; aunque estos últimos, raramente al norte de los 15.25° de latitud. Además del oleaje generado por tormentas lejanas, en la zona de estudio se

observa la presencia de oleaje local, generado por los *Tehuanos*. Dado que la frecuencia e intensidad de los vientos de chorro son mayores durante los meses de invierno y primavera [Trasviña y Barton 2008], en estas épocas el oleaje forzado puede alcanzar valores de $H_{s\text{sea}} \sim 3$ m y $L_{p\text{sea}} \sim 120$ m en las inmediaciones del Golfo.

En particular, el estudio de la variabilidad del oleaje libre realizado a partir del análisis de imágenes SAR adquiridas por el satélite europeo ENVISAT como parte del proyecto INTOA, reveló que el campo de olas observado de forma casi instantánea sobre un área de aproximadamente 100 km por 400 km, estaba compuesto por hasta cuatro sistemas de oleaje libre coexistiendo simultáneamente. Se encontró que parámetros típicos como la longitud de onda estimada a partir del SAR, $L_{p\text{SAR}} = 190\text{--}311$ m concordaban relativamente bien con valores correspondientes medidos en campo: $L_{p\text{swell}} = 185\text{--}322$ m. Otros, como la altura significante, tendían a la sobreestimación $H_{s\text{SAR}} = 0.3\text{--}1.9$ m contra $H_{s\text{swell}} = 0.4\text{--}1.2$ m. Se observó que, aún bajo las condiciones de viento moderado imperantes en los momentos de adquisición de los tres juegos de imágenes, la variabilidad espacial de los sistemas, una vez aislados tenía valores entre 7 y 17%. Análisis de la variabilidad espacial de L_p a lo largo de la trayectoria de propagación a_p correspondiente, en algunos casos, nos permitió determinar el momento t_0 y la distancia al punto generación Δ del oleaje libre.

Por otro lado, los días 20 y 21 de marzo de 2008, el TerraSAR-X adquirió dos imágenes sobre el Golfo de Tehuantepec coincidiendo con un evento

Tehuano que, de acuerdo a la base de datos blended QuikSCAT [CERSAT 2002], inició el 19 de marzo y finalizó aproximadamente 60 horas después, la noche del día 21, alcanzando valores máximos de velocidad de viento (promediados cada 6 horas) $U_{10} = 23 \text{ ms}^{-1}$ aproximadamente a las 18h UTC del 20 de marzo. Análisis de las imágenes tipo *StripMap* de las 12:19h UTC y tipo *ScanSAR* de las 00:19h revelaron que el chorro de viento tiene forma de abanico, como había sido sugerido por *Chelton et al.* [2000]; se observó también que el eje del chorro de viento presentó una rotación de aproximadamente 25° en sentido horario (de $\sim 165^\circ$ a $\sim 190^\circ$ azimutales), como función del tiempo. Sin embargo, los valores de velocidad del viento calculados a partir de la función X-MOD subestimaron hasta en un 30% los valores máximos calculados por el modelo. Análisis espectrales mostraron que los procesos que genera el viento sobre la superficie del océano (*wind streaks*, *boundary rolls*, etc.), útiles para determinar su dirección, bajo las condiciones de viento intenso observadas, presentaron ondulaciones con longitud L menor que lo normal ($\sim 600\text{--}1200$ m, [Katsaros et al. 2002]). Estos valores son equivalentes a los del oleaje libre estimados mediante SAR, y por tanto, oscurecen su detección. Por su parte, los resultados del análisis de los espectros de intensidad de la imagen SAR en el intervalo limitado por los de números de onda $k_{\min} = 0.0105 \text{ radm}^{-1}$ y $k_{\max} = 0.0898 \text{ radm}^{-1}$ (correspondientes a longitudes de onda $L_{\max} = 600$ m y $L_{\min} = 70$ m, respectivamente) revelaron la presencia de varios grupos de ondulaciones en la superficie del mar con

longitudes de onda asociadas a los picos observados $L_p = 90\text{--}350$ m aproximadamente y direcciones de propagación correspondientes en el rango $\alpha_p = 0\text{--}45^\circ$, respecto del norte geográfico. Estos resultados son comparables con parámetros de oleaje calculados mediante simulación numérica por el modelo WAM (resultados cortesía del Servicio Meteorológico Alemán). Análisis de la evolución espacial de estos espectros revelaron la disminución de los valores de L_p con la distancia a la costa, así como variaciones de los valores de α_p . Estos resultados son nuevamente consecuentes con los resultados de la simulación numérica así como con los modelos analíticos de asombramiento y refracción.

Análisis adicionales realizados a subimágenes obtenidas de la imagen tipo ScanSAR entre 60–120 km de la costa, revelaron la presencia de una señal que creemos corresponde al oleaje generado localmente en condiciones de *fetch* limitado por los vientos de chorro. Análisis de linealidad realizados de acuerdo con *Alpers et al.* [1981] sugieren que esta señal se encuentra en el límite de detección del SAR. Por tanto, se compararon los valores de $L_{p,SAR}$ calculados de las subimágenes contra valores correspondientes estimados a partir de las relaciones paramétricas de *Kahma y Calkoen* [1992] sobre crecimiento del oleaje, y se observó que las primeras superaban a las segundas hasta en un 49%.

A partir de los análisis realizados en este trabajo se puede concluir que el

SAR es una herramienta adecuada para estimar la variabilidad espacial de los campos de viento y oleaje, además de otros procesos que imprimen su huella sobre la superficie del mar, aunque con ciertas limitaciones. Tiene la ventaja de que proporciona información detallada sobre las características espaciales del oleaje en áreas del océano de decenas a centenas de kilómetros en forma casi instantánea. Sin embargo, su capacidad de detección está circunscrita al rango de longitudes de onda correspondientes al oleaje libre y limitada por factores como el viento y el estado de mar. Además, dado que el ciclo orbital de los satélites (intervalo de tiempo en el que se repite la misma órbita exactamente) es de varios días, la resolución temporal adecuada para estudiar la naturaleza del oleaje en el área de estudio es también limitada. Así, aunque algunos trabajos han demostrado que el viento es capaz de provocar la atenuación del oleaje propagándose en sentido contrario [Young y Sobey 1985; Peirson *et al.* 2003], o bien que las corrientes pueden provocar una fuerte refracción de las olas [Beal *et al.* 1983, 1986; Irvine y Tilley 1988], los resultados de mis análisis con SAR no son concluyentes en este sentido. Considero que sería muy interesante realizar experimentos adicionales, en el que pudiera disponerse de un acervo más completo de imágenes SAR, quizás adquiridas durante distintas fases de evolución de un *Tehuano* y quizás en combinación con otros sensores.

VI. LITERATURA CITADA

- ARDHuin, F. y A. Jenkins, 2006. On the interaction of surface waves and upper ocean turbulence. *Journal of Physical Oceanography*, 36(3): 551–557.
- ARDHuin, F., W. O'Reilly, T. Herbers y P. Jessen, 2003. Swell transformation across the continental shelf - Part I: attenuation and directional broadening. *Journal of Physical Oceanography*, 33: 1921–1939.
- ALPERS, W.R., D.B. Ross y C.L. Rufenach, 1981. On the detectability of ocean surface waves by real and synthetic aperture radar. *Journal of Geophysical Research*, 86(C7): 6481–6498.
- BEAL, R, 1980. Spaceborne imaging radar ocean wave monitoring. *Science*, 208(4450): 1373–1375.
- BEAL, R, 1981. Spatial evolution of ocean wave spectra, in Spaceborne SAR for Oceanography. Editado por R. Beal, P. DeLeonibus y I. Katz. *John Hopkins University press*: 110–127.
- BEAL, R., T. Gerling, D. Irvine, F. Monaldo y D. Tilley, 1986. Spatial variations of ocean wave directional spectra from the SEASAT SAR. *Journal of Geophysical Research*, 91(C2): 2433–2449.
- BEAL, R., D. Tilley y F. Monaldo, 1983. Large- and small-scale spatial evolution of digitally processed ocean wave spectra from SEASAT SAR. *Journal of Geophysical Research*, 88(C3): 1761–1778.

- BLACKBURN, M., 1962. An oceanography study of the Gulf of Tehuantepec, United States Fisheries and Wildlife Service. *Special Scientific Report - Fisheries*, 404, 28 pp.
- BRANDHORST, W., 1958. Thermocline topography, zooplankton standing crop, and mechanisms of fertilization in the eastern tropical Pacific. *Conseil Permanent International Exploration de la Mer, Journal du Conseil*, 24(1): 16–31.
- CAVALERI, L., J. Alves, F. Arduin, A. Babanin, M. Banner, K. Belibassakis, M. Benoit, M. Donelan, J. Groeneweg, T. Herbers, P. Hwang, P. Janssen, T. Janssen, I. Lavrenov, R. Magne, J. Monbaliu, M. Onorato, V. Polnikov, D. Resio, W. Rogers, A. Sheremet, J. McKee Smith, H. Tolman, G. van Vledder, J. Wolf y I. Young, 2007. Wave modelling - state of the art. *The WISE Group*. 104 pp.
- CHELTON, D., M. Freilich y S. Esbensen, 2000. Satellite observations of the wind jets off the Pacific coast of Central America - part I: case studies and statistical characteristics. *Monthly Weather Review*, 128: 1993–2018.
- ENGEN, G. y H. Johnsen, 1995. SAR-ocean wave inversion using image cross spectra. *IEEE Transactions on Geoscience and Remote Sensing*, 33(4): 1047–1056
- GARCÍA NAVA, H., F. J. Ocampo-Torres, P. Osuna y M. Donelan, 2009. Wind stress in the presence of swell under moderate to strong wind conditions, *Journal of Geophysical Research*, 114(C12008), doi:

- 10.1029/2009JC005389.
- GONZALEZ F., T. Thompson, W. Brown Jr. y D. Weissman, 1982. SEASAT wind and wave observations of NE Pacific hurricane Iva, Aug. 13 1978. *Journal of Geophysical Research*, 87(): 3431–3438.
- HASSELMANN, K., T.P. Barnett, E. Bouws, H. Carlson, D.E. Cartwright, K. Enke, J.A. Ewing, H. Gienapp, D.E. Hasselmann, P. Sell y H. Walden, 1973. Measurements of wave-wind growth and swell decay during the Joint North Sea Wave Project (JONSWAP). *Dtsch. Hydrogr. Z. Reihe A*. 8, 12.
- IRVINE, D. y D. Tilley, 1988. Ocean wave directional spectra and wave-current interaction in the Agulhas from the shuttle imaging radar-B synthetic aperture radar. *Journal of Geophysical Research*, 93(C12): 15,389–15,401.
- JANSSEN, P. y W. Alpers, 2006. Why SAR wave mode data of ERS and Envisat are inadequate for giving the probability of occurrence of freak waves. *Trabajo presentado en el Taller SEASAR 2006*. ESA/ESRIN, Enero 23 a 26 de 2006.
- KATSAROS, K., P. Vachon, T. Liu y P. Black, 2002. Microwave remote Sensing of tropical cyclones from space. *Journal of Oceanography*, 58: 137–151.
- KATSAROS, K., Y. Quilfen, B. Chapron y Z. Hongwei, 1994. Tropical cyclone surface winds and waves from the Active Microwave Instrument of the ERS-1: comparison to Special Sensor Microwave Imager. *International Geoscience and Remote Sensing Symposium*, 1994.

- KEMP, P. y R. Simons, 1983. The interaction of waves and a turbulent current: waves propagating against the current. *Journal of Fluid Mechanics*, 130: 73–89.
- LEHNER, S., A. Reppucci y J. Schulz-Stellenfleth, 2007. Validation of parametric hurricane models by ENVISAT - ASAR images. *Trabajo presentado en el Simposio ENVISAT 2007. ESA*.
- MASTENBROEK, C, 1998. Spectral wave climate data from space-borne SAR. *Marine meteorology and related oceanographic activities: provision and engineering/operational application of ocean wave data Unesco*, Paris, 21-25 September 1998. pp. 304-309.
- MASTENBROEK, C. y C. de Valk, 2000. A semiparametric algorithm to retrieve ocean wave spectra from synthetic aperture radar. *Journal of Geophysical Research*, 105(C2): 3497–3516.
- OCAMPO-TORRES, F., 2001. On the homogeneity of the wave field in coastal regions as determined from ERS-2 and RADARSAT SAR images of the ocean surface. *Scientia Marina*. 65(Supl. 1): 215–228.
- OCAMPO-TORRES, F. y P. Vachon, 2000. Spatial variations of ocean wave spectra in coastal regions from RADARSAT and ERS synthetic aperture radar images. *Trabajo presentado en la 6ta Conf. Int. sobre Sensores Remotos para Ambientes Marinos y Costeros*. Charleston, SC. EEUU.
- OCAMPO-TORRES, F. J., H. García-Nava, R. Durazo, P. Osuna, G. M. Díaz Méndez. and H. C. Graber, 2011. The intOA Experiment: a study of ocean-

- atmosphere interactions under moderate to strong offshore winds and opposing swell conditions in the Gulf of Tehuantepec, Mexico, *Boundary-Layer Meteorology*, 138: 433–451. DOI 10.1007/s10546-010-9561-5.
- PEIRSON, W., A. Garcia y S. Pells. 2003. Water wave attenuation due to opposing wind. *Journal of Fluid Mechanics*, 487: 345–365.
- REPPUCCI, A., J. Schulz-Stellenfleth, S. Lehner y T. König. 2007. Analysis of SAR wave mode imagette taken under extreme wind and wave conditions. Trabajo presentado en el *Simposio ENVISAT 2007*. ESA.
- RODEN, G. I., 1961. On the wind driven circulation in the Gulf of Tehuantepec and its effect upon surface temperature. *Geofísica Internacional*, 1(3): 55–72.
- ROMERO, L. y K. Melville, 2010a. Airborne Observations of Fetch-Limited Waves in the Gulf of Tehuantepec. *Journal of Physical Oceanography*, 40: 441–465.
DOI: 10.1175/2009JPO4127.1.
- ROMERO, L. y K. Melville, 2010b. Numerical Modeling of Fetch-Limited Waves in the Gulf of Tehuantepec. *Journal of Physical Oceanography*, 40: 466–486.
DOI: 10.1175/2009JPO4128.1.
- SCHULZ-STELLENFLETH, J. 2007. Retrieval of integral ocean wave parameters from SAR Data using an empirical approach. Trabajo presentado en el *Simposio ENVISAT 2007*. ESA.

- SNODGRASS, F., G. Groves, K. Hasselmann, G . Miller, W. Munk y W. Powers, 1966. Propagation of ocean swell across the Pacific. *Philosophical Transactions of the Royal Society of London*, 259(1103): 431–497.
- TRASVIÑA, A. y E. D. Barton, 2008. Summer circulation in the Mexican tropical Pacific. *Deep-sea Research I*, 55: 587–607.
- VIOLANTE-CARVALHO, N., F. Ocampo-Torres e I. Robinson, 2004. Buoy observations of the influence of swell on wind waves in the open ocean. *Applied Ocean Research*, 26(1-2): 49–60.
- WAMDIG: The WAM - Development and Implementation Group: S. Hasselmann, K. Hasselmann, E. Bauer, L. Bertotti, V. Cardone, J. A. Ewing, J. A. Greenwood, A. Guillaume, P. Janssen, G. J. Komen, P. Lionello, M. Reistad, y L. Zambresky, 1988. The WAM Model: a third generation ocean wave prediction model. *Journal of Physical Oceanography*, 18(12): 1775–1810.
- YOUNG, I. y R. Sobey, 1988. Deep water swell and spectral wave decay in opposing winds. *Journal of Waterway, Port, Coastal and Ocean Engineering*, 114(6): 732–744.